

INFORMATION TO USERS

This manuscript has been reproduced from the microfilm master. UMI films the text directly from the original or copy submitted. Thus, some thesis and dissertation copies are in typewriter face, while others may be from any type of computer printer.

The quality of this reproduction is dependent upon the quality of the copy submitted. Broken or indistinct print, colored or poor quality illustrations and photographs, print bleedthrough, substandard margins, and improper alignment can adversely affect reproduction.

In the unlikely event that the author did not send UMI a complete manuscript and there are missing pages, these will be noted. Also, if unauthorized copyright material had to be removed, a note will indicate the deletion.

Oversize materials (e.g., maps, drawings, charts) are reproduced by sectioning the original, beginning at the upper left-hand corner and continuing from left to right in equal sections with small overlaps. Each original is also photographed in one exposure and is included in reduced form at the back of the book.

Photographs included in the original manuscript have been reproduced xerographically in this copy. Higher quality 6" x 9" black and white photographic prints are available for any photographs or illustrations appearing in this copy for an additional charge. Contact UMI directly to order.

U·M·I

University Microfilms International
A Bell & Howell Information Company
300 North Zeeb Road, Ann Arbor, MI 48106-1346 USA
313 761-4700 800 521-0600

Order Number 9230506

Ab initio calculations performed on CO adsorption on the
Fe(100) surface and complementing theoretical techniques

Meehan, Timothy Erickson, Ph.D.

University of Hawaii, 1992

U·M·I

300 N. Zeeb Rd.
Ann Arbor, MI 48106



Ab Initio Calculations Performed on CO Adsorption on
the Fe(100) Surface and Complementing Theoretical
Techniques

A Dissertation Submitted to the Graduate Division of
the University of Hawai'i in Partial Fulfillment of
the Requirements for the Degree of
Doctor of Philosophy

in
Chemistry
May 1992

By
Timothy Erickson Meehan

Dissertation Committee
John Head, Chairperson
Thomas Bopp
Edgar Kiefer
Karl Seff
Anthony Clarke

Acknowledgements

I would like to acknowledge **John Head** for his brilliant teachings and endless patience. I will be indebted to him forever. I would also like to acknowledge Drs. Kiefer, Seff, and Clarke for the encouragement they gave me through the years and for the excellent discussions we have had concerning research, science, and humanity. This would also have to include my professors during undergraduate school at Willamette University and the University of Munich, who were foolish enough to believe in me.

I thank Mike Burger, Don Cole, and Cyril Choy for the technical support; otherwise, I would still be hacking away at the computer screen. I am grateful to Walter Niemczura for the use of his high speed disk and for not becoming too unglued when the system became full.

Lastly I would like to thank the most important people in my life for making my undergraduate and post-graduate studies worth it: karen, michael, terry, shannon, the l'meister, jim, jim's family, brutus, jon, jon, mark and beth, jenny, ray, ray's dogs, jenny's mom, chris, rory, tricia, liz, liz's family, kurt and mary jane, jon and trace, jim, jim's family, jim, johnny, johnny's lovely sisters, johnny's parents, sponge, lars, ream, jon, bruce, eric, susie, weissbier, deitmar, christina, jon and kathryn, chris

and jill, mike and laurie, susie, hoser, joyce, gloria,
yuichi, lester, brian, mario, naresh, ian and jacqui, ted,
allan, todd, louie and the rest of the ghetto floor, jay and
gail, deanly, mark and paige, john and vicki, kim, chris,
scott, cheryl, paul, karl and jane, jack, and the people of
the Martial Islands.

Abstract

Unrestricted Hartree-Fock calculations were performed on Fe_xCO clusters to model the $\text{CO}(\alpha_1)$, $\text{CO}(\alpha_2)$, and $\text{CO}(\alpha_3)$ adsorptions on the $\text{Fe}(100)$ surface. Clusters of $\text{FeCO}(\text{C}_{4v})$ and a multiplicity of 5, $\text{Fe}_2\text{CO}(\text{C}_{2v})$ and a multiplicity of 7, and $\text{Fe}_2\text{CO}(\text{C}_s)$ and a multiplicity of 7, were constructed to model, respectively, the adsorption for the on top site, bridging site, and tilted CO structure at the 4-fold site. The CO position was optimized with respect to the Fe bulk distances using gradient techniques and the partial geometry optimization. CO stretching frequencies were calculated for each optimized geometry, and we find no evidence supporting CO adsorption in the bridging site. Using a full basis set the calculated CO stretching frequencies for the $\text{FeCO}(\text{C}_{4v})$, $\text{Fe}_2\text{CO}(\text{C}_{2v})$, and the $\text{Fe}_2\text{CO}(\text{C}_s)$ clusters are 1992, 1767, and 771 cm^{-1} , respectively. The CSOV analysis was executed to analyze the major orbital interactions between the CO and Fe_x clusters. For both Fe_2CO clusters, the CO π^* perpendicular to the Fe_2 axis had a more significant contribution involving the π backdonation from the Fe_2 clusters. Furthermore, the spin minority d electrons are mainly responsible for the π backdonation.

Due to problems with SCF convergence incurred during the Fe_xCO studies, we were forced to investigate a number of different techniques to achieve SCF convergence. Therefore,

techniques that generate starting guesses of the eigenvectors for the SCF procedure and techniques used to accelerate SCF convergence are reviewed. The standard guesses of H_{core} and charge build-up are examined, and we introduce a new incremental cluster method for generating starting guesses for larger clusters. The standard techniques of extrapolation, DIIS, damping, level shifting, restrict, and symmetry blocking are examined, and we also developed the hacker method and partial geometry optimization as new techniques to achieve SCF convergence. Results of the review indicate that the most important element for obtaining SCF convergence is the starting guess. A procedure for performing transition metal cluster calculations is outlined.

Table of Contents

Acknowledgements.....	iii
Abstract.....	v
List of Tables.....	ix
List of Figures.....	xii
List of Abbreviations.....	xiii
Chapter 1: Introduction.....	1
Clusters.....	3
Metal-CO Bonding.....	4
Calculations.....	9
Chapter 2: SCF Procedure.....	14
Hartree-Fock Theory.....	14
Initial Guess Techniques.....	18
H _{core}	21
Charge Build-up.....	24
CONAVE.....	29
β CI.....	31
Expanded Basis Set.....	39
Incremental Cluster.....	42
Techniques to Achieve SCF Convergence.....	46
Extrapolation.....	47
DIIS.....	48
Damping.....	52
Level Shifting.....	53
Restrict.....	55

Symmetry Blocking.....	58
Hacker.....	60
Geometry Optimization.....	67
Conclusion.....	70
Chapter 3: Constrained Space Orbital	
Variation.....	74
CSOV Method.....	74
Orthogonalization.....	78
Subunits.....	82
Fock Matrices.....	90
DIIS.....	92
Chapter 4: Aluminum on Graphite	
Computational Details.....	96
Results and Discussion.....	98
Conclusion.....	108
Chapter 5: Fe_xCO Clusters.....	109
Computational Details.....	112
Experimental Geometry Calculations.....	114
Geometry Optimization Calculations.....	133
CO (C _{4v}).....	136
FeCO (C _{4v}).....	137
Fe ₂ CO (C _{2v}).....	147
Fe ₂ CO (C _s).....	161
Conclusion and Future Studies.....	174
References.....	178

List of Tables

<u>Table</u>	<u>Page</u>
2.1 Initial Guess with H _{core}	23
2.2 Initial Guess with Charge Build-up.....	26
2.3 CONAVE Results.....	30
2.4 β CI Results.....	38
2.5 Convergence Acceleration Techniques.....	51
2.6 State Loyalty Techniques: Damping and Level Shifting.....	56
2.7 State Loyalty Techniques: Restrict and Symmetry Blocking.....	59
2.8 Hacker and Perturbation Hacker Results.....	64
2.9 Hacker and Perturbation Hacker Results.....	66
2.10 Convergence versus Geometry Optimization.....	69
3.1 Schmidt Orthogonalized: Fe-CO-Fe.....	84
3.2 Symmetrically Orthogonalized: Fe-CO-Fe.....	85
3.3 Schmidt Orthogonalized: CO-Fe-CO.....	86
3.4 Symmetrically Orthogonalized: CO-Fe-CO.....	87
4.1 Equilibrium C-Al Bond Length(d), Al Binding Energy(BE), Charge(q).....	101
4.2 CSOV Energy Analysis for the Different Adsorption Sites.....	106
5.1 CSOV Analysis for FeCO(C _{4v}) $^5\Sigma^-$ State: Full Basis Set.....	120

5.2	CSOV Analysis for $\text{Fe}_2\text{CO}(\text{C}_{2v})$: Full Basis Set.....	121
5.3	CSOV Analysis for $\text{Fe}_2\text{CO}(\text{C}_s)$: Full Basis Set.....	122
5.4	SCF Mulliken Majority(α) and Minority(β) Population.....	128
5.5	Irreducible Representations Spanned by the Atomic Orbitals Used by the Fe_xCO Clusters.....	134
5.6	Optimized $\text{CO}(\text{C}_{4v})$	136
5.7	Geometry Optimization Results for $\text{FeCO}(\text{C}_{4v})$	138
5.8	CSOV Study for $\text{FeCO}(\text{C}_{4v})$ $^5\Sigma^-$: Pseudopotential Basis Set.....	141
5.9	CSOV Study for $\text{FeCO}(\text{C}_{4v})$ $^5\Sigma^-$: Full Basis Set.....	142
5.10	Singles and Doubles CI calculation for $\text{FeCO}(^5\Sigma^-)$..	145
5.11	Geometry Optimization Results for $\text{Fe}_2\text{CO}(\text{C}_{2v})$: Pseudopotential Basis Set.....	149
5.12	CSOV Study for $\text{Fe}_2\text{CO}(\text{C}_{2v})$ $^7\text{A}_2$: Pseudopotential Basis Set.....	153
5.13	Geometry Optimization Results for $\text{Fe}_2\text{CO}(\text{C}_{2v})$: Full Basis Set.....	157
5.14	CSOV Study for $\text{Fe}_2\text{CO}(\text{C}_{2v})$ $^7\text{A}_2$: Full Basis Set.....	160
5.15	Geometry Optimization Results for $\text{Fe}_2\text{CO}(\text{C}_s)$: Pseudopotential Basis Set.....	163

5.16 CSOV Study for $\text{Fe}_2\text{CO}(\text{C}_s)$ ${}^7\text{A}''$: Pseudopotential Basis Set.....	166
5.17 Geometry Optimization Results for $\text{Fe}_2\text{CO}(\text{C}_s)$: Full Basis Set.....	172
5.18 CSOV Study for $\text{Fe}_2\text{CO}(\text{C}_s)$ ${}^7\text{A}''$: Full Basis Set.....	173

List of Figures

<u>Figure</u>	<u>Page</u>
2.1 Summary of the SCF Procedure.....	19
2.2 Convergence Behavior.....	22
2.3 Incremental Cluster Technique for $\text{Fe}_3\text{CO}(\text{C}_{2v})$	43
2.4 $\text{Al}_2\text{CO}(\text{C}_s)$ Cluster for the Hacker Studies.....	63
2.5 $\text{Fe}_4\text{CO}(\text{C}_{4v})$ Geometry.....	68
2.6 Procedure for Transition Metal Clusters.....	73
3.1 General CSOV Steps.....	79
3.2a Schmidt and Symmetric Orthogonalization: A = Fe B = CO.....	83
3.2b Schmidt and Symmetric Orthogonalization: A = CO B = Fe.....	83
4.1 Aluminum on Graphite Clusters.....	99
4.2 CSOV Steps for the Aluminum on Graphite Clusters.....	105
5.1 CO Adsorption on Fe(100) Surface.....	110
5.2 Fe_xCO Clusters.....	111
5.3 CSOV Steps for the Fe_xCO Clusters.....	117
5.4 Occupied Majority(α) and Minority(β) Spin Orbital Energies.....	130
5.5 CSOV Steps for the $\text{Fe}_2\text{CO}(\text{C}_{2v})$ Clusters.....	151
5.6 CSOV Steps for the $\text{Fe}_2\text{CO}(\text{C}_s)$ Clusters.....	165

List of Abbreviations

a.u.	Atomic Units
eV	Electron Volts
GAMESS	General Atomic and Molecular Electronic Structure Systems: Hartree-Fock <i>ab initio</i> program
UHF	Unrestricted Hartree-Fock
CI	Configuration Interaction
CONAVE	Configuration Average
β CI	Beta Configuration Interaction
DIIS	Direct Inversion of the Iterative Subspace
CSOV	Constrained Space Orbital Variation

Chapter 1

Introduction

With the advent of ultrahigh vacuum experimental techniques, such as scanning tunneling microscopy, it is now possible to study surface-adsorbate interactions at the atomic level.¹ With this information one can begin to determine structural-chemical relationships necessary for efficient catalysis. For example, due to its importance in the Fischer-Tropsch Synthesis, there has been much interest in the chemisorption of CO on Fe surfaces in the last decade.²⁻¹²

On the clean Fe(100) surface, temperature programmed desorption (TPD) studies show that the CO adsorbs molecularly in three sequentially filled states.³ The structure of the initially filled and most tightly bound state CO(α_3) has recently been determined using X-ray photoelectron diffraction (XPD)⁴ and consists of the CO molecule, most probably lying in the 4-fold hollow site tilted at a 55° with respect to the Fe(100) surface normal. This CO(α_3) state is of considerable interest, because it is believed to represent a precursor state for the dissociation of CO on the Fe surface. The two other states CO(α_1) and CO(α_2) desorb CO molecularly with desorption activation energies of 12.8 and 18.0 kcal/mole respectively, while the more tightly bound CO(α_3) has a 26.2 kcal/mole desorption activation energy.³

Moon et al. have assigned CO stretching frequencies of 2070, 2010, and 1210 cm^{-1} to the $\text{CO}(\alpha_1)$, $\text{CO}(\alpha_2)$, and the $\text{CO}(\alpha_3)$ states, respectively.⁵ $\text{CO}(\alpha_1)$ and $\text{CO}(\alpha_2)$ have typical metal carbonyl stretching frequencies; however, the $\text{CO}(\alpha_3)$ frequency indicates substantial C-O bond weakening which is consistent with being a precursor to dissociation. Photoemission experiments have also found CO-Fe(100) substrate interaction peaks.^{11,12} The more recent experiments by Brookes et al.¹² are in general agreement with those performed earlier by Benndorf et al.¹¹ In the $\text{CO}(\alpha_3)$ spectra Brookes et al. find two peaks at 8.0 and 12.0 eV binding energy which are attributed to emission from a mixed ($1\pi+5\sigma$) CO level and from a 4σ CO level, respectively. At higher CO surface coverage with the $\text{CO}(\alpha_2)$ and $\text{CO}(\alpha_3)$ states present, Brookes et al., find three peaks at 10.9, 8.1, 7.1 eV binding energy which are assigned to the 4σ , 1π , and 5σ levels for a vertical CO species.¹¹ In addition Brookes et al. have performed a spin polarized photoemission study where they find in the $\text{CO}(\alpha_3)$ spectra a minority spin peak at 1.7 eV binding energy and a majority spin peak at 2.3 eV binding energy.¹² A tilted CO structure has also been observed on other transition metal surfaces.¹³ Because the findings are unusual and the CO tilt angle on Fe(100) is well defined, we decided to investigate the chemisorption of CO on the Fe(100) surface.

Clusters

Another manner to study these surface chemical processes is to use quantum mechanical calculations. Calculations can offer information or predict adsorption structures even in situations where it is experimentally inaccessible. The main problem with modeling surface interactions is the infinite dimension of solids. Obviously, one could not directly include an infinite or near infinite number of atoms in any calculation. Consequently, this demands alternative solutions to solve this problem.

One solution is to perform slab calculations.¹⁴⁻¹⁶ Here, the surface is modelled by several layers of atoms to produce a slab. The 2-dimensional periodic symmetry of the slab is used to make the calculation into a manageable form. As a consequence, slab calculations are useful for investigating an ordered overlayer on a surface. However, a chemical reaction such as that which must occur in catalysis is more likely to be a local phenomenon.

An alternative method, which better models local phenomena of chemisorption, is the use of clusters.¹⁷⁻²¹ When performing a cluster calculation, one essentially extracts a section of the solid material from the bulk that would best represent the system to be studied. The obvious advantage of using clusters is that the size of the problem can be conveniently contracted to a computationally tractable limit.

It also need not be constrained to any periodic boundary conditions. Thus, many different structures and systems without symmetry can be studied.

However, with the simplifications come the drawbacks. Clearly, in clusters the environmental effects are not being included nor the band structure of the bulk solid. Because the cluster is finite, this creates edge effects or "dangling bonds" associated with the cluster. These become less significant as the cluster size is increased, but then the limits of the calculations can often be rapidly approached. "Dangling bonds" cause problems associated with the convergence of the adsorbate properties to the observed properties of the bulk. In particular the binding energy of adsorbates has been shown to change drastically with cluster size.⁶⁰ Panas et al.⁶¹ have outlined a technique to achieve better convergence of binding energies using clusters, and we, too, will introduce a new technique to overcome this problem in chapter 2.

Metal-CO Bonding

To understand the bonding that occurs in the chemisorption of CO on Fe, we first need to understand the bonding between CO and metals. There have been numerous theoretical investigations on CO to transition metal bonding.²² Orgel introduced the idea that the metal carbonyl

bond is a dative bond, where the σ lone pair on the CO donates into the metal, and the metal backdonates into the CO $2\pi^*$ orbital.²³ Subsequently, the backdonation into the $2\pi^*$ causes the weakening of the CO bond, which is so characteristic in carbonyl complexes.²⁴ This is usually measured by the decrease in vibrational frequency of the CO, where free CO has a C-O stretch of 2143 cm^{-1} .²⁵ In neutral carbonyl complexes the CO stretching frequency can range from $1800\text{--}2200\text{ cm}^{-1}$, and the bridging CO stretch can range from $1700\text{--}1860\text{ cm}^{-1}$.²⁴

Hillier and Saunders performed *ab initio* calculation on $\text{Ni}(\text{CO})_4$ and $\text{Cr}(\text{CO})_6$ to measure any backdonation via Mulliken Population analysis.²⁶ The charge calculated on the Ni and the Cr were $+0.47$ and $+0.20$, respectively, asserting donation from the metal to the CO ligands. In the population analysis the C $2s$ population decreased by 0.1 indicating σ donation from the CO lone pair, and the $2p\pi$ population increased by 0.2 confirming the π backdonation.

There was controversy concerning the backdonation mechanism,²⁷⁻³¹ where Johnson and Wahlgren observed no backdonation in their MS $X\alpha$ calculations on $\text{Ni}(\text{CO})_4$.^{27,28} This was repudiated by Larsson and Braga, who repeated the same calculations and concluded there is backdonation.²⁹ Additional MS $X\alpha$ calculations by Veillard³⁰ and Fenske³¹ also confirmed backdonation.

Using the CSOV method,^{101,102} Bagus et al. were able to determine the energetics of the σ and π interaction between Cu and CO.^{32,33} They found for CuCO that the π backdonation contributed 0.20 eV to the total energy versus 0.09 eV from the σ donation. This asserts that the π backdonation is even more important than the σ donation. In another CSOV study done on Ni(CO)₄ and Fe(CO)₅, similar conclusions were made.³⁴ The π backdonation for the Ni(CO)₄ was found to be 5.09 eV compared with 0.27 eV for the σ donation. For Fe(CO)₅, the π backdonation was calculated to be 6.67 eV versus 2.41 eV from the σ donation. The σ donation is more substantial in the Fe complex, which is rationalized by there being fewer d electrons in the Fe allowing more σ donation. Even so, the π backdonation is still more significant. Pearson developed an electronegativity model for metal-carbonyl bonding, where the metal is a Lewis base, and the CO is a Lewis acid.³⁵ This also implies that the π backdonation from the metal is more important in the binding.

Although the π backdonation has been shown to be more significant, there are cases when σ donation from the CO is the overriding factor. Mn(CO)₆⁺ has a stretching frequency of 2090 cm⁻¹, which is very close to the free CO value.³⁶ It is also inert to CO substitution indicating very strong bonds. CO absorbed on ZnO has a stretching frequency equal to 2202 cm⁻¹, which is above the free CO value. The binding energy of

the adsorption is 12.0 kcal/mole, which is on the order of the $\text{CO}(\alpha_1)$ binding energy for the Fe(100) surface.³⁷

Despite these anomalies, the σ donation π backdonation mechanism describes the bonding in metal carbonyl complexes very well for CO end on binding. There are cases, however, where CO has a distorted geometry in carbonyl complexes.^{24, 38} The CO stretching frequency of semi-bridged and μ_3 bonded CO complexes can be as low as 1200 cm^{-1} . Hoffmann provides a qualitative MO description for bending CO out of a linear position into a side on position.³⁹ Because the symmetry of the complex changes as the CO bends, this allows other d orbitals to mix with the CO orbitals. This basically is the same mechanism as before except now other d orbitals can backdonate into the CO $2\pi^*$ orbital. Also, the σ lone pair and the π orbital hybridize to provide σ and π donation into the metal.

For chemisorption of CO on metal surfaces, Blyholder extended the Orgel description to explain chemisorption behavior.⁴⁰ Using the CSOV analysis, Bagus et al. demonstrated for the on top vertical adsorption of CO on a Cu_5 cluster that π backdonation dominated the binding as with carbonyl complexes.³² The backdonation contributed 0.32 eV to the total energy versus 0.12 eV attributed to the σ donation from the CO. Calculations done by Blomberg et al. on linear PdCO and bridging Pd₂CO to model the chemisorption of CO on Pd also showed significant backdonation.⁴¹ The corresponding

Mulliken populations were 0.40 and 0.54 in the $2\pi^*$ orbital indicating even more backdonation from the Pd_2 . Currently, the Blyholder model is the accepted bonding picture for vertical adsorption of CO.

However, Avouris et al. introduced a new aspect into the bonding model of CO on metal surfaces based on calculations done on $FeCO^-$ and $CuCO^-$.⁴² By adding an electron to FeCO and CuCO, the $2\pi^*$ orbital hybridized with the $4p\pi$ orbital of the metal producing new bonding and antibonding orbitals. Therefore, mixture with the unoccupied $4p\pi$ level also contributes to the bonding of CO on metal surfaces.

As one moves across the first row transition metals, an interesting trend of CO desorption occurs. To the left of Co, CO dissociates upon desorption. To the right of Co, including Co, CO desorbs molecularly.⁴³ This is rationalized by the atomic adsorption versus the molecular adsorption. In the first set of transition metals the atomic adsorption is stronger than the molecular adsorption. Consequently, the atomic adsorption is an overriding effect compared to the CO bond strength. To the right of Co, the atomic adsorption is not strong enough to break the CO bond. To explain the behavior of CO on the first row transition metals, Sung and Hoffmann performed band calculations of the extended Huckel type.⁴⁴ Dissociation is rationalized by the higher Fermi level of the transition metals to the left of Co. This causes more backdonation into the $2\pi^*$ orbital, and, subsequently, a

weaker CO bond. The change in electron density of the CO for the σ lone pair and $2\pi^*$ orbitals is calculated to be greatest from Ti to Fe. Breakage of the CO bond is rationalized by the weaker bond and increased side ways motion of the CO. Their calculations also predict that the high index adsorption site is more favorable to dissociation, which is the case for Fe(100).

Calculations

Currently, there are three popular methods for performing cluster calculations: semi-empirical methods, density functional theory, and *ab initio*.⁴⁵ When choosing a method for transition metals, one factor to consider is electron correlation. This is born out of the d and f electrons, which are confined in a small space with respect to the number of electrons. There is ample evidence that the lack of correlation produces energies that vary greatly from experimental values.⁴⁵⁻⁴⁷ In order to calculate the energetics of transition metals correctly one must calculate electron correlation accurately. Semi-empirical methods use experimental information to correct for electron correlation. Density functional theory, which incorporates an approximation to correct for electron correlation, and *ab initio* calculations are non-empirical methods to calculate energies. Attempts to use semi-empirical methods produced

binding energies between two Fe atoms that were much too high. Density functional calculation were not available to us, and, therefore, we chose *ab initio* methods.

Ab initio calculations are usually started by performing Hartree-Fock calculations. Hartree-Fock calculations neglect electron correlation, which is a shortcoming. Therefore, post Hartree-Fock calculations are essential for obtaining more quantitative energies for transition metals. Even so, one needs to start at the Hartree-Fock level to produce the higher level calculations. Also, Hartree-Fock calculations provide a useful qualitative description of the molecular orbitals in our system of interest. More importantly, Hartree-Fock calculations do predict geometries very well.⁴⁵ For these reasons we only use Hartree-Fock theory here.

Even with the Hartree-Fock calculations alone, results were still very difficult to obtain. This is due an incomplete filling of the d orbitals creating many low lying energy states or quasi-degenerate states.⁴⁵⁻⁴⁷ This causes many problems with SCF convergence and determining the correct ground state. Furthermore, the closeness in energy of the states often leads to a switching of states during the SCF cycle. Once a calculation is converged, then there still is a possibility that it is trapped in an excited state.

Not only are the d orbitals partially filled, but the valence s orbital can also change its occupation. For the first row transition metals the configuration can be

$4s^23d^{n-2}$, $4s^13d^{n-1}$, or $3d^n$. This creates a problem of choosing a particular 4s-3d configuration. One could attempt to calculate the energy for all possible 4s-3d occupations, but the number of calculations involved becomes rapidly large. For instance, Fe has a ground state configuration of s^2d^6 (5D). This equates to 5 different possible occupations for the d^6 electrons. If we have Fe_2 at a multiplicity of 9, then the resultant configuration would be s^2d^6 for each Fe atom. The d occupation now has 100 different permutations. One additional Fe has increased the number of possible permutations by 20 fold without including the $4s^1d^7$ and d^8 configurations.

Lastly, there is the matter of choosing the spin of the transition metal system. Instead of a multiplicity of 9 for Fe_2 , we can choose a multiplicity of 7. This is derived by using the $4s^13d^7$ configuration for each Fe and spin coupling the s electrons. The number of different d occupation is now 230 with a multiplicity of 7.

In practical terms, transition metals usually require very large basis sets. Single zeta basis sets are not adequate.⁴⁵⁻⁴⁹ This is again due to the fact transition metals can have configuration of $4s^23d^{n-2}$, $4s^13d^{n-1}$, or $3d^n$. Hay demonstrated that optimizing a basis set for one configuration can lead to gross errors in the other configurations.⁴⁹ Therefore, double and triple zeta basis sets need to be used to compute adequate energies. Also, a

larger basis set reduces the amount of basis set superposition error.^{48,49} Yet, the computer time needed for large basis set calculations can increase to the point that the calculation becomes intractable. Replacing the core electrons with pseudopotentials is one convenient method for reducing the number of basis functions.^{48,120} This can expedite the calculation considerably, although caution is still needed, because the fixed core may affect trends in the calculations.

In this thesis we present new information regarding the chemisorption of CO on Fe in light of the current theories and experimental data. The Fe_xCO cluster calculations, which include optimizing the CO position, aid this process. Additional studies on other transition metal clusters would contribute to the complete picture of CO adsorption, but this is beyond the scope of this thesis. In chapter 5 are the results and discussions of our Fe_xCO clusters. Chapter 3 describes the constrained space orbital variation (CSOV) technique, which has been used extensively on the Fe_xCO clusters for determining the major bond interactions between the CO and Fe_x clusters. Chapter 4 is an illustrative application of the CSOV technique performed on aluminum-graphite clusters. Chapter 2 outlines Hartree-Fock theory and the SCF procedure. Many standard techniques are discussed that are designed to determine the ground state for a cluster and achieve SCF convergence. However, as is shown, we were

forced to design new techniques in order to achieve SCF convergence on the Fe_xCO clusters. Thus, a general scheme for approaching calculations on transition metal clusters is reported at the end of chapter 2.

Chapter 2

SCF procedure

Hartree-Fock Theory

Because of the problems associated with calculations on transition metals, we essentially went back to basics to develop strategies for efficiently performing the calculations. To do this we first need to review the Self Consistent Field (SCF) procedure and how we can better utilize it to obtain results for the Fe clusters.

In Hartree-Fock SCF theory the pseudoeigenvalue problem is solved iteratively,

$$\underline{\underline{F}} \underline{\underline{C}} = \underline{\underline{S}} \underline{\underline{C}} \underline{\underline{E}} \quad (2.1)$$

where F is the Fock matrix, C is the coefficient matrix, S is the overlap matrix, and E is the diagonal eigenvalue matrix.⁵⁰ An initial basis set $\{\phi\}$ is selected. The resultant molecular orbitals, Ψ_i , are related to the basis set through

$$\Psi_i = \sum_{\mu} \phi_{\mu} C_{\mu i} \quad (2.2)$$

where $C_{\mu i}$ is the expansion coefficient on the basis function. Using this basis set the Fock matrix elements are calculated by

$$F_{\mu\nu} = H_{\mu\nu\text{core}} + \sum_{\lambda\sigma} P_{\lambda\sigma} [(\mu\nu|\lambda\sigma) - 1/2(\mu\lambda|\sigma\nu)] \quad (2.3)$$

H_{core} is the core Hamiltonian matrix including the one electron operators involving the kinetic energy and nuclear attraction potential of the electron. It is defined by

$$H_{\mu\nu\text{core}} = \int \phi_{\mu}^*(1) (1/2\nabla^2(1) - \sum_A Z_A/r_{1A}) \phi_{\nu}(1) d\tau_1 \quad (2.4)$$

$(\mu\nu|\lambda\sigma)$ is the 2 electron integral defined by

$$(\mu\nu|\lambda\sigma) = \int \phi_{\mu}^*(1) \phi_{\nu}(1) 1/r_{12} \phi_{\lambda}(2) \phi_{\sigma}(2) d\tau_1 d\tau_2 \quad (2.5)$$

and it is calculated for all the basis functions. P is the density matrix defined by

$$P_{\lambda\sigma} = 2 \sum_a C_{\lambda a} C_{\sigma a}^* \quad (2.6)$$

where "a" sums over all of the occupied orbitals. If we let

$$G_{\mu\nu} = \sum_{\lambda\sigma} P_{\lambda\sigma} [(\mu\nu|\lambda\sigma) - 1/2(\mu\lambda|\sigma\nu)] \quad (2.7)$$

then

$$\underline{F} = \underline{H} + \underline{G} \quad (2.8)$$

The overlap matrix between two basis functions is defined by

$$S_{\mu\nu} = \int \phi_{\mu}(1) \phi_{\nu}(1) d\tau_1 \quad (2.9)$$

and the orthonormality constraint on the molecular orbitals requires the coefficient matrix to obey with respect to the overlap matrix

$$\underline{\underline{C}}^+ \underline{\underline{S}} \underline{\underline{C}} = \underline{\underline{1}} \quad (2.10)$$

The Hartree-Fock calculation is iterative, because F is dependent upon P , which is formed from C . An initial guess at P is needed to form G .

After the Fock matrix is formed, we want to convert equation 2.1 into an eigenvalue problem for a symmetric matrix

$$\underline{\underline{F}}' \underline{\underline{C}}' = \underline{\underline{C}}' \underline{\underline{E}} \quad (2.11)$$

This is done usually in two ways: symmetric and canonical orthogonalization. First we let

$$\underline{\underline{C}} = \underline{\underline{X}} \underline{\underline{C}}' \quad (2.12)$$

and the eigenvalue problem now becomes

$$\underline{\underline{F}} \underline{\underline{X}} \underline{\underline{C}}' = \underline{\underline{S}} \underline{\underline{X}} \underline{\underline{C}}' \underline{\underline{E}} \quad (2.13)$$

Multiplying both sides of equation 2.13 by X^+ yields

$$\underline{\underline{X}}^+ \underline{\underline{F}} \underline{\underline{X}} \underline{\underline{C}}' = \underline{\underline{X}}^+ \underline{\underline{S}} \underline{\underline{X}} \underline{\underline{C}}' \underline{\underline{E}} \quad (2.14)$$

Equation 2.11 is obtained when $\underline{\underline{X}}^+ \underline{\underline{S}} \underline{\underline{X}} = \underline{\underline{1}}$, and $\underline{\underline{X}}^+ \underline{\underline{F}} \underline{\underline{X}} = \underline{\underline{F}}'$.

In symmetric orthogonalization

$$\underline{\underline{X}} = \underline{\underline{S}}^{-1/2} \quad (2.15)$$

where $S^{-1/2}$ is the inverse square root of the overlap matrix.

In canonical orthogonalization

$$\underline{\underline{X}} = \underline{\underline{U}} \underline{\underline{s}}^{-1/2} \quad (2.16)$$

where U is a unitary matrix and $s^{-1/2}$ is the diagonal matrix of the inverted square roots of the overlap matrix eigenvalues. Consequently, diagonalizing F' will yield the eigenvalues and the eigenvectors. To transform back to the new non-orthogonal coefficient matrix, equation 2.12 is utilized.

In the GAMESS program⁵¹ the transformation is slightly different, and C^+ is used as the transformation matrix.

$$\underline{\underline{C}}^+ \underline{\underline{F}} \underline{\underline{C}} = \underline{\underline{C}}^+ \underline{\underline{S}} \underline{\underline{C}} \underline{\underline{E}} \quad (2.17)$$

Since $\underline{\underline{C}}^+ \underline{\underline{S}} \underline{\underline{C}} = \underline{\underline{1}}$, then $F' = \underline{\underline{C}}^+ \underline{\underline{F}} \underline{\underline{C}}$. Diagonalizing F' will result in an eigenvector matrix near unity, $\underline{\underline{1}}'$, such that

$$\underline{\underline{F}}' \underline{\underline{1}}' = \underline{\underline{1}}' \underline{\underline{E}} \quad (2.18)$$

To transform back to the non-orthogonal coefficient matrix, C_{out} , the previous set of eigenvectors, C_{in} , are used.

$$\underline{\underline{C}}_{out} = \underline{\underline{C}}_{in} \underline{\underline{1}}' \quad (2.19)$$

At convergence $\underline{\underline{1}}' = \underline{\underline{1}}$. Regardless of the transformation of F , the new coefficient matrix, C , is then used to reform density matrix, P , which will yields a new F . Convergence is reached, when the absolute change in the density matrix, ΔP , or in energy, ΔE , is below some threshold. Typically a threshold of 10^{-4} and 10^{-8} a.u. are used for ΔP and ΔE , respectively. The SCF procedure is summarized in figure 2.1. The two elements that are crucial to the success of Hartree-Fock calculations are the initial guess at C and having techniques for efficiently reaching convergence. The remainder of this chapter analyzes these features in detail.

Initial Guess Techniques

In this section we will be investigating different initial guess routines necessary to start an SCF calculation. One problem associated with choosing a guess is that an electron in an occupied orbital experiences a potential due to $N-1$ electrons, while an electron in a virtual orbital

Summary of the SCF Procedure

1. Choose atomic positions and a basis set
 2. Calculate S , H_{core} , $(\mu\nu|\lambda\sigma)$
 3. Obtain transformation matrix X
 4. Guess at density matrix, P
 - 5. Form G and form F
 6. Transform F
 7. Diagonalize F'
 8. Backtransform C'
 9. Form new P
 10. if converged then finished
- else return to 5
-

Figure 2.1

experiences the potential due to N electrons. Also, the electrons in doubly occupied orbitals feel a different potential than the electrons in singly occupied orbitals due to the repulsion of two electrons in the same orbital. Therefore, in the case of transition metals, one may bias the d occupation by locking the calculation into an excited state.

The initial guess techniques we have examined are H_{core} , charge build-up, configuration average (CONAVE), βCI , expanded basis set, and incremental cluster. H_{core} , charge build-up, and CONAVE are techniques designed to equalize the potential felt by the d electrons. βCI is a new method developed in our laboratory, where it measures the energy of different d occupations. Instead of equalizing the potential felt by d electrons, βCI determines the best d occupation via the relative energies of the possible d occupations. The expanded basis set and incremental cluster do neither of the above, but rather they use information from smaller basis sets or smaller clusters to construct a starting guess for more complicated systems.

To judge the quality of H_{core} versus charge build-up, we performed calculations on $\text{FeCO}(\text{C}_{4v})$. All $\text{FeCO}(\text{C}_{4v})$ calculations were performed using the full basis set described in chapter 5. The geometry was taken as the theoretically optimized free CO bond length (1.14 Å) combined with a typical experimental Fe-C separation (1.85 Å). A $^5\Sigma^-$

ground state with -1374.969870 a.u. energy was found at this geometry. This will be designated as the target energy. Unless convergence was reached each calculation was performed with a maximum of 50 cycles. In the tables giving results for the different methods, each calculation is listed as converged, converging, or oscillating. An oscillating calculation means the Hartree-Fock energy is not monotonically decreasing. Figure 2.2 shows the typical energy variation with the SCF cycle number for a calculation that converges smoothly and one that oscillates. The quality of each initial guess technique will be evaluated based on their ability to produce the target energy and to converge the calculation.

H_{core}

When $\underline{G} = \underline{0}$ in equation 2.8, H_{core} becomes the starting Fock matrix. This is a means of negating the different potential felt by the electrons in the occupied and virtual orbitals, because the density matrix is set equal to zero. H_{core} is a simple means to produce a starting guess, but it is also a very poor starting guess. The neglect of the 2 electron integrals is simply too crude.⁵²

In Table 2.1 the data is listed for 4 calculations using different convergence techniques starting from H_{core}. In every calculation H_{core} failed to produce the target energy.

Convergence Behavior

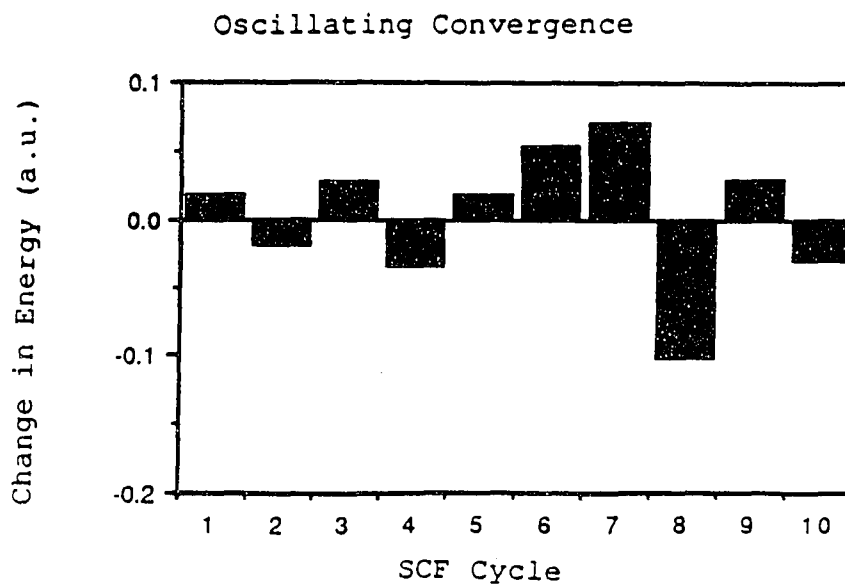
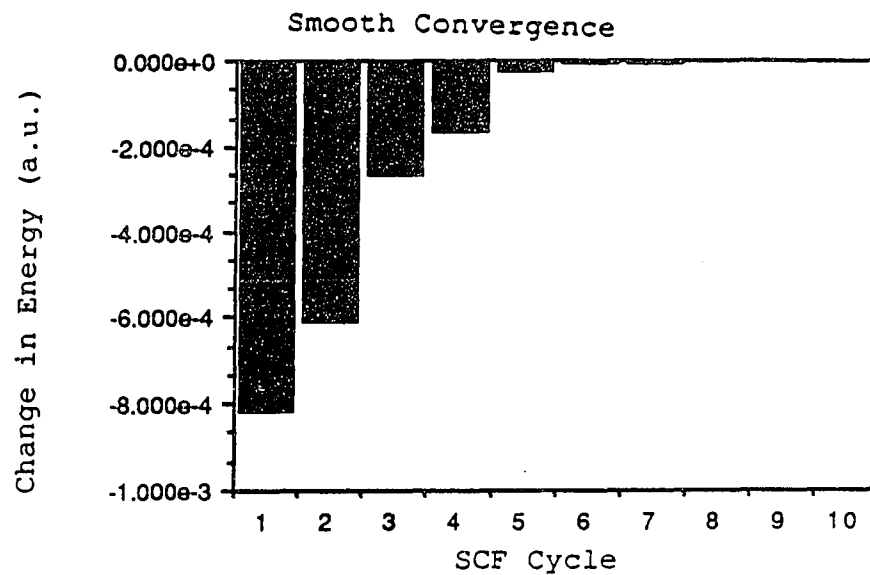


Figure 2.2

Table 2.1
Initial guess with H_{core}

Target Energy = -1374.969870 a.u.

Convergence		Final Energy	Number of SCF
<u>Technique</u>	<u>Behavior</u>	<u>(a.u.)</u>	<u>Cycles</u>
Extrapolation	oscillating	-1374.890814	50
DIIS	oscillating	-1236.665522	50
Damping	oscillating	-1374.537703	50
Level shifting	converging	-1374.755955	50

Only when level shifting is used does the H_{core} calculation start to converge but at a higher energy. The final energy of this calculation is 0.21 a.u. above the target energy. Clearly, H_{core} has produced an excited state. The closest energy to the target energy is 0.08 a.u. above the target energy, when extrapolation is used. Even DIIS, which is a superior acceleration technique, could not produce an adequate energy on the $\text{FeCO}(\text{C}_{4v})$ calculation.

Yet, H_{core} must be used at some point in a calculation, unless the eigenvectors from a minimum basis set or an extended Huckel calculation are used as starting vectors. Because the full basis set precludes the use of a minimum basis set (MINGUESS in GAMESS) or an extended Huckel guess (EXTGUESS in GAMESS), these choices as starting guess were not used.

Charge Build-up

Another technique to develop starting eigenvectors is the "charge build-up" technique.^{53,54} To begin the charge build-up technique, one starts with H_{core} and places a charge on the cluster. Then the resulting eigenvectors from this calculation are used to start another charged calculation or begin the no charge calculation. The charge build-up technique has worked fairly well in our research, in particular, for high symmetry cases. However, there are some

disadvantages. One is that the most efficient charge build-up scheme needs to be reinvestigated for each new cluster treated, because it may vary between different systems. This may prove to be costly concerning computer time.

For example, in the $\text{FeCO}(\text{C}_{4v})$ cluster, Fe has 26 electrons, of which 18 are paired core electrons, leaving 8 valence electrons to occupy the 4s and 3d orbitals. The 6α electrons completely occupy the 4s and 3d orbitals, while the 2β electrons can occupy any two of these six orbitals. If the 2β electrons are removed to give a charge of +2 and a multiplicity of 7, this will make each of the the 4s and 3d α orbitals singly occupied. Of course, one could also put a charge of +8 and a multiplicity of 1 placing the 4s and 3d orbitals in the virtual space. Likewise, a charge of -4 and a multiplicity of 1 would be a similar idea to the charge of +8 by placing each orbital in the doubly occupied space. The CO orbitals are left doubly occupied as in free CO. In Table 2.2 results for the $\text{FeCO}(\text{C}_{4v})$ cluster using the charge build-up scheme started from each of these charge build-up schemes are reported.

For the $\text{FeCO}(\text{C}_{4v})$ cluster, a charge of +2 in the charge build-up scheme produced the best results. The charge of -4 did have one calculation converging, but the final energy is 0.72 a.u. above the target energy. The other calculations were oscillating with respect to convergence. Obviously, the charge of -4 did not produce a good starting point for the no

Table 2.2

Initial Guess with Charge Build-up

Target Energy = -1374.969870 a.u.

Charge = +2

Convergence		Final Energy	Number of SCF
<u>Technique</u>	<u>Behavior</u>	<u>(a.u.)</u>	<u>Cycles</u>
Extrapolation	converging	-1374.969555	50
DIIS	converged	-1374.969870	16
Damping	converging	-1374.969856	50
Level shifting	converged	-1374.969870	50

Charge = -4

Convergence		Final Energy	Number of SCF
<u>Technique</u>	<u>Behavior</u>	<u>(a.u.)</u>	<u>Cycles</u>
Extrapolation	oscillating	-1278.154474	50
DIIS	oscillating	-1236.665522	50
Damping	oscillating	-1350.144248	50
Level shifting	converging	-1374.251014	50

Table 2.2 (continued)
Initial Guess with Charge Build-up

Target Energy = -1374.969870 a.u.

Charge = +8

Convergence		Final Energy	Number of SCF
<u>Technique</u>	<u>Behavior</u>	<u>(a.u.)</u>	<u>cycles</u>
Extrapolation	converging	-1374.969861	50
DIIS	oscillating	-1240.201226	50
Damping	oscillating	-1361.438707	50
Level shifting	converged	-1374.791461	50

charge calculation. The charge of +8 was also not a very good starting point, even though the calculation with extrapolation was converging to the target energy. Yet, when level shifting was used, the calculation converged to an excited state 0.18 a.u. above the target energy. This demonstrates that the charge of +8 did not produce good starting vectors.

These calculations have demonstrated that the charge build-up scheme can produce the proper ground state, if the charge build-up is correct. Different charge build-up schemes produce different states, and this is an important consideration when using the charge build-up technique. We found this to be the case for the $\text{Fe}_2\text{CO}(\text{C}_{2v})$ pseudopotential calculations, where the charge build-up produced an excited state rather than the ground state. Furthermore, Cox and Bauschlicher have also reported similar problems with the charge build-up technique for their Be_{10} and Be_{15} cluster calculations.⁵⁴ For systems with low symmetry, such as $\text{Fe}_2\text{CO}(\text{C}_s)$, charge build-up did not help with finding the correct ground state. Despite its problems, the charge build-up technique enables one to find a ground state in many cases and has certainly proven to be superior to Hcore.

CONAVE

Another technique used in our research is the configuration average technique (CONAVE).⁵⁵ In this technique the d orbital potential between the occupied and the virtual orbitals is equalized by computing the average SCF energy for a number of different electronic configurations. Based on this average, the best d orbital occupancy correspond to the lowest energies of the occupied orbitals. The lower the molecular orbital energy, the more favorable the d occupation.⁵⁵

The CONAVE is performed as an ROHF calculation, but these vectors can easily be adapted to start a UHF calculation. The eigenvectors from the ROHF calculation are used as starting α and β orbitals. This procedure was used on the $\text{Fe}_2\text{CO}(\text{C}_s)$ geometry as shown in figure 5.2c, which was the most problematic concerning convergence. The C-O distance was placed at 1.140 Å, and the CO distance from the z axis was varied. In Table 2.3 are the results from the CONAVE calculations.

The resultant Fe_2 configuration from the CONAVE calculation was $d\pi^3d\pi^*3d\delta^3d\delta^*3d\sigma^1d\sigma^*14s\sigma^2$. As shown, the energy rose as the CO approached the Fe_2 , and the convergence looked promising. The calculations did converge at closer distances until the CO was 1.50 Å from the z axis. In this calculation the energy was oscillating drastically.

Table 2.3
CONAVE Results

CO distance* (Å)	Energy (a.u.)	Number of cycles
5.00	-155.741526	71
4.00	-155.738882	89
2.00	-155.514623	52
1.50	unconverged	150

* CO distance is the distance from the z axis.

Ultimately, the CONAVE technique did not solve the problems with the $\text{Fe}_2\text{CO}(\text{C}_S)$ cluster. Other problems concerning CONAVE are similar to the charge build-up technique, where an excited state might result from the calculation.

βCI

Hartree-Fock theory is based on a single determinant wavefunction and therefore does not calculate the exact energy. The difference between the Hartree-Fock energy and the non-relativistic exact energy is called the correlation energy, E_{corr} , expressed as

$$E_{\text{corr}} = \mathcal{E}_0 - E_0 \quad (2.20)$$

\mathcal{E}_0 is the exact energy, and E_0 is the Hartree-Fock ground state energy. The exact energy is the eigenvalue of the total wavefunction, $|\Phi_0\rangle$, such that

$$H|\Phi_0\rangle = \mathcal{E}_0|\Phi_0\rangle \quad (2.21)$$

One method to calculate a better energy is to use the configuration interaction method (CI). The wavefunction in a CI calculation is expressed as a linear combination of Slater determinants. Consequently, excited determinants are included in the total wavefunction. This yields the expression

$$|\Phi_0\rangle = C_0|\Psi_0\rangle + \sum_{a^r} C_{a^r}|\Psi_{a^r}\rangle + \sum_{ab^{rs}} C_{ab^{rs}}|\Psi_{ab^{rs}}\rangle + \text{higher excitations} \quad (2.22)$$

$|\Psi_0\rangle$ is the reference determinant, which is usually the Hartree-Fock ground state. $|\Psi_{a^r}\rangle$ is the singly excited determinant, where the virtual orbital r has replaced the occupied orbital a in the reference determinant. Likewise, $|\Psi_{ab^{rs}}\rangle$ is the doubly excited determinant and so on for triple excitations and higher. C is the contribution of each determinant.

If we designate single excitations as $|S\rangle$, double excitation as $|D\rangle$, and triple excitations as $|T\rangle$, we can easily construct the CI matrix as

$$(2.23)$$

	$ \Psi_0\rangle$	$ S\rangle$	$ D\rangle$	$ T\rangle$
$ \Psi_0\rangle$	$\langle\Psi_0 H \Psi_0\rangle$	0	$\langle\Psi_0 H D\rangle$	0
$ S\rangle$		$\langle S H S\rangle$	$\langle S H D\rangle$	$\langle S H T\rangle$
$ D\rangle$			$\langle D H D\rangle$	$\langle D H T\rangle$
$ T\rangle$				$\langle T H T\rangle$

According to Brillouin's theorem the matrix elements between the reference determinant and the singly excited determinants are zero, equation 2.24. Also, the matrix element is zero if two determinants differ by more than two orbitals, such as single and quadruple excitations, equation 2.25.

$$\langle \Psi_0 | H | S \rangle = 0 \quad (2.24)$$

$$\langle S | H | Q \rangle = 0 \quad (2.25)$$

Because converged calculations for the $\text{Fe}_2\text{CO}(\text{C}_s)$ geometry were very difficult to obtain, we decided the d occupation of the starting Fe_2 configuration may not have been optimum for this system. In order to obtain a better Fe_2 configuration, different combinations of the d orbital occupation would have to be examined. In Fe_2CO there are some 210 different possibilities, and, thus, we developed the β CI technique to expedite this process.

Normally, the CI matrix elements are derived from the molecular integrals of the SCF reference determinant, and indeed the molecular integrals are better suited for calculating the double excitation matrix elements. However, this costs a great amount of computer time. Therefore, in the β CI calculation we bypass the calculation of the molecular integrals and form a pseudo-full CI matrix from all the single excitations to produce the matrix elements.

Since the α d orbitals are all occupied, we only excite into all possible β d occupations. Then the first excited determinant becomes the reference determinant, and it is excited into all d occupations. The diagonal element for each determinant in the CI matrix is equal to the Hartree-Fock energy, E_{HF} , for that particular configuration.

$$\langle \Psi_0 | H | \Psi_0 \rangle = E_{HF} \quad (2.26)$$

$$\langle \Psi_a^r | H | \Psi_a^r \rangle = a^r E_{HF}$$

To calculate the elements between the reference determinants and single excitations, we use the rules for the one and two electron operators between determinants.⁵⁰

The Hamiltonian can be divided into one electron operators, $\sum_i h_i$, and two electron operators, $\sum_i \sum_j 1/r_{ij}$ $i < j$, such that

$$H = \sum_i h_i + \sum_i \sum_j 1/r_{ij} \quad (2.27)$$

For the one electron operators the matrix elements between two determinants that differ by one orbital is given by

$$\langle \Psi_0 | \sum_i h_i | \Psi_a^r \rangle = \langle a | h_1 | r \rangle \quad (2.28)$$

To convert this expression in terms of atomic integrals, we let

$$|r\rangle = \sum_v C_{vr} \phi_v \quad (2.29)$$

where C_{vr} is the coefficient of the atomic orbital, ϕ_v .

This yields the expression

$$\langle \Psi_0 | \sum_i h_i | \Psi_a^r \rangle = \sum_\mu \sum_v C_{\mu a} C_{vr} h_{\mu v} \quad (2.30)$$

Therefore, we have the one electron operator expressed in terms of the atomic one electron integrals, $h_{\mu\nu}$. For the two electron operators, which we designate as \hat{O}_2 , the matrix elements for the two electron operator between two determinants that differ by one orbital is given by

$$\langle \Psi_0 | \hat{O}_2 | \Psi_a^r \rangle = \sum_n [ar|nn] - [an|rn] \quad (2.31)$$

where n sums over all of the occupied orbitals in the reference determinant. The two electron molecular integral, $[an|rn]$, can be written in terms of atomic integrals, where

$$[an|rn] = \sum_{\mu\nu} C_{\mu a} C_{\nu r} [\sum_{\lambda} \sum_{\sigma} C_{\lambda n} C_{\sigma n} ((\mu\nu|\lambda\sigma) - (\mu\sigma|\lambda\nu))] \quad (2.32)$$

Therefore, equation 2.31 becomes

$$\begin{aligned} \sum_n [ar|nn] - [an|rn] = \\ \sum_{\mu\nu} C_{\mu a} C_{\nu r} [\sum_n \sum_{\lambda} \sum_{\sigma} C_{\lambda n} C_{\sigma n} ((\mu\nu|\lambda\sigma) - (\mu\sigma|\lambda\nu))] \end{aligned} \quad (2.33)$$

If we combine equations 2.30 and 2.33, then the matrix elements between the reference determinant and the singly excited determinants become

$$\begin{aligned} \langle \Psi_0 | H | \Psi_a^r \rangle = \langle r | \sum_i h_i + \hat{O}_2 | a \rangle = \\ \sum_{\mu} \sum_{\nu} C_{\mu a} C_{\nu r} h_{\mu\nu} + \\ \sum_{\mu\nu} C_{\mu a} C_{\nu r} \sum_n \sum_{\lambda} \sum_{\sigma} C_{\lambda n} C_{\sigma n} ((\mu\nu|\lambda\sigma) - (\mu\sigma|\lambda\nu)) \end{aligned} \quad (2.34)$$

Rearranging equation 2.34 will yield

$$\sum_{\mu} \sum_{\nu} C_{\mu a} C_{\nu r} [h_{\mu\nu} + \sum_n \sum_{\lambda} \sum_{\sigma} C_{\lambda n} C_{\sigma n} ((\mu\nu|\lambda\sigma) - (\mu\sigma|\lambda\nu))] \quad (2.35)$$

and the term in the brackets is equal to the Fock matrix element, $F_{\mu\nu}$, in the reference Fock matrix."

$$F_{\mu\nu} = h_{\mu\nu} + \sum_n \sum_{\lambda} \sum_{\sigma} C_{\lambda n} C_{\sigma n} ((\mu\nu|\lambda\sigma) - (\mu\sigma|\lambda\nu)) \quad (2.36)$$

Consequently, we can calculate the matrix elements using the Fock matrix elements of the reference Fock matrix and the orbital coefficients.

$$\langle \Psi_0 | H | \Psi_a^r \rangle = \sum_{\mu\nu} C_{\mu r} C_{\nu a} F_{\mu\nu} \quad (2.37)$$

The CI matrix is then diagonalized to obtain the eigenvalues and eigenvectors. The largest coefficients for the lowest eigenvalue should indicate the more favorable d occupation.

The starting valence Fe₂ configuration for the β CI calculation was $d\pi^4 d\pi^{*4} d\delta^2 d\delta^{*2} d\sigma^1 d\sigma^{*1} 4s\sigma^2$. The β space reference configuration was $d\pi$, $d\pi$, $d\pi^*$, and $d\pi^*$, and excitations were made into the $d\delta$, $d\delta$, $d\delta^*$, $d\delta^*$, $d\sigma$, and $d\sigma^*$ orbitals. The CO was placed at 8.000 Å from the z axis in the xy plane with the Fe₂ in the z axis. The C-O distance was set at 1.140 Å, and the Fe₂ distance was set at 2.870 Å. This geometry was chosen to determine which Fe₂ configuration is

most likely in the field of the CO. The Hartree-Fock energy for this configuration and geometry is -155.557940 a.u. The results of the β CI calculation are listed in Table 2.4.

If we analyze the eigenvector of the first eigenvalue, the starting calculation has no contribution to this lowest state, because the coefficient was equal to zero. The four largest coefficients correspond to β configurations of

1. $d\pi(yz) d\pi^*(xz) d\delta(x^2-y^2) d\delta^*(x^2-y^2)$
2. $d\pi(yz) d\pi^*(yz) d\delta(xy) d\delta^*(xy)$
3. $d\pi(yz) d\pi^*(yz) d\delta(x^2-y^2) d\delta^*(xy)$
4. $d\pi(yz) d\pi^*(yz) d\delta(xy) d\delta^*(x^2-y^2)$

Since the β configuration $d\pi(yz) d\pi^*(xz) d\delta(x^2-y^2) d\delta^*(x^2-y^2)$ has the largest coefficient in the CI eigenvector, it was chosen as a starting guess for another SCF calculation. However, because each β configuration has the same symmetry, starting with any one of them should still result in the same energy due to variational collapse. The starting Fe₂ configuration is now $d\pi^3 d\pi^{*3} d\delta^3 d\delta^{*3} d\sigma^1 d\sigma^{*1} 4s\sigma^2$. This is also the same configuration produced by CONAVE. The energy with the new Fe₂ configuration at this geometry is -155.578633 a.u., which is 0.56 eV lower than found in the starting configuration. Hence, the β CI calculation has produced a better starting guess.

Table 2.4
 β CI results

10 lowest eigenvalues (a.u.)

-156.2412 -156.1026 -155.9283 -155.8911 -155.8463
 -155.8064 -155.8035 -155.7594 -155.7345 -155.7263

CI coefficients for first eigenvector

β Configuration	Coefficient
$d\pi(yz) d\pi^*(xz) d\delta(x^2-y^2) d\delta^*(x^2-y^2)$	-0.399
$d\pi(yz) d\pi^*(yz) d\delta(xy) d\delta^*(xy)$	-0.392
$d\pi(yz) d\pi^*(yz) d\delta(x^2-y^2) d\delta^*(xy)$	-0.369
$d\pi(yz) d\pi^*(yz) d\delta(xy) d\delta^*(x^2-y^2)$	-0.329

SCF calculations

<u>CO distance* (Å)</u>	<u>Energy (a.u.)</u>	<u>Number of SCF cycles</u>
8.00	-155.578633	18
6.00	-155.578859	13
4.00	-155.577907	19
3.00	-155.566935	195
2.50	-155.549592	176
2.00	unconverged	150

* CO distance is the distance from the z axis.

As the CO was brought in closer to the Fe₂ using the new starting guess, it suffered the same problems as the CONAVE calculations. The energy rose as the CO approached the Fe₂, and convergence became more difficult. This is shown in Table 2.4, where the first calculation converged in 18 cycles compared to 176 cycles when the CO is 2.50 Å above the z axis. When the CO was placed at 2.00 Å, the calculation never converged.

In conclusion the β CI has demonstrated that it can produce a better starting guess. This guess, however, may not produce a ground state or a bound state. This can be expected, because only the d orbitals were included in the CI space in our calculation. If more virtual orbitals are included in the CI space, it should yield better results.

Expanded Basis Set

Even though the GAMESS options, EXTGUESS and MINGUESS, can not be used as starting guesses for the full basis set calculations, a minimum basis set calculation or a pseudopotential calculation can be used as a starting guess for a full basis set. The eigenvectors from a smaller basis set can be expanded into a larger basis set via a projection operator proposed by Beebe and Lunell.⁵⁶⁻⁵⁹ If a pseudopotential is used, core orbitals for the full basis can easily be generated from an atomic full basis calculation.

Suppose we have two basis sets ϕ and χ

$$\phi = \{\phi_1 \dots \phi_n\}$$

$$\chi = \{\chi_1 \dots \chi_m\}$$

We can express Ψ as a linear combination of ϕ

$$\Psi = \sum_V \phi_V c_V = |\phi\rangle\langle c| \quad (2.38)$$

We want to express Ψ in terms of the new basis, χ , thereby producing Ψ' .

$$\Psi' = \sum_\mu \chi_\mu a_\mu = |\chi\rangle\langle a| \quad (2.39)$$

Ψ' is related to Ψ via a projection operator Q , such that

$$\Psi' = Q\Psi \quad (2.40)$$

and

$$Q = |\chi\rangle\langle\chi|\chi\rangle^{-1}\langle\chi| \quad (2.41)$$

where $\langle\chi|\chi\rangle^{-1}$ is the inverse overlap matrix for the χ basis.

$$\langle\chi|\chi\rangle = S_{\chi\chi} \quad (2.42)$$

Substituting equations 2.38 and 2.41 into equation 2.40 yields the expression

$$\Psi' = |\chi\rangle\langle\chi|\chi\rangle^{-1}\langle\chi|\phi\rangle\langle c| \quad (2.43)$$

Upon comparing equations 2.39 and 2.43 gives

$$\langle a| = \langle\chi|\chi\rangle^{-1}\langle\chi|\phi\rangle\langle c| \quad (2.45)$$

where $\langle\chi|\phi\rangle$ is the overlap between χ and ϕ , $S\chi\phi$.

$$\langle\chi|\phi\rangle = S\chi\phi \quad (2.44)$$

We have used this technique to converge the low symmetry $\text{Fe}_2\text{CO}(\text{C}_s)$ calculation. A starting wavefunction was generated for the full basis calculation $\text{Fe}_2\text{CO}(\text{C}_s)$ by using the eigenvectors from a converged pseudopotential calculation. It converged in 56 cycles with no oscillation in the energy. Previously, this calculation was difficult to converge, and if it did converge, convergence was slow. Yet, with the expanded wavefunction, the calculation converged rapidly and smoothly. Expanded basis method appears to be very helpful at generating a good starting guess, and one must conclude that the initial starting guess is the most important contribution to convergence. Otherwise, the other techniques would have been able to converge this system.

Incremental Cluster

The incremental cluster technique is a new convergence method developed in our laboratory. The whole premise of cluster models is that chemisorption is a local phenomenon. If this is the case, then why not maintain the local features when performing cluster calculations? In other words, we are proposing to start with small clusters to model the adsorption site then add additional atoms to these calculations to model adsorption on larger clusters. Alternatively, the major adsorbate-surface interactions take place with the neighboring surface atoms, so why not start with the neighbor surface atoms and measure how the surface interactions are modified when the cluster size is increased.

For instance, in the on top CO adsorption on Fe(100), the linear FeCO(C_{4v}) unit is always present in any cluster calculation. To model the same adsorption site on a larger cluster, the next simplest cluster to use would be Fe₃CO(C_{2v}) with the additional 2 Fe atoms at the same geometry as the Fe(100) surface. In the incremental cluster technique, orbitals from an Fe₂ calculation would be orthonormalized to the orbitals of the linear FeCO(C_{4v}) calculation. This is illustrated in figure 2.3. As a consequence the FeCO(C_{4v}) vectors would be augmented by the vectors of the Fe₂ calculation.

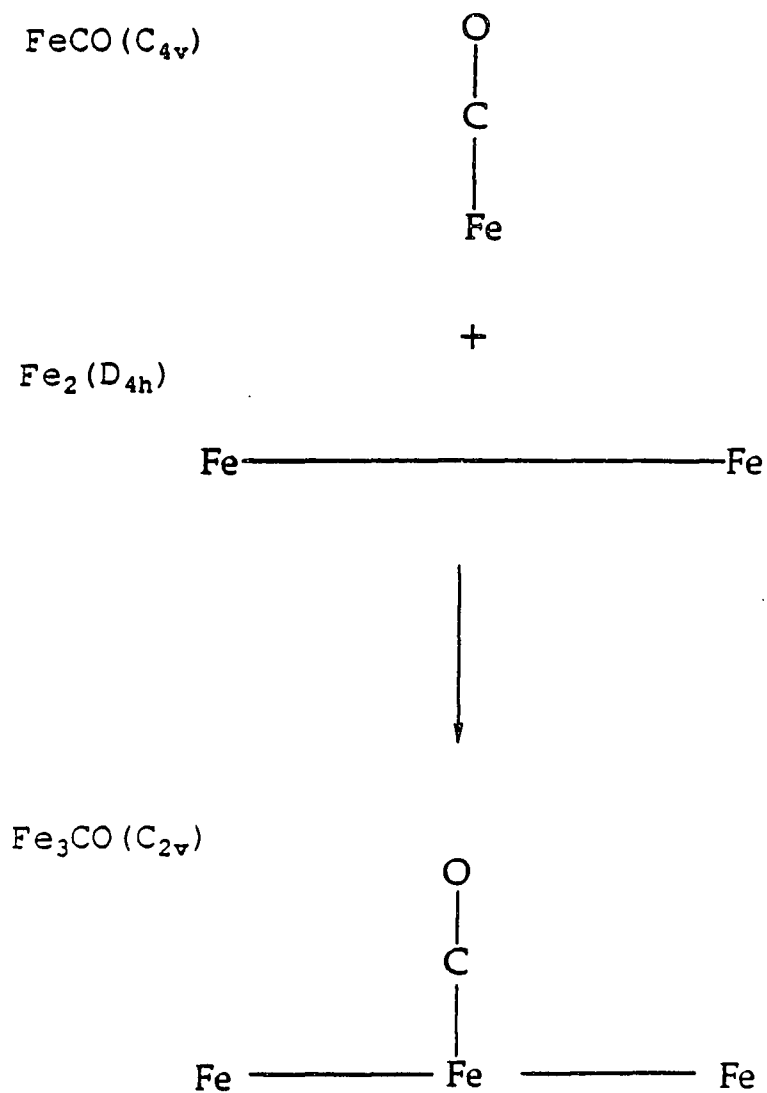
Incremental Cluster Technique for $\text{Fe}_3\text{CO}(\text{C}_{2v})$ 

Figure 2.3

The incremental cluster technique was the only method we used that could converge $\text{Fe}_4\text{CO}(\text{C}_5)$ calculations. Any attempt at charge build-up for the $\text{Fe}_4\text{CO}(\text{C}_5)$ calculation was futile, because the calculations would always diverge. Therefore, because the orbitals and geometry of the $\text{Fe}_2\text{CO}(\text{C}_5)$ case were converged, we proposed using them to start the $\text{Fe}_4\text{CO}(\text{C}_5)$ calculations. Consequently, the incremental cluster technique has greatly reduced convergence problems in the larger clusters.

In addition to problems with the convergence, we believe the incremental cluster technique can solve problems with the adsorbate properties of larger clusters. As stated in the introduction, a serious concern with cluster calculations is the dependence of adsorption properties on cluster size.⁶⁰⁻⁶⁹ Properties such as adsorbate vibrational frequencies and geometries converge fairly rapidly with cluster size.⁶⁶⁻⁶⁹ Yet, the binding energies of adsorbates have been shown to fluctuate with cluster size. Hermann et al. performed CO on C_{4v} Cu_n cluster calculations, where $n = 1, 5, 10, 14,$ and 34 .⁶⁰ When $n = 1, 10,$ and $34,$ the adsorption was nonbinding. When $n = 5$ and $14,$ the adsorption was binding. This was explained by the fact that $n = 1, 10,$ and 34 had an orbital of A_1 symmetry higher in energy than the orbital of E symmetry. The A_1 orbital acted in repelling the CO, and the $n = 5$ and 14 cases had orbitals of E symmetry higher in energy than the A_1 orbital. The orbitals of E symmetry are crucial

in the π backdonation. Therefore, the electronic state of the cluster around the adsorption site is crucial to binding.

Panas et al. showed for the chemisorption of H and O on Ni(100) that convergence of the binding energy can be achieved by using a proper electronic state for the naked cluster at the adsorption site.⁶¹ If we consider H, they propose that the cluster state should have a singly occupied orbital of a_1 symmetry available to bond with the a_1 singly occupied orbital of H. This state should be used at short and long bond distances between H and the cluster. If the ground state of the naked cluster does not meet these requirements, then the cluster must be excited to a more conducive state for binding. They found convergence for the chemisorption energies with increasing cluster size using their procedure.

A similar study done by the same people discovered the identical behavior for H_2 dissociation.⁷⁰⁻⁷² H_2 dissociates on Ni, Co, and Fe with very small energy barriers.⁷³ When the ground state of the naked Ni cluster is used to model the H_2 dissociation, the energy barriers calculated are much higher than experimental values. However, once the properly excited state of the naked Ni cluster is used, the energy barrier calculated reproduces experiment very well.⁷⁰⁻⁷²

Incremental cluster provides a good electronic state for larger clusters with the adsorbate, because the same basic interactions are taking place regardless of the size of the

cluster. Exciting the cluster to achieve the proper binding state is not necessary with the incremental cluster method.

Techniques to Achieve SCF Convergence

In this section we discuss convergence techniques that are utilized during the SCF procedure. There are essentially two kinds of convergence techniques. The first is the techniques that expedite the calculation to the ground state. The second is the techniques that maintain the state loyalty of the calculation. Extrapolation and DIIS are techniques used to find the ground state. Damping, level shifting, restrict, and symmetry blocking are techniques which maintain the state loyalty. Two other techniques, hacker and altering the geometry, are designed to accelerate convergence in the current state but do not assure state loyalty.

To compare the quality of the extrapolation versus DIIS, calculations, similar to those discussed in the initial guess section, were performed on $\text{FeCO}(\text{C}_{4v})$. As demonstrated earlier the charged calculation of +2 produces a good starting guess to the ground state, while H_{core} , the charge of -4, and the the charge of +8 were poor starting guesses. The quality of these SCF convergence techniques will be determined by their ability to find the ground state from each of these starting guesses. How quickly they find the ground state will measure the quality of the technique.

If indeed the state loyalty techniques maintain state loyalty, they should also produce the same ground state as obtained in the +2 calculation. In contrast, the other starting guesses should produce excited states. The final energies and the behavior of the calculation will be used to judge the quality of the state loyalty techniques. Oscillating behavior of the energy during the SCF cycles indicates a poor state loyalty technique. Restrict and symmetry blocking are studied separately, because they are used under different conditions than damping and level shifting, which is explained later.

Extrapolation

Extrapolation is simply what the name implies: three points are used to extrapolate to a new point.^{52,74-81} The point in the SCF procedure, M , can be the coefficient matrix, C , the density matrix, P , or the Fock matrix, F .⁵² One formula for producing the new point goes accordingly,

$$M^{\text{new}} = M^{k+1} + \Delta M^{k+1} / (\Delta M^k - \Delta M^{k+1}) \quad (2.46)$$

where M^{new} is the projected point and k is the iteration number. The change in M between iterations is defined by

$$\Delta M^k = M^k - M^{k-1} \quad (2.47)$$

Equation 2.47 is derived from Aitken extrapolation method for iterative processes,⁷⁴ where a new M^{k+1} is a function of a previous M^k

$$M^{k+1} = f(M^k) \quad (2.48)$$

and convergence, w , is reached when

$$w = \lim M^k \text{ as } k \rightarrow \infty \quad (2.49)$$

In the GAMESS program the Fock matrix is used for M in the extrapolation routine.

In Table 2.5 the results for convergence of FeCO(C_{4v}) using extrapolation are given. In two calculations extrapolation did aid the convergence to the target energy. Also, the H_{core} calculation did have an energy close to the target energy. Extrapolation did show fairly good results. Yet, extrapolation is known to expedite the end of a calculation, rather than a technique to accommodate the whole process.⁵²

DIIS

A more recent technique is the Direct Inversion in the Iterative Subspace or DIIS technique introduced by Pulay.^{82,83} DIIS is derived from the Lanczos method for an

eigenvalue problem.⁸⁴ In each SCF cycle, an error matrix, e_i , is calculated. For a series of Fock matrices, F_i , and errors, e_i , the iterative subspace can be directly inverted to obtain a new F_i with zero error. This is done by solving the following set of equations

$$\begin{pmatrix} 0 & -1 & -1 \\ -1 & B_{11} & B_{12} \\ -1 & B_{21} & . \\ -1 & . & B_{ij} \\ . & . & . \end{pmatrix} \begin{pmatrix} -\lambda \\ C_1 \\ C_2 \\ C_i \\ . \end{pmatrix} = \begin{pmatrix} -1 \\ 0 \\ 0 \\ 0 \\ . \end{pmatrix} \quad (2.50)$$

where B_{ij} is the trace of e_i times e_j^+ .

$$B_{ij} = \text{tr}(\underline{e}_i \underline{e}_j^+) \quad (2.51)$$

Each error matrix is defined by

$$\underline{e}_i = (\underline{S}^{-1/2})^+ (\underline{F}_i \underline{P}_i - \underline{P}_i \underline{F}_i) (\underline{S}^{-1/2}) \quad (2.52)$$

λ is a Lagrangian multiplier which causes the sum of C_i to be equal to one. Then the new Fock matrix is a linear combination of previous Fock matrices.

$$\underline{F} = \sum_i C_i \underline{F}_i \quad (2.53)$$

The results for convergence on the $\text{FeCO}(\text{C}_{4v})$ system are listed in Table 2.5. Using DIIS, only one calculation converged to the ground state. The other calculations were diverging from the ground state. This is slightly worse than extrapolation, but DIIS converged to the ground state in only 16 cycles. It is the only calculation in the entire study to converge to the ground state in under 50 cycles. DIIS is an excellent technique to use, but it is very sensitive to the initial guess. Also, DIIS did not solve any problems we encountered with the $\text{Fe}_2\text{CO}(\text{C}_s)$ geometry.

Recently, Sellers has reported " In our experience with metal cluster systems we have encountered many cases of which heavily damped Roothan Hall iterations, level shifting, DIIS, and variable matrix second order convergence schemes do not bring convergence at all or the rate is intolerably low."⁸⁵ Sellers' comments describe precisely the SCF convergence characteristics we have found with our Fe clusters. He suggests that adding a change in dipole moment to B_{ij} can improve the DIIS technique, where B_{ij} is now

$$B_{ij} = \text{tr}(\underline{e}_i \underline{e}_j^+) + s \langle \Delta \underline{\mu}_i | \Delta \underline{\mu}_j \rangle \quad (2.54)$$

where s is a scalar and $\Delta \underline{\mu}_i$ is the change in dipole moment between iterations such that

$$\Delta \underline{\mu}_i = \underline{\mu}_i - \underline{\mu}_{i-1} \quad (2.55)$$

Table 2.5
Convergence Acceleration Techniques

Target Energy = -1374.969870 a.u.

Extrapolation

<u>Initial guess</u>	<u>Behavior</u>	<u>Final Energy</u> <u>(a.u.)</u>	<u>Number of SCF</u> <u>cycles</u>
H _{core}	oscillating	-1374.890814	50
+2	converging	-1374.969555	50
-4	oscillating	-1278.159474	50
+8	converging	-1374.969861	50

DIIS

<u>Initial guess</u>	<u>Behavior</u>	<u>Final Energy</u> <u>(a.u.)</u>	<u>Number of SCF</u> <u>cycles</u>
H _{core}	oscillating	-1236.665522	50
+2	converged	-1374.969870	16
-4	oscillating	-1236.665522	50
+8	oscillating	-1240.201226	50

He states fluctuations in the dipole moment can occur without orbital switching causing slight energy changes and slow convergence.⁸⁵ We investigated the Sellers' algorithm by implementing it into the GAMESS program with $s = 1$. This addition did not prove to aid convergence in our Fe clusters. In fact, the change in dipole was very small between iterations corresponding to only small changes in the error matrix.

Damping

Damping is a simple procedure where usually the new density is produced from the current density and the previous density by a weighting factor.^{52,81,86-91} If the weighting factor is large enough, then state loyalty is maintained. However, a large weighting factor can slow convergence considerably. Damping is described by the following formula

$$M^{\text{new}} = (1-\alpha)M^k + \alpha M^{k-1} \quad (2.56)$$

Likewise as in extrapolation, M can be C, P, or F.⁵² α is the weighting factor with values between 0 and 1. A large weighting factor would be on the order of 0.6.

The damping factor can be held fixed, but there are dynamic damping procedures to change the value of α during the iterative cycle.⁸⁸⁻⁹⁰ In the GAMESS program the dynamic

damping technique was introduced by Hsu et al., and it is slightly different than regular damping, because it is derived from the Aitken extrapolation technique.⁹¹ In this damping

$$P_{\text{new}} = (P^k + \lambda P^{k-1}) / (1 + \lambda) \quad (2.57)$$

where P is the density matrix and λ is greater than or equal to zero.

The results for damping on converging the $\text{FeCO}(\text{C}_{4v})$ calculations are listed in Table 2.6. The calculation with the charge of +2 as the starting guess is converging towards the ground state as it should. Yet, the other calculations are oscillating and their final energies are quite high. This demonstrates that damping can be a poor choice for maintaining state loyalty.

Level Shifting

Level shifting was introduced by Saunders and Hillier.⁹² Changes in the molecular orbital coefficients and energy between SCF cycles are affected only by the occupied and virtual orbital mixing. Therefore, based on first order perturbation theory the new molecular orbital coefficients can be written as a sum of the old coefficients plus a contribution from the virtual orbitals such that

$$C_{vi}^{k+1} = C_{vi}^k + \sum_a \Delta_{ia}^{k+1} C_{va}^k \quad (2.58)$$

Δ_{ia} is the contribution of the virtual orbital, a , mixing with the occupied orbital, i . Δ_{ia}^{k+1} is given by

$$\Delta_{ia}^{k+1} = F_{ia} / (e_i - e_a) \quad (2.59)$$

where F_{ia} is the Fock matrix element between orbitals i and a , and e_i , e_a are their respective orbital energies.⁵²

In level shifting a scalar, b , is added to the diagonal elements of the virtual orbitals.^{52,81,92-95} thereby reducing the contribution from each virtual orbital

$$\Delta_{ia}^{k+1} = F_{ia} / (e_i - e_a - b) \quad (2.60)$$

and prevents orbital switching.

In addition to preventing orbital switching, the total energy must necessarily decrease. The new total energy can be expressed as a first order perturbation correction, where

$$E = E_0 + \sum_i \sum_a \Delta_{ia} F_{ia} \quad (2.61)$$

where E_0 is the zero order energy and E is the new total energy. Equation 2.60 for Δ_{ia} ensures that the second term in equation 2.61 will be negative. Therefore, there must be a decrease in energy. However, if b is made too large then the

orbital mixing is reduced considerably, and the convergence rate becomes too slow. Therefore, smaller values of b need to be used later in the SCF cycle. Dynamic level shifting techniques have also been developed.^{94,95}

Table 2.6 demonstrates very well how level shifting maintains state loyalty and converges the calculation. All four calculations are converging at the end of 50 cycles. The calculation with the charge of +2 as the starting guess converged to the ground state. The other calculations are converging towards different excited states demonstrating state loyalty is maintained. Level shifting is a superior technique than damping in obtaining converged states.

Although level shifting worked very well for the FeCO(C_{4v}) calculations, it still failed to produce convergence for the Fe₂CO(C_s) geometry. This is due in part to the fact that the level shifting in the GAMESS program is dynamic. Consequently, the value of b may become too small allowing orbitals to switch. To avoid this problem the value of b was held fixed at 0.15 a.u., which is very low for level shifting, but the calculation still did not converge in 1500 cycles.

Restrict

Restrict is a technique written in the GAMESS program to restrict the occupied orbital ordering.⁵¹ To prevent orbital

Table 2.6
 State Loyalty Techniques
 Damping and Level Shifting

Target Energy = -1374.969870 a.u.

Damping

<u>Initial guess</u>	<u>Behavior</u>	<u>Final energy</u> <u>(a.u.)</u>	<u>Number of SCF</u> <u>cycles</u>
H _{core}	oscillating	-1371.537703	50
+2	converging	-1374.969856	50
-4	oscillating	-1350.144248	50
+8	oscillating	-1361.438707	50

Level shifting

<u>Initial guess</u>	<u>Behavior</u>	<u>Final energy</u> <u>(a.u.)</u>	<u>Number of SCF</u> <u>cycles</u>
H _{core}	converging	-1374.755955	50
+2	converged	-1374.969870	50
-4	converging	-1374.251014	50
+8	converged	-1374.791461	50

switching the overlap between the eigenvectors, C_k , from the current iteration and the eigenvectors, C_{k-1} , from the previous iteration is analyzed, where

$$\underline{C}_k^+ \underline{S} \underline{C}_{k-1} = \underline{\Delta} \quad (2.62)$$

The resultant matrix, Δ , should be close to the unit matrix if there has been no orbital switching. If an off-diagonal element, Δ_{ij} , is close to 1, then orbitals i and j have switched. The routine would then rearrange the orbitals into the previous order. The FeCO(C_{4v}) results for using restrict are listed in Table 2.7. It is the only technique that did not produce the ground state with the +2 charged starting vectors. One calculation is converging, and it is near the same energy as produced by level shifting. The results of restrict are due to the fact that in the early cycles C_k and C_{k-1} differ greatly. Therefore, C^+SC is not close to the unit matrix, which causes the restrict routine to breakdown.

Restrict should only be used near convergence or during geometry optimizations once convergence of an SCF calculation has been achieved. This is why H_{core} was not included as a starting guess, because restrict should be used to control a known desired state.

Symmetry Blocking

Since the eigenvectors of the Fock matrix translate according to different irreducible representations of the point group, we can then block diagonalize the Fock matrix into separate irreducible representations.^{96,97} In doing so one can constrain the number of occupied orbitals of a particular symmetry. This aids in maintaining numerical accuracy and prevents any changes in the electronic state. Symmetry has also been used in the calculation of integrals and gradients.⁹⁸⁻¹⁰⁰

In the GAMESS program the Fock matrix is converted into the molecular orbital basis by equation 2.17. To block diagonalize the Fock matrix we partition the eigenvectors into each irreducible representation, i . Then we convert the Fock matrix using each partition such that

$$\underline{F}_i' = \underline{C}_i^+ \underline{F} \underline{C}_i \quad (2.63)$$

For the high symmetry cases, we have found symmetry blocking to be very useful. The results for the FeCO(C_{4v}) geometry are listed in Table 2.7. The starting guess of the +2 charged calculation produced the target energy as it should. The starting guesses of the charges -4 and +8 are oscillating, because these starting guesses have broken the degeneracy of the π orbitals, which is why they were poor

Table 2.7
 State Loyalty Techniques
 Restrict and Symmetry Blocking

Target energy = -1374.969870 a.u.

Restrict

<u>Initial guess</u>	<u>Behavior</u>	Final energy (a.u.)	Number of SCF cycles
H _{core}	oscillating	-1173.018535	50
+2	oscillating	-1365.896322	50
-4	oscillating	-1365.604688	50
+8	converging	-1374.791375	50

Symmetry blocking

<u>Initial guess</u>	<u>Behavior</u>	Final energy (a.u.)	Number of SCF cycles
+2	converging	-1374.969425	50
-4	oscillating	-1144.613422	50
+8	oscillating	-1258.987577	50

starting guesses in the previous calculations. H_{core} was also not included due to the same reasons for restrict. Symmetry blocking is a technique that is better for maintaining a desired known electronic state. In fact, for the ROHF calculation on the FeCO(C_{4v}) geometry, it proved to be the only technique that could achieve convergence. However, for the low symmetry Fe₂CO(C_s) geometry, symmetry blocking did not help the convergence. Another advantage of symmetry blocking is that it allows one to study excited states by preventing variational collapse to the ground state. Restrict can also perform this function, but it is less reliable. Yet, restrict requires less computational time, which is another factor to consider.

Hacker

Computer round off error can be a problem in quantum chemistry calculations because of the large number of floating point operations. Since the low symmetry clusters have very few Fock matrix elements equal to zero, we suspected the Fock matrix of the Fe₂CO(C_s) geometry was causing numerical instability problems in the diagonalization routines. In turn, this caused slow convergence due to inaccurate calculations of the eigenvectors. Therefore, we investigated two schemes to overcome this problem. These are hacker and perturbation hacker.

In hacker, we set a threshold on the Fock matrix elements, where the absolute maximum of the Fock matrix elements is divided by a scalar.

$$\text{Threshold} = \text{Max}(F_{ij})/\text{Scalar} \quad (2.64)$$

If a Fock matrix element falls below the threshold then it is set equal to zero.

$$\begin{aligned} \text{If } F_{ij} < \text{Threshold} & \quad (2.65) \\ \text{then set } F_{ij} = 0 & \end{aligned}$$

In doing so a number of the Fock matrix elements are zeroed out or hacked out. A number of different scalars were examined to determine which are best. As the larger Fock elements converged, the $\text{Max}(F_{ij})$ decreases producing a reduced threshold.

The perturbation hacker involved not only including the larger Fock matrix elements but also the elements whose diagonal elements were close in energy. First, we define a measure, M_{ij} , where each off diagonal element is divided by the corresponding difference of diagonal elements. Then the

$$M_{ij} = |F_{ij}|^2 / (F_{ii} - F_{jj}) \quad (2.66)$$

threshold is set by dividing the absolute maximum of the measure by a scalar.

$$\text{Threshold} = \text{Max}(M_{ij}) / \text{Scalar} \quad (2.67)$$

If the corresponding measure of an off diagonal element is below this threshold then the element is set equal to zero.

$$\begin{aligned} \text{If } M_{ij} < \text{Threshold} & \quad (2.68) \\ \text{then set } F_{ij} &= 0 \end{aligned}$$

A number of different scalars were investigated for this scheme, too.

A model calculation on $\text{Al}_2\text{CO}(\text{C}_5)$ was performed. The Al-Al distance was set at 2.00 Å, and the C-O distance was set at 1.137 Å. The CO was placed 2.00 Å from the z axis. Different scalars were used to determine which ones are optimum. The cluster is depicted in figure 2.4. First, a charge calculation was done on the Al_2CO to determine if the hacker idea can be used under all conditions. The charge placed on the cluster was +2 and a multiplicity of 1. The starting guess for this calculation was H_{core} . A regular SCF calculation was performed with DIIS, and it converged in 38 cycles to an energy of -595.568544 a.u. The results are listed in Table 2.8.

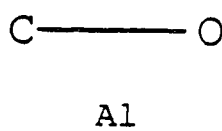
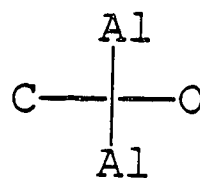
$\text{Al}_2\text{CO}(\text{C}_s)$ Cluster for Hacker Studies

Figure 2.4

Table 2.8

Hacker and Perturbation Hacker Results

Al₂CO(C_s) Geometry:

Al-Al distance = 2.000 Å

C-O distance = 1.137 Å

CO distance from z axis = 2.000 Å

Charge = +2

Multiplicity = 1

<u>Method</u>	<u>Energy (a.u.)</u>	<u>Scalar</u>	<u>SCE Cycles</u>
<u>DIIS</u>	-595.568544		38
<u>Hacker</u>	-595.568544	10	30
	-595.568544	10 ²	39
	-595.568544	10 ³	38
	-595.568544	10 ⁴	38
	-595.568544	10 ⁷	38
<u>Perturbation</u>	-582.280299	10	23
	-488.311016	10 ²	unconverged
	-595.568544	10 ³	43
	-595.568544	10 ⁴	39
	-595.568544	10 ⁷	38

The hacker calculations converged to the same energy in approximately the same number of cycles; except when the scalar was set equal to 10, the calculation converged in 30 cycles. The perturbation hacker calculation was divergent when the scalar was set at 10, and it produced a higher energy when the scalar was set at 100. Higher values for the scalar produced the correct energy but in slightly more cycles.

The vectors from the charged calculation were then used to perform a calculation with a charge of 0 and a multiplicity of 1. The results are listed in Table 2.9. The regular SCF calculation converged in 16 cycles at an energy of -596.245910 a.u. The hacker calculations again produced the same energy in approximately the same number of cycles. Except, it took 25 cycles to converge the calculation when the scalar was set at 10. The perturbation hacker produced the correct energy in approximately the same number of cycles when the scalar was set high. When the scalar was set at 10 or 100, the calculations are converging but in many more cycles.

Because the hacker proved to be the most promising, we decided to use it on the $\text{Fe}_2\text{CO}(\text{C}_5)$ cluster. With the full basis set the CO was set at 6.069 Å from the z axis, and the C-O distance was set at 1.137 Å. For the pseudopotential $\text{Fe}_2\text{CO}(\text{C}_5)$ calculation, the CO was set at 2.069 Å from the z axis with a C-O distance of 1.137 Å. For the full basis set

Table 2.9

Hacker and Perturbation Hacker Results

Al₂CO(C_s) Geometry:

Al-Al distance = 2.000 Å

C-O distance = 1.137 Å

CO distance from z axis = 2.000 Å

Charge = 0

Multiplicity = 1

<u>Method</u>	<u>Energy (a.u.)</u>	<u>Scalar</u>	<u>SCF Cycles</u>
<u>DIIS</u>	-596.245910		16
<u>Hacker</u>	-596.245910	10	25
	-596.245910	10 ²	17
	-596.245910	10 ³	16
	-596.245910	10 ⁴	16
	-596.245910	10 ⁷	16
<u>Perturbation</u>	-596.245871	10	unconverged
	-596.245910	10 ²	50
	-596.245910	10 ³	16
	-596.245910	10 ⁴	23
	-596.245910	10 ⁷	16

calculation the scalar was set at 100, and the calculation did not converge in 240 cycles. Likewise, for the pseudopotential calculation, it did not converge in 150 cycles.

The hacker idea does seem to aid convergence, but it did not solve any problems associated with the $\text{Fe}_2\text{CO}(\text{C}_s)$ calculations. For Hacker the smaller scalars, i.e. 100 or 1000, appeared to converge the calculations the most quickly. For the perturbation hacker the opposite is true. A larger scalar, i.e. 1000-10000, gives better results for convergence.

Geometry Optimization

Oddly enough, what proved to be the most valuable technique for achieving convergence was altering the geometry. This was observed while performing calculations on the $\text{Fe}_4\text{CO}(\text{C}_{4v})$ cluster depicted in figure 2.5, where the C-O bond length was set at 1.140 Å. When the CO was brought closer to the Fe_4 , the energy rose and convergence became more difficult. The CO was brought to a position of 1.0 Å above the plane of the Fe_4 cluster. A partial geometry optimization¹⁰¹ was performed on the cluster, where only the O was allowed to vary its position. Table 2.10 lists the number of SCF cycles needed to achieve convergence at different geometries.

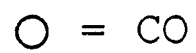
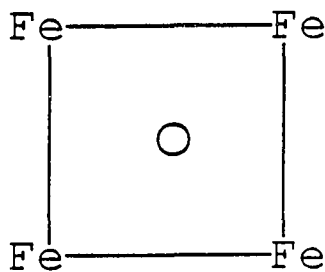
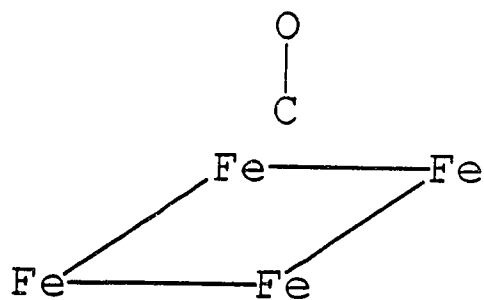
$\text{Fe}_4\text{CO}(\text{C}_{4v})$ Geometry

Figure 2.5

Table 2.10

Convergence versus Geometry Optimization

Fe₄CO (C_{4v}) Geometry:

Fe-Fe distance = 2.870 Å

C-O distance = 1.140 Å

CO distance* (Å)	Energy (a.u.)	Cycles
5.0	-198.335228	18
4.0	-198.334874	12
2.5	-198.321999	60
2.0	-198.306291	77
1.0	-198.239629	81

* CO distance is the distance C is from the plane of the Fe₄ cluster.

Partial Geometry Optimization

CO is at 1.00 Å from plane of the Fe₄ cluster

C-O distance (Å)	Energy (a.u.)	Cycles
1.205	-198.247579	25
1.214	-198.247749	34
1.217	-198.247761	13
1.217	-198.247761	3

The CO bond length increased and the subsequent calculations converged much more rapidly. These calculations are converging in less than 50 cycles compared to 81 cycles when the C-O bond length is 1.140 Å. Consequently, the convergence was difficult due to the CO bond length of 1.140 Å, which is near the free CO bond length. This is also the reason why the $\text{Fe}_2\text{CO}(\text{C}_s)$ calculations would not converge, for the CO bond length was placed at 1.14 Å. As the CO approached the Fe_2 , the interaction simply became more repulsive. Relaxing the CO bond length allows the Fe_2 cluster and the CO to mix orbitals rather than repel. In fact, as will be discussed later in chapter 5, in order to achieve convergence on the $\text{Fe}_2\text{CO}(\text{C}_s)$ cluster, the geometry had to be altered. Additionally, removing the CO from the Fe clusters and reattaching the CO has produced lower energy states. Schlegel and McDouall also suggest altering the geometry to obtain convergence.⁵² We believe this is due to a greater separation in energy between the states resulting from the change in geometry. The greater separation in energy reduces the tendency of the calculations to oscillate between states.

Conclusion

In conclusion we would like to propose a procedure for performing calculations on Fe clusters and on transition metal clusters in general. First, one should start with a

minimal basis set or a pseudopotential basis set on small clusters of high symmetry. Small basis sets have proven to provide a qualitative description of the ground state wavefunction. Also one will not be hampered by needing large amounts of computer time. Clusters of high symmetry are known to be less prone to convergence problems.⁵²

From the studies conducted and based on our own observations, clearly the most crucial element concerning convergence is the starting guess. The convergence techniques will produce the final energy quickly once the starting guess is adequate, but they are by no means an automatic procedure to achieve convergence. To obtain a correct starting guess, the charge build-up procedure is recommended for clusters of high symmetry, but many different charge build-up schemes must be investigated in order to ensure that the true ground state has been found. Any subsequent problems in convergence from these charged guesses undoubtedly means one is starting with a poor guess. If different charge schemes are still plagued by convergence problems, then altering the geometry should be attempted next. Altering the geometry has proven to be the most advantageous technique in finding bound states for CO on the Fe clusters.

Once a good starting guess has been produced, accelerating the convergence can be accomplished via DIIS or level shifting. These techniques are highly recommended. Extrapolation and damping are techniques, which can also be

helpful, but they do not have the efficiencies of DIIS and level shifting. Symmetry blocking or restrict is recommended for systems with high symmetry and a known desired electronic state in order to prevent any switching of states during the SCF cycles.

After the smaller basis set calculations have been completed, one can obtain better energies and geometries by expanding the basis functions using the Beebe technique. Because the expansion of the smaller basis set has proven to provide a reliable guess for the larger basis set, problems encountered using the smaller basis sets will not be as prevalent with the larger basis sets. To conduct studies on larger clusters, we recommend constructing the clusters using the incremental cluster method. Recent calculations on Be clusters have verified that incrementing the cluster can provide excellent binding energies and alleviate many of the problems with convergence. The complete procedure is summarized in figure 2.6.

SCF Procedure for Transition Metal Clusters

1. Start with a small basis set or pseudopotential basis set
2. Start with a small cluster of high symmetry
3. Use charge build-up to produce starting guesses
4. Alter the geometry for difficult cases
5. Use DIIS and level shifting to aid convergence
6. Use symmetry blocking for high symmetry cases
7. Expand smaller basis sets into larger basis sets using the Beebe Technique
8. Construct larger clusters using the incremental cluster technique.

Figure 2.6

Chapter 3

Constrained Space Orbital Variation

Constrained Space Orbital Variation (CSOV) provides a formulism, wherein a wavefunction is separated into a fixed part and a variational part. In doing so one hopes to study the partial variation of a wavefunction within the field of the remaining fixed wavefunction. This idea has a long history,¹⁰²⁻¹⁰⁷ and one of its first uses was by Lykos and Parr, where they justified the separability of σ and π orbitals because of their orthogonality.¹⁰² Bagus et al. coined the name CSOV and developed the method for analysis of the energetics of chemical bond interactions.^{106,107}

CSOV Method

To separate the fixed and variational parts in the CSOV method, the Fock matrix, F , is converted via a unitary transformation to

$$\underline{\underline{F'}} = \underline{\underline{T}}_{nm}^{\dagger} \underline{\underline{F}} \underline{\underline{T}}_{nm} \quad (3.1)$$

where n is the size of the complete space, and m is the size of the variational space. T is a unitary matrix in the complete space with the T_{nm} block being constructed from m variational orbitals. The resulting variational Fock matrix,

F' is m dimensional. The orbital interactions are dissected into steps to measure their contribution to the final energy. This is done by computing the decrease in energy as the variational space is modified between different steps. Although the CSOV method can also be used to keep a part of the wavefunction fixed such as the periphery of a cluster in order to study a local interaction while simulating the surroundings. Currently, the common method to examine orbital interactions is to use the Mulliken population analysis,¹⁰⁸ but this method has a number of shortcomings such as yielding different results for different basis sets.

To start a CSOV analysis the system to be studied first needs to be separated into two subunits, A and B. For instance in FeCO, Fe and CO are suitable subunits, since the CO enters the space of the Fe and forms a bond. In order for one to proceed with the CSOV study, an initial electronic configurations for each subunit must be determined. This is done by pulling the two subunits apart into free subunits and allowing the subunits to relax into their separated subunit electronic configurations. It is important that the geometry of the individual subunits match the geometry they possess in the final system. In other words, if CO is subunit B, then the CO bond length used in the combined system is the CO bond length used to calculate the subunit CO energy and configuration. Likewise, the d occupation for Fe should be the symmetrically equivalent d occupation in the final system

and need not necessarily be the same as the Fe atom ground state d occupation.

The reference energy is the sum of the energy of the separate subunits using the above electronic configurations. The energy, E_{step} , in the CSOV analysis is the difference between the reference energy and the partial SCF energy or the energy of a particular CSOV step.

$$E_{\text{step}} = E(A) + E(B) - E(\text{partial SCF}) \quad (3.2)$$

Before starting the CSOV study the orbitals from the subunits must be superimposed and orthogonalized at the desired geometry. The energy calculated at this point is the frozen orbital energy. The frozen orbital step determines if the initial interaction between the subunits is attractive or repulsive. If the energy is positive the interaction is attractive, and if the energy is negative, the interaction is repulsive. The orbitals of the subunits must be orthogonalized to retain the overall orthonormality of the complete wavefunction. Also, the orbitals have to be ordered in a particular fashion in order to accommodate the CSOV analysis. This is usually done like so:

$$A_{\text{occ}} B_{\text{occ}} B_{\text{virt}} A_{\text{virt}} \quad (3.3)$$

The *occ* and *virt* label respectively the occupied and virtual orbitals of fragments A and B. Different orthogonalization techniques and further details on how to choose A and B are discussed later in this chapter.

After the frozen orbital step, the first step in the CSOV technique might allow B to relax in the field of A. Large changes in energy indicate that B is perturbed greatly by A. The relaxation step is not restricted to relaxing every orbital of B in the step. For instance, one could relax only the σ orbitals of B, and then the π orbitals could be relaxed in a separate step. The energy changes for the different steps allows one to determine which orbitals are energetically more important to A.

The second step might allow B to mix with the virtual orbitals of A. This measures the importance of any donation into A from B. The π backdonation from a transition metal into the CO π^* orbitals is a typical example of this type of interaction. Likewise, the virtual orbitals of A may be partitioned to investigate different orbital interactions. One big advantage of the CSOV technique is its versatility for examining different interactions.

After B has been allowed to mix with all the virtual orbitals of A, the orbitals must now be rearranged to let A vary in the field of B, and equation 3.3 becomes

$$B_{occ} A_{occ} A_{virt} B_{virt} \quad (3.4)$$

Because the B subunit and the A virtual orbitals were allowed to mix, one needs to differentiate the A orbitals from the B orbitals before proceeding with step 3. This is achieved by measuring the overlap between the frozen orbitals, C_{FO} , and the current orbitals from step 2,

$$\underline{C}_{FO}^+ \underline{S} \underline{C}_{step2} = \underline{X} \quad (3.5)$$

where S is the overlap matrix. The large matrix elements in X determine which orbitals in C_{step2} correlate with the A frozen virtual orbitals.

Now step 3 can be calculated by letting the orbitals of A vary in the field of B. This measures the perturbation of B on A. Step 4 is analogous to step 2, but now the orbitals of A are allowed to mix with the virtual orbitals of B. Finally, step 5 consists of varying all the orbitals to arrive at the final SCF energy.

In essence there are 6 general steps to the CSOV analysis, and they are summarized in figure 3.1. It is important to note that these steps are flexible to modifications and further partitioning.

Orthogonalization

In order for the SCF procedure to be valid, the eigenvectors must be orthonormal as described by equation

General CSOV Steps

- 0 = Frozen orbital energy : FO
- 1 = Vary B in the field of A : V(B:B)
- 2 = Mix B with the virtual of A : V(B:A virtual)
- 3 = Vary A in the field of B : V(A:A)
- 4 = Mix A with the virtual of B : V(A:B virtual)
- 5 = Final SCF energy : V(SCF)

Figure 3.1

2.10. Note that when combining A and B the orbitals are not automatically orthonormal. Therefore, the combined orbitals of A and B must be orthonormalized. There are essentially two orthogonalization techniques used in the CSOV procedure: Schmidt and symmetric.⁵⁰

Schmidt orthogonalization consists of orthonormalizing each vector to a previous set of vectors. Initially, we have a set of vectors, where

$$\langle c_i | S | c_j \rangle \neq \delta_{ij} \quad (3.6)$$

To orthogonalize $|c_i\rangle$ we want

$$\langle c_i | S | c_j \rangle = 0 \quad (3.7)$$

for $j \neq i$. This can be accomplished by

$$|c_i'\rangle = |c_i\rangle - |c_j\rangle \langle c_j | S | c_i \rangle \quad (3.8)$$

If we sum over all previous vectors, j to i , then $|c_i'\rangle$ is now expressed as

$$|c_i'\rangle = \{ |c_i\rangle - \sum_{j^i} |c_j\rangle \langle c_j | S | c_i \rangle \} / \langle c_i' | S | c_i' \rangle^{1/2} \quad (3.9)$$

where $\langle c_i' | S | c_i' \rangle^{1/2}$ is a normalization constant.

The symmetric method orthogonalizes the orbitals simultaneously rather than in series. We express the overlap between the vectors as \underline{X}

$$\underline{C}^+ \underline{S} \underline{C} = \underline{X} \quad (3.10)$$

If we multiply by $\underline{X}^{-1/2}$ on both sides of \underline{X} , then \underline{X} is transformed into a unit matrix.

$$\underline{X}^{-1/2} \underline{X} \underline{X}^{-1/2} = \underline{1} \quad (3.11)$$

To determine $\underline{X}^{-1/2}$, we diagonalize \underline{X} to obtain the eigenvectors, \underline{U} , and eigenvalues, \underline{x} , of \underline{X} . Then $\underline{X}^{-1/2}$ is given by

$$\underline{X}^{-1/2} = \underline{U} \underline{x}^{-1/2} \underline{U}^+ \quad (3.12)$$

where $\underline{x}^{-1/2}$ is the diagonal matrix of the inverse square roots of the eigenvalues. Now orthonormal eigenvectors, \underline{D} , can be constructed such that

$$\underline{D} = \underline{C} \underline{X}^{-1/2} \quad (3.13)$$

$$\underline{D}^+ \underline{S} \underline{D} = \underline{X}^{-1/2} \underline{C}^+ \underline{S} \underline{C} \underline{X}^{-1/2} = \underline{X}^{-1/2} \underline{X} \underline{X}^{-1/2} = \underline{1} \quad (3.14)$$

Because the vectors between the A and B subunits are initially orthogonal to themselves, in principle B only needs

to be orthogonalized to A. Yet, because the system usually has a different symmetry than the subunits, precision is lost between overlap elements within the subunits. Therefore, we recommend orthogonalizing all the orbitals within the subunits for the new symmetry of the system.

Subunits

Before proceeding with the CSOV study, one needs to establish which subunit is A and which is B. Bauschlicher has shown that different choices of A and B will produce slightly different results.¹⁰⁹ We experimented with the different choices of A and B on the FeCO(C_{4v}) pseudopotential calculation using Schmidt orthogonalization and symmetric orthogonalization. Bauschlicher used only Schmidt orthogonalization in his work.¹⁰⁹ This leaves us with four calculations to perform. The first two take A as Fe and B as CO orthogonalized via the Schmidt and symmetric methods, and the second two take B as Fe and A as CO orthogonalized via the Schmidt and symmetric methods. The results are listed in Tables 3.1, 3.2, 3.3, and 3.4, respectively. In figure 3.2a the CSOV steps are outlined when Fe is A, and in figure 3.2b the CSOV steps are outlined when Fe is B. The Fe-C distance is 2.083 Å, and the C-O distance is 1.140 Å, which are the optimized distances in FeCO using this basis set. The

Schmidt and Symmetric Orthogonalization

A = Fe B = CO

MO Ordering = Fe_{occ} CO_{occ} CO_{virt} Fe_{virt}

Step 0 = Frozen orbital

Step 1 = CO space varies

Step 2 = CO + Fe virtual space

Step 3 = Fe space varies

Step 4 = Fe + CO virtual space

Step 5 = Final SCF

Figure 3.2a

Schmidt and Symmetric Orthogonalization

A = CO B = Fe

MO Ordering = CO_{occ} Fe_{occ} Fe_{virt} CO_{virt}

Step 0 = Frozen orbital

Step 1 = Fe space varies

Step 2 = Fe + CO virtual space

Step 3 = CO space varies

Step 4 = CO + Fe virtual space

Step 5 = Final SCF

Figure 3.2b

Table 3.1
Schmidt Orthogonalized
Feocc COocc COvirt Fevirt

Step	Estep	ΔE_{step}	<u>Charges</u>		
			Fe	C	O
0	-1.59		0.00	+0.23	-0.23
1	-1.53	0.06	0.00	+0.17	-0.17
2	-1.06	0.47	-0.10	+0.27	-0.17
3	-0.76	0.30	-0.02	+0.21	-0.19
4	-0.09	0.67	+0.07	+0.13	-0.20
SCF	+0.12	0.21	+0.04	+0.16	-0.19

Estep and ΔE_{step} are listed in eV

Charges are in atomic units

Table 3.2
Symmetrically Orthogonalized
Feocc COocc COvirt Fevirt

Step	Estep	ΔE_{step}	<u>Charges</u>		
			Fe	C	O
0	-1.59		0.00	+0.23	-0.23
1	-1.50	0.09	-0.08	+0.27	-0.19
2	-1.09	0.41	-0.10	+0.28	-0.18
3	-0.72	0.37	-0.04	+0.22	-0.18
4	-0.01	0.71	+0.08	+0.13	-0.21
SCF	+0.12	0.13	+0.04	+0.16	-0.19

Estep and ΔE_{step} are listed in eV

Charges are in atomic units

Table 3.3
Schmidt Orthogonalized
CO_{occ} Fe_{occ} Fe_{virt} CO_{virt}

Step	E _{step}	ΔE _{step}	<u>Charges</u>		
			Fe	C	O
0	-1.59		0.00	+0.23	-0.23
1	-1.00	0.59	0.00	+0.23	-0.23
2	-0.44	0.56	+0.15	+0.12	-0.26
3	-0.36	0.08	+0.13	+0.07	-0.19
4	+0.11	0.47	+0.01	+0.18	-0.19
SCF	+0.12	0.01	+0.04	+0.16	-0.19

E_{step} and ΔE_{step} are listed in eV

Charges are in atomic units

Table 3.4
Symmetrically Orthogonalized
CO_{occ} Fe_{occ} Fe_{virt} CO_{virt}

Step	Estep	Δ Estep	<u>Charges</u>		
			Fe	C	O
0	-1.59		0.00	+0.23	-0.23
1	-1.12	0.47	+0.05	+0.18	-0.23
2	-0.56	0.56	+0.17	+0.09	-0.26
3	-0.49	0.07	+0.16	+0.03	-0.19
4	+0.08	0.57	0.00	+0.19	-0.19
SCF	+0.12	0.04	+0.04	+0.16	-0.19

Estep and Δ Estep are listed in eV

Charges are in atomic units

reference energy from the separate A and B units is
-134.125371 a.u.

First, let us compare the different orthogonalization methods. In tables 3.1 and 3.3 are the results for the Schmidt orthogonalized orbitals, and in table 3.2 and 3.4 are the results for the symmetrically orthogonalized orbitals. In the frozen orbital step, the E_{step} and the charges from the Mulliken population analysis are the same for each study. This is expected, for no orbital variation has occurred. Also, the repulsion between the Fe and CO should not change regardless of the orthogonalization method or the choice of A and B. Of course, the last step also contains the same values for each study, because all of the orbitals vary in this step to produce the final SCF energy.

In step 1 differences between the different schemes occur. When CO is taken as B, tables 3.1 and 3.2, the charge on the Fe atom is 0.00 for the Schmidt orbitals versus -0.08 for the symmetric orbitals. Likewise, when Fe is taken as B, tables 3.3 and 3.4, the charge on the Fe atom remained 0.00 for the Schmidt orbitals, while the charge on the Fe atom changed to +0.05 for the symmetric orbitals.

This bleeding of charge during the orbital variation in step 1 is a serious problem with the symmetric orbitals, because in step 1 the subunit orbitals are not mixing with the other subunit in each study. We would like to keep charge transfer null until the subunits are allowed to mix. The

charge transfer in the symmetric orbitals has occurred, because diagonalizing \underline{X} in equation 3.10 causes orbital mixing inadvertently. Therefore, we recommend using Schmidt orthogonalization in the CSOV method.

With this in mind we only need to compare the choice of A and B with respect to the Schmidt orbitals in tables 3.1 and 3.3. In table 3.1 Fe is taken to be A, and in table 3.3 Fe is taken to be B. When Fe is allowed to relax in the field of CO, step 3 in table 3.1 and step 1 in table 3.3, the ΔE_{step} is 0.30 and 0.59 eV, respectively. The value is smaller when the Fe relaxation is step 3, because the CO has already relaxed and causes less perturbation on the Fe. When CO is allowed to relax in the field of Fe, step 1 in table 3.1 and step 3 in table 3.3, the ΔE_{step} is 0.06 and 0.08 eV, respectively, which is approximately equal unlike the Fe relaxation. Furthermore, if we analyze the Fe donation into the CO virtual orbitals, step 4 in table 3.1 and step 2 in table 3.3, the ΔE_{step} is 0.67 and 0.56, respectively. If we analyze the CO donation into the Fe virtual orbitals, step 2 in table 3.1 and step 4 in table 3.3, the ΔE_{step} is the same at 0.47 eV. Based on these results it appears the Fe is more sensitive to the choice of A and B, while the CO appears to be unaffected by the choice of A and B. Therefore, we only need to decide if Fe should be A or B. If we analyze the final SCF step in the two studies, then Fe as B in table 3.3 should be chosen, because this particular CSOV study has

accounted for most of the SCF energy by the final step. Thus, the energies for the major binding interactions have been determined with very little dependence between the CSOV steps. Hence, in all of our CSOV studies on other Fe_xCO clusters, we chose Fe as subunit B.

Fock Matrices

There are three kinds of Fock matrices used in the Hartree-Fock procedure: closed shell restricted Hartree-Fock (RHF), open shell restricted Hartree-Fock (ROHF), and unrestricted Hartree-Fock (UHF).⁵⁰ RHF is used for closed shell molecules and clusters, where there are only doubly occupied orbitals. For open shell systems, which include partially filled orbitals, the other kinds of Fock matrices need to be used. ROHF dictates that the α and β electrons in the same orbital have the same energy. In UHF theory, the α and β electrons can have a different orbitals. We have implemented the CSOV analysis to treat these different Fock matrices.

In RHF calculations there is only one Fock matrix to be diagonalized. Therefore, implementation of the CSOV analysis is straightforward. In the GAMESS program the non-orthogonal eigenvectors are used to construct the eigenvector equation as described in equations 2.17 and 2.18. Consequently, to convert the Fock matrix into the CSOV Fock matrix, F_{CSOV} , one

only needs to use the eigenvectors in the variational space, $\underline{\underline{C}}_v$.

$$\underline{\underline{F}}_{\text{csov}} = \underline{\underline{C}}_v^+ \underline{\underline{F}} \underline{\underline{C}}_v \quad (3.15)$$

The new variational eigenvectors are backtransformed from the eigenvectors of the Fock matrix.

$$\underline{\underline{C}}_{v\text{new}} = \underline{\underline{C}}_{v\text{old}} \underline{\underline{1}}_{\text{csov}} \quad (3.16)$$

For an ROHF calculation based on a single Slater determinant, the Fock matrix can be partitioned into a doubly occupied space, a singly occupied space, and a virtual space, where

$$\underline{\underline{F}}_{\text{ROHF}} = (\underline{\underline{F}}_{\text{double}}; \underline{\underline{F}}_{\text{single}}; \underline{\underline{F}}_{\text{virtual}}) \quad (3.17)$$

Therefore, the variational space is comprised of the variational space of the doubly and singly occupied orbitals and the variation virtual orbitals.

$$\underline{\underline{C}}_v = (\underline{\underline{C}}_v(\text{double}); \underline{\underline{C}}_v(\text{single}); \underline{\underline{C}}_v(\text{virtual})) \quad (3.18)$$

For the UHF Hamiltonian there are two Fock matrices for the α and β electrons. Therefore, one needs to partition the

variational space for the α and β electrons to produce two CSOV Fock matrices.

$$\underline{\underline{F}}_{\text{csov}\alpha} = \underline{\underline{C}}_{\text{v}\alpha}^{\dagger} \underline{\underline{F}}_{\alpha} \underline{\underline{C}}_{\text{v}\alpha} \quad (3.19)$$

$$\underline{\underline{F}}_{\text{csov}\beta} = \underline{\underline{C}}_{\text{v}\beta}^{\dagger} \underline{\underline{F}}_{\beta} \underline{\underline{C}}_{\text{v}\beta} \quad (3.20)$$

DIIS

The DIIS routine could not be used directly with the CSOV method in the GAMESS program, because there is a constant error associated with the nonvariational part of the Fock matrix. Therefore, we had to remove the fixed space from the Fock matrix in the DIIS routine. This was done accordingly. First, we multiply the Fock matrix by $\mathbf{1}$, where $\mathbf{1}$ is equal to $\underline{\underline{C}}^{\dagger}$ times $(\underline{\underline{C}}^{\dagger})^{-1}$ and $\underline{\underline{C}}$ times $\underline{\underline{C}}^{-1}$.

$$\underline{\underline{F}} = \underline{\underline{\mathbf{1}}} \underline{\underline{F}} \underline{\underline{\mathbf{1}}} \quad (3.21)$$

$$\underline{\underline{F}} = (\underline{\underline{C}}^{\dagger})^{-1} \underline{\underline{C}}^{\dagger} \underline{\underline{F}} \underline{\underline{C}} (\underline{\underline{C}}^{-1}) \quad (3.22)$$

If we partition $\underline{\underline{C}}$ into the fixed, C_a , and variational spaces, C_b , then we have

$$\underline{\underline{C}} = (C_a | C_b) \quad (3.23)$$

(3.24)

$$\underline{\underline{F}} = (\underline{\underline{C}}^+)^{-1} \left(\begin{array}{c|c} C_a^+ F C_a & C_a^+ F C_b \\ \hline C_b^+ F C_a & C_b^+ F C_b \end{array} \right) (\underline{\underline{C}}^{-1})$$

The inverse of $\underline{\underline{C}}$ and $\underline{\underline{C}}^+$ is derived from the orthonormality condition such that

$$(\underline{\underline{C}}^{-1}) = \underline{\underline{C}}^+ \underline{\underline{S}} \quad (3.25)$$

$$(\underline{\underline{C}}^+)^{-1} = \underline{\underline{S}} \underline{\underline{C}} \quad (3.26)$$

We remove the fixed space, C_a , from the eigenvectors and Fock matrix, and now F' is defined by

$$\underline{\underline{F}}' = \underline{\underline{S}} (0|C_b) (0|C_b^+) \underline{\underline{F}} (0|C_b) (0|C_b^+) \underline{\underline{S}} \quad (3.27)$$

$$\underline{\underline{F}}' = \underline{\underline{S}} C_b C_b^+ \underline{\underline{F}} C_b C_b^+ \underline{\underline{S}} \quad (3.28)$$

D then becomes the transformation matrix such that

$$\underline{\underline{D}} = C_b C_b^+ \underline{\underline{S}} \quad (3.29)$$

F' is transformed by D , and it is the Fock matrix used in the DIIS routine.

$$\underline{\underline{F}}' = \underline{\underline{D}}^+ \underline{\underline{F}} \underline{\underline{D}} \quad (3.30)$$

Even with this correction DIIS tends to produce oscillating energies. Consequently, one should use DIIS only for a few SCF cycles during the CSOV method. The final calculation convergences is completed with the aid of level shifting, extrapolation, or damping.

Chapter 4

Aluminum on Graphite

One research topic, in which our group has been interested, is adsorption of aluminum on graphite. Susil Silva performed geometry optimizations on clusters to find the preferred aluminum adsorption site. Because we were interested in understanding the major bonding contributions, our first CSOV studies were performed using the optimized geometries from these cluster calculations.¹¹⁰ We also felt this would be a good system to judge the usefulness of the CSOV method.

Scanning tunneling microscopy (STM) is becoming an important tool for characterizing surfaces. For example, Ganz, Sattler, and Clarke recently used STM to directly image with atomic resolution gold, silver, and aluminum atoms and clusters deposited on a cleaved graphite surface.¹¹¹ Here we report cluster calculations which attempt to model the adsorption of Al atoms on graphite. The Ganz et al. STM images of Al atoms on graphite are reproducible and long lived suggesting strong binding interactions with the adsorbate and the graphite substrate. The STM images find the Al atoms directly above a surface beta carbon, where the surface layer of graphite can be divided into an α set consisting of carbons directly above carbon atoms in the second graphite layer and the β set containing the remaining

carbon atoms. One objective of this work is to examine whether cluster calculations can reproduce the STM observation. However, a difficulty might be anticipated owing to Ganz et al. always finding a single Al atom adsorbed within 10 Å of a large Al cluster island which may be perturbing the graphite surface.¹¹¹ Further experimental evidence for long range perturbations of the graphite surface has recently been given by Mizes and Foster.¹¹²

Computational Details

In this preliminary study we examine what type of cluster is needed for the Al atom to become bound. Due to computational limitations we perform the calculations at a minimal STO-3G basis Hartree-Fock level. We feel such calculations are qualitatively useful for modeling the interaction between Al and graphite but recognize that larger basis sets and configuration interaction might be needed for quantitative results. The clusters consist of rings of carbon atoms arranged as fragments of the graphite. Following the approach of other workers^{113,114} the clusters are terminated with hydrogen atoms. Three different adsorption sites are examined: (A) on top site, with Al directly above a carbon atom; (B) bridging site, with Al above the center of a C-C bond; and (C) open site, with Al above the center of a C₆ hexagon. Again because of computational limitations we were

unable to perform calculations on a carbon cluster large enough to include both an α and a β carbon surrounded by a shell of neighboring atoms. However, as we indicate below, we find a double carbon layer is necessary to obtain the result that the Al adsorption at the on top (A) site is more stable than the open site (C).

All the *ab initio* calculations were performed using the GAMESS program⁵¹ on MicroVAX II, VAX 8550, or the San Diego Cray X/MP supercomputer. Due to the large storage requirements of the integral files, this was another factor in choosing the STO-3G minimal basis set¹¹⁵ in the calculations. The STO-3G basis is not quantitative but is well established for producing correct trends in hydrocarbon molecules.¹¹⁶ The effectiveness of the Al STO-3G basis was also checked by performing a complete geometry optimization of $\text{Al}(\text{CH}_3)_3$, which gave an Al-C distance of 1.982 Å in reasonable agreement with the experimental value of 1.957 Å.¹¹⁷ The total energies were computed using either closed or open shell restricted Hartree-Fock calculations depending on the number of electrons in the cluster.

The nature of the interactions between Al and the C_{10}H_8 and C_{13}H_9 clusters was analyzed using the CSOV method. By examining the differences between the energies obtained for various unconstrained molecular orbital spaces, we identify the major molecular orbital interactions between the adsorbing Al and the graphite cluster.

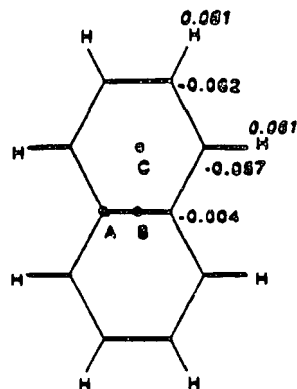
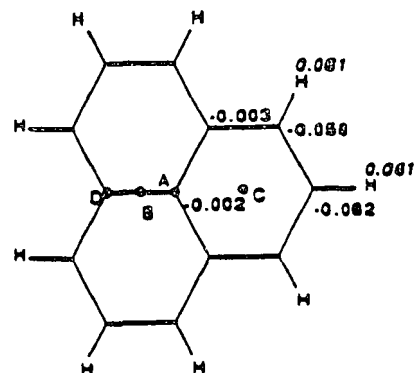
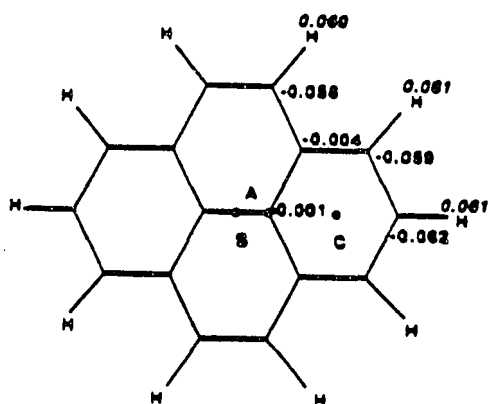
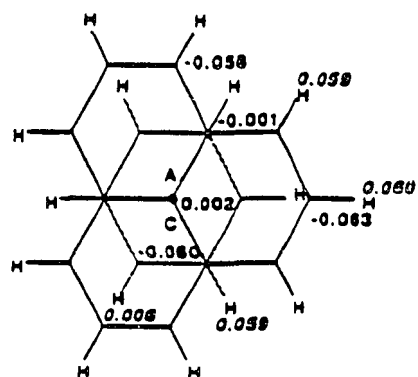
Results and Discussion

Figure 4.1 shows the geometries of the four different carbon clusters $C_{10}H_8$, $C_{13}H_9$, $C_{16}H_{10}$, and $C_{19}H_{15}$ used in the calculations. The cluster C-C bond length, 1.42 Å, is taken from the graphite experimental distance and the C-H bond length, 1.09 Å, is typical for organic molecules. Some indication of the naked aromatic molecules ability to mimic the properties of the graphite surface is indicated by the net atomic charges given in figure 4.1. The carbon charges are all negative and never less than -0.07. The clusters' central atoms, those atoms which are only bound to neighboring carbon atoms, are very close to neutral. The outer carbon atoms are slightly more negative due to donation of electrons from the hydrogen atom. The cohesive energy (CE), given by

$$CE = [E(C_nH_m) - nE(C) - mE(H)] / (n+m) \quad (4.1)$$

where $E(C_nH_m)$ is the cluster's total energy and $E(X)$ is the atomic energy, is another useful measure of the clusters effectiveness to simulate graphite.¹¹³ Our CE values for $C_{10}H_8$ (-4.46eV), $C_{13}H_9$ (-4.54eV), $C_{16}H_{10}$ (-4.66eV), and $C_{19}H_{15}$ (-4.46eV) are uniform and in reasonable agreement with the Almlöf and Luthi theoretical estimate of 5.4 eV, who used

Aluminum on Graphite Clusters

a) C₁₀H₈b) C₁₃H₉c) C₁₆H₁₀d) C₁₉H₁₅

The solid circles indicate adsorption sites. The C₁₉H₁₅ cluster consists of the C₁₃H₉ (solid lines) on top of a C₆H₆ cluster (dotted lines). In C₉H₁₅ site (A) is above the C₁₃H₉ layer and site (C) is below the C₆H₆ layer.

Figure 4.1

a better quality basis set¹¹⁴, but in poor agreement with experimental CE estimated at 7.6 eV.¹¹⁸ The discrepancy is attributed to the neglect of electron correlation and the minimal basis set. For the double layer cluster C₁₉H₁₅ we find a small repulsive interaction of 0.05 eV relative to the separated aromatic molecules C₆H₆ and C₁₃H₉. Such a small energy is not too surprising if the graphite interlayer forces are due to Van der Waals interactions. With these limitations taken into consideration and from the experience of others we feel our clusters are a reasonable starting point for modeling the Al adsorption on graphite.

The adsorption calculations with the Al atom positioned above the different sites on the four different clusters labelled in figure 4.1 are summarized in table 4.1. The stable geometry for the Al Adsorbate at different sites is found by minimizing the clusters total energy with respect to the Al to surface distance. In the single layer clusters we find the Al adsorbed over the open site (C) to give the lowest energy, followed by the Al on top the carbon atom in site (A) as the most stable adsorption position in agreement with the STM experiment result. However at the present time we have no explanation why the double layer calculation agrees with the experiment, and the result may be fortuitous. The equilibrium distances for the Al atom above the cluster, given in table 4.1, appear reasonable when compared to the Al-C distance in Al(CH₃)₃. At the on top sites the Al-C

Table 4.1
Equilibrium C-Al Bond Length (d), Al Binding Energy (BE), and
Charge (q)

<u>Cluster</u>	<u>Site</u>	<u>d/Å</u>	<u>BE/eV</u>	<u>q/e</u>
C ₁₀ H ₈ AL	A	2.20	-0.87 ^a	-0.059
	B	2.20 (2.08)	-1.17 ^a	-0.054
	C	2.40 (1.93)	-0.67	0.209
C ₁₃ H ₉ AL	A	2.14	-0.58	0.456
	B	2.27 (2.16)	-0.29	0.395
	C	2.48 (2.03)	0.79	0.245
	D	2.11	0.36	0.263
C ₁₆ H ₁₀ AL	A	2.20	-1.16 ^a	-0.172
	B	2.28 (2.17)	-1.93	0.437
	C	2.45 (2.00)	-0.65	0.226
C ₁₉ H ₁₅ AL	A	2.18	-0.55	0.462
	C	2.50 (2.06)	-1.47	0.289

Numbers in brackets are C to Al distance from the graphite plane.

^a These sites are non-binding and the BE and q are calculated at the C-Al bond length of 2.20 Å.

distance is found to be 0.2 Å longer than in $\text{Al}(\text{CH}_3)_3$ while in the bridging and open sites the difference is much larger. From the Al to cluster binding energy (BE), given by

$$\text{BE} = E(\text{C}_n\text{H}_m) + E(\text{Al}) - E(\text{C}_n\text{H}_m\text{Al}) \quad (4.2)$$

we find, apart from sites (C) and (D) for C_{13}H_9 , the BE to be negative indicating that $\text{C}_n\text{H}_m\text{Al}$ is unstable relative to the separated C_nH_m and Al. However our calculations, except for (A) and (B) on C_{10}H_8 and (A) on $\text{C}_{16}\text{H}_{10}$, exhibit total energy variations with respect to the Al-surface distance with fairly deep minima. The potential energy well depths range from 0.5 eV for site (C) on C_{10}H_8 to greater than 2 eV for sites (A) and (C) on C_{13}H_9 and $\text{C}_{19}\text{H}_{15}$. Hence once the Al gets inside the potential well it should be strongly bound to the graphite. Results for Al adsorbing at the on top site (D) at the C_{13}H_9 cluster edge are also included in table 4.1 to illustrate the calculations sensitivity to the cluster shape.

The Al net charges are also given in Table 4.1. The Al loses most electrons when it is located at an on top site (A) and when the cluster has an odd number of carbon atoms. A Mulliken population analysis shows that the donated Al electrons are delocalized over the entire cluster. For all adsorption sites the carbon net charges show an oscillatory distribution. For example, for Al at site (A) on C_{13}H_9 we find -0.10 on the site (A) carbon, while the three

neighboring carbon atoms are slightly positive with +0.05, and the next nearest neighbor carbon atoms have -0.13. These charge oscillations mimic the long range electronic perturbations caused by defects recently observed by Mizes and Foster using STM.¹¹² A striking feature for each cluster calculation is that we find the charge distribution to be insensitive to the position of Al adsorption. After analyzing each naked clusters' molecular orbitals we conclude the charge distribution is derived from the carbon clusters lowest unoccupied π molecular orbital (LUMO). The single layer carbon clusters are examples of alternant conjugated hydrocarbons and simple π Huckel theory requires for alternant systems with an odd number of carbon atoms that the LUMO is half occupied and has zero energy relative to the carbon atom, while for alternates with an even number of carbon atoms the LUMO is empty and has positive energy.¹¹⁸ Thus for the on top site (A), the Al can readily donate electrons to the C₁₃H₉ and the C₁₉H₁₅ LUMO while in C₁₀H₈ and C₁₆H₁₀ the donation is more difficult and the Al gains electrons. In all four site (A) clusters the site (A) carbon becomes negatively charged relative to the naked clusters and this is due to electrons entering both σ and π orbitals on the cluster. However none of this increase in carbon (A) charge directly enters the LUMO, because the LUMO carbon (A) π orbital coefficient is zero. The site (C) charge distribution for C₁₉H₁₅ is striking in that the Al electrons

are donated to the second layer carbon atoms rather than the C₆H₆ top layer. This is still consistent with electron donation to the π LUMO, but now the LUMO is localized on the C₁₃H₉ layer. We have no explanation for the different amounts of Al electron donation at the different adsorption sites but expect it to be related to differing amounts of electrostatic repulsion.

Unfortunately the charge distributions above do not provide any simple explanation why the on top site (A) is the favored Al adsorption site. In table 4.2 we report the results of the CSOV analysis for Al interacting at the different adsorption sites on the C₁₀H₈ and C₁₃H₉ clusters. The calculations were performed at equilibrium geometries given in table 4.1, but now the open shell calculations were performed at the unrestricted Hartree-Fock level which gives slightly different energies and charge distributions to those obtained at the restricted Hartree-Fock level. In our analysis we have identified 5 major CSOV energy changes, and these steps are listed in figure 4.2. Step 0 is simply the sum of the energy of the isolated cluster and the Al atom, the reference energy. Step 1 gives the energy of superimposing the cluster and Al orbitals at the equilibrium geometry; the Al orbitals were Schmidt orthogonalized to the cluster occupied orbitals. In step 2 the Al orbitals are allowed to relax, and the constrained space consists of the cluster orbitals. The atomic relaxation is small, and in both

CSOV Steps for Aluminum on Graphite Clusters

Step 0 : Reference energy = $E(\text{Al}) + E(\text{Cluster})$

Step 1 : Frozen orbital energy.

Step 2 : Al orbitals vary

Step 3 : Cluster p orbitals vary

Step 4 : Al and Cluster p orbitals vary

Step 5 : Final SCF energy

Figure 4.2

Table 4.2

CSOV Energy Analysis for the Different Adsorption Sites

C ₁₀ H ₈ Al			
<u>Step</u>	<u>Site (A)</u>	<u>Site (B)</u>	<u>Site (C)</u>
1	-0.5899 P _x	-0.5600 P _y	-0.5073 P _y
2	-0.5978 P _x	-0.5714 P _y	-0.5202 P _y
3	-0.6386	-0.5751	-0.5225
4	-0.7027	-0.6479	-0.6717
SCF	-0.7265	-0.6535	-0.6839
0	-0.6946	-0.6946	-0.6946

C ₁₃ H ₉ Al			
<u>Step</u>	<u>Site (A)</u>	<u>Site (B)</u>	<u>Site (C)</u>
1	-0.3545 P _x	-0.3646 P _y	-0.3293 P _y
2	-0.3633 P _x	-0.3732 P _y	-0.3388 P _y
3	-0.4547	-0.4652	-0.4310
4	-0.5028	-0.5214	-0.5214
5	-0.5331	-0.5513	-0.5463
0	-0.6015	-0.6013	-0.6013

All the C₁₀H₈Al energies are in a.u. and have -617 a.u. added.

All the C₁₃H₉Al energies are in a.u. and have -730 a.u. added.

P_x and P_y represents the occupancy of the Al p orbital.

C₁₀H₈ and C₁₃H₉ the on top site (A) has lower energy than site (C). Also at this stage and at full convergence we find that the Al 3p electron prefers an orbital parallel to the surface; in an ideal cluster mimicking the extended surface the two parallel Al 3p orbitals are degenerate at the high symmetry adsorption sites (A), (B), and (C). For the CSOV step 3 we constrain the Al orbitals and relax the cluster π orbitals. In C₁₀H₈ the step 3 energy gain is small, especially for sites (B) and (C), while for C₁₃H₉ we obtain 0.09 a.u. of energy which is up to 60% of the energy in going from step 2 to step 4. Step 4 consists of relaxing all the Al orbitals and all the cluster π orbitals, both occupied and virtual. Step 5 corresponds to the full unconstrained UHF calculation on the cluster. In going from step 4 to step 5, the major energy contribution is coming from the clusters σ molecular orbitals. For both cluster the σ energy contribution is small. The largest step 2 to step 4 energy change, 0.15 a.u. for C₁₀H₈ and 0.19 a.u. for C₁₃H₉, occur at site (C) adsorption site in both clusters. We conclude from the CSOV analysis that superposition of the Al and the cluster favors adsorption at the on top site (A) rather than the open site (C). This superposition is repulsive relative to the separated Al atom and the cluster. The repulsion is reduced largely by mixing between the Al orbitals and the cluster π orbitals, where site (C) is stabilized most by this orbital interaction. The final adsorption site will be

decided by a balance between these two effects. The presence of other atoms or clusters on the graphite surface could alter this balance and influence the structure of the final adsorption site.

Conclusion

The adsorption of an Al atom on four different clusters has been investigated. Only the double layer cluster reproduced results in agreement with STM experiments. The charge distributions on the clusters are oscillatory and essentially independent of the Al position. The form of the naked clusters LUMO largely determines the charge distribution and will vary with the clusters geometry. The Al to cluster bonding interaction has been analyzed using CSOV calculations. The initial superposition of the Al and cluster wavefunction energetically favors the on top (A) geometry versus the open site (C). However the mixing of the cluster π orbitals with the Al orbitals stabilizes site (C) more than site (A).

Chapter 5

Fe_xCO Clusters

In this chapter we theoretically compare the bonding of the vertical CO, CO(α_1) and CO(α_2), with the tilted CO, CO(α_3), chemisorption on the Fe(100) surface. Accurate calculations using large basis sets are difficult, and we thus report here calculations for minimal clusters with only one and two Fe atoms. Although these clusters are too small to yield high accuracy results to enable a direct comparison with experiment, we expect them to provide qualitatively useful trends and predictions. We are not aware of an experimental geometry for the CO(α_1) and CO(α_2) structures in the literature and approximate them by taking the CO normal to the Fe(100) surface directly above a single Fe atom and a bridging two fold-fold site. The vertical structures are shown by figure 5.1a and figure 5.1b. The tilted structure, CO(α_3), is centered at the 4-fold site with the CO tilted at an angle of 55° from the normal to the plane of the Fe surface. This is shown in figure 5.1c. To model the on top site we used a FeCO cluster in C_{4v} symmetry, figure 5.2a. It will be designated as FeCO(C_{4v}). To model the bridging and tilted structures, we used an Fe₂CO cluster in C_{2v} and C_s symmetry depicted in figures 5.2b and 5.2c, respectively. They will be designated as Fe₂CO(C_{2v}) and Fe₂CO(C_s).

CO Adsorption on Fe(100) Surface

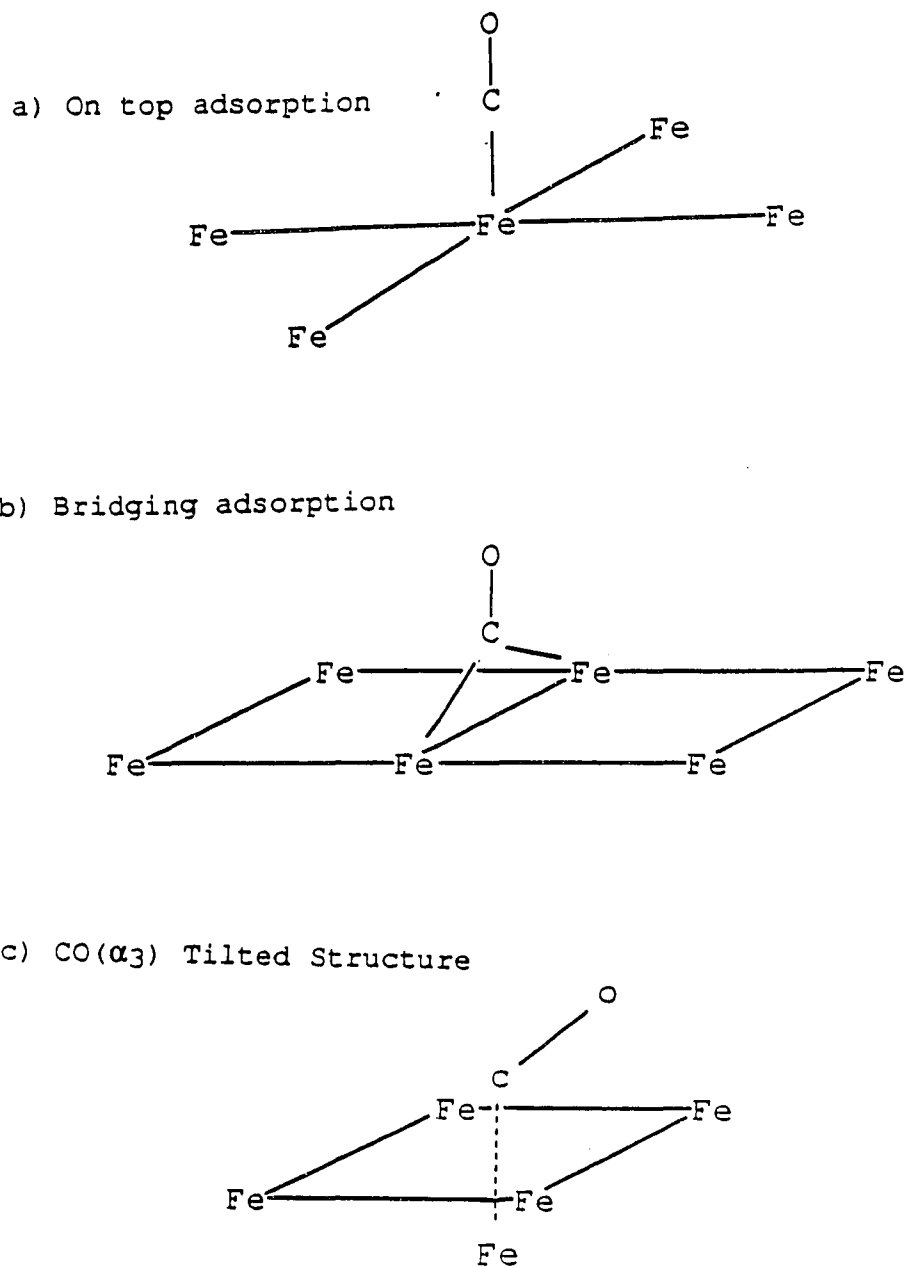


Figure 5.1

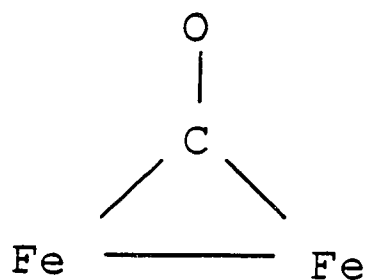
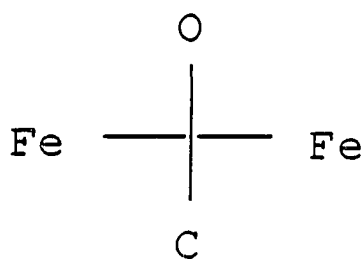
Fe_xCO Clustersa) $\text{FeCO}(\text{C}_{4v})$ b) $\text{Fe}_2\text{CO}(\text{C}_{2v})$ c) $\text{Fe}_2\text{CO}(\text{C}_s)$ 

Figure 5.2

Due to early problems with SCF convergence, which made performing geometry optimizations difficult, the first set of calculations were performed using a full basis set and experimentally suggested geometries.¹¹⁹ These calculations, describe in the first part of this chapter, serve to provide information about the electronic states of the CO interacting with the Fe. Afterwards geometry optimizations were performed using a pseudopotential basis and the full basis set. These calculations serve to determine the favorable electronic states for optimizing the CO position on Fe, and this work is discussed in the remainder of the chapter. We also calculate CO vibrational stretching frequencies, which enable comparison with experimental values.

Computational Details

Unrestricted Hartree-Fock (UHF) calculations were performed using the GAMESS program.⁵¹ The UHF method was chosen to facilitate computing spin polarization information as well as to make the calculations more computationally tractable. Both a pseudopotential basis set and a full basis set were used in our calculations regarding Fe. The pseudopotential for Fe was developed by Hay and Wadt.¹²⁰ The valence basis set was a contracted double zeta (3s2p5d/2s2p2d) given by Hay and Wadt.¹²⁰ In the full basis set contraction 3 of the Wachters primitive basis¹²¹

augmented by two diffuse 4p functions, with exponents scaled by 1.5, and the diffuse d function of Hay¹²² was used as a basis set. The final basis set (14s11p6d/8s6p4d) was shown to provide good results for Fe in earlier work by Bauschlicher et al.^{32-34,123} The C and O basis set was the Dunning-Hay set (9s5p/3s2p).¹²⁴ All geometry optimizations were performed using gradient techniques, and the partial geometry optimizations were performed using the Head technique, which greatly reduces the computational effort for calculation of the gradient.¹⁰¹ The geometry is taken to be converged when the maximum cartesian gradient is less than 10^{-4} .

Vibrational stretching frequencies for CO were calculated at the optimized geometries, and they are expressed as inverse centimeters, cm^{-1} . In the harmonic oscillator model, the potential energy, V , is a parabolic curve, where

$$V = 1/2 kx^2 \quad (5.1)$$

k is the force constant and x is the displacement of the spring.¹²⁵ Because the Morse curve of a diatomic is near parabolic at the lower vibrational energy levels, we can use the harmonic oscillator potential to estimate the vibrational stretching frequency of CO. By plotting the energy versus the CO bond length, we can fit the curve to a quadratic equation.

$$E = ax^2 + bx + c \quad (5.2)$$

where the force constant, k , is related to quadratic coefficient by

$$k = 2a \quad (5.3)$$

The vibrational frequency of a harmonic oscillator is then expressed by

$$\nu = 1/2\pi (k/\mu)^{-1/2} \quad (5.4)$$

where μ is the reduced mass of CO. The curves were fitted using the Cricket program available on MacIntosh computers.

Experimental Geometry Calculations

For the $\text{FeCO}(\text{C}_{4v})$ and the $\text{Fe}_2\text{CO}(\text{C}_{2v})$ clusters we used typical experimental distances for the Fe-C and the C-O suggested by carbonyl complexes.²⁴ In the $\text{FeCO}(\text{C}_{4v})$ cluster the Fe-C distance was 1.84 Å, and the C-O distance was 1.15 Å. In $\text{Fe}_2\text{CO}(\text{C}_{2v})$ cluster the Fe₂ distance was taken as the bulk value of 2.87 Å with 2.05 Å for the Fe-C distance and 1.15 Å for C-O. For the $\text{Fe}_2\text{CO}(\text{C}_s)$ the Fe-Fe distance was given the bulk value, the Fe-C, Fe-O, and C-O distances are 2.05, 1.80, and 1.22 Å, respectively corresponding to the 55°

tilt geometry of the CO measured in the XPD experiment.⁴ The tilted CO distance is elongated by 0.07 Å relative to the vertical CO structures to be consistent with the geometry suggested by near-edge X-ray absorption fine-structure (NEXAFS) measurements.⁸ In the discussion below we always take the Fe₂ to lie along the z-axis.

We performed a CSOV analysis in order to examine the binding interactions between the CO and Fe clusters. The CSOV analysis followed the sequence of Bauschlicher et al.³³ Seven steps were performed and we started with Fe orbitals Schmidt orthogonalized to the CO orbitals. This was also determined to be the best scheme for FeCO in chapter 3. Step 0 in the analysis gives the frozen orbital (FO) energy. Step 1 varies only the Fe orbitals in the field of the CO molecule, and is denoted by $V(\text{Fe};\text{Fe})$; this step determines how the Fe orbitals relax in the presence of the CO molecule. In step 2 the Fe orbitals are allowed to mix with the CO σ orbitals, $V(\text{Fe};\text{full } \sigma \text{ virtual})$, thereby determining any charge transfer into the CO. Step 3 enables the Fe orbitals to mix with all the virtual orbitals, $V(\text{Fe};\text{full virtual})$; it is this step which measures the energetics of back donation into the CO π^* orbitals. Steps 4, 5, and 6 repeat steps 1, 2, and 3 but now for the CO. The CO orbitals vary in the field of the constrained Fe subunit, $V(\text{CO};\text{CO})$, in step 4. Steps 5, $V(\text{CO};\text{full } \sigma \text{ virtual})$, and step 6, $V(\text{CO};\text{full virtual})$, allow the CO to transfer charge to the Fe σ and π virtual orbitals,

respectively. The final step consists of varying all orbitals to obtain the SCF energy. The CSOV analysis is summarized in figure 5.3.

To mitigate convergence problems we also used the CSOV method as a frozen core approximation in the calculations involving Fe₂. Once the UHF orbitals for the isolated Fe₂ and CO subunits had been obtained, the Fe 1s-3p core orbitals and some of the high energy virtual orbitals were always retained in the constrained space.

The on top site is modeled by FeCO(C_{4v}) in the high spin state $^5\Sigma^-$ where the Fe atom initially has the configuration $d\sigma^1d\pi^4d\delta^24s^1$, which is expected to be a close approximation of the surface Fe atom configuration. The FeCO(C_{4v}) UHF CSOV steps, given in table 5.1, match closely the Restricted Hartree-Fock (RHF) and Complete Active Space SCF (CASSCF) results of Bauschlicher et al.³³ with UHF giving intermediate values when differences between the RHF and CASSCF calculations occur. For example, in step 3 the energy of the Fe to CO π^* backdonation is computed to be 0.92, 1.25, 1.68 eV by RHF, UHF, and CASSCF respectively. The only major difference is the UHF ΔE_{step} value of 0.48 eV for the CO σ donation to Fe at step 5, which is four times larger than that found in the RHF and CASSCF calculations. The UHF dipole moments also have values intermediate between the RHF and CASSCF calculations. The UHF dipole moment changes sign between steps 2 and 3 similar to the CASSCF. We expect this

CSOV Steps for the Fe_xCO Clusters

- Step 0 : frozen orbital
- Step 1 : Fe orbitals vary, $V(\text{Fe};\text{Fe})$
- Step 2 : Fe mixes with CO σ virtual, $V(\text{Fe};\text{CO } \sigma \text{ virtual})$
- Step 3 : Fe mixes with CO full virtual, $V(\text{Fe};\text{CO full virtual})$
- Step 4 : CO orbitals vary, $V(\text{CO};\text{CO})$
- Step 5 : CO mixes with Fe σ virtual, $V(\text{CO};\text{Fe } \sigma \text{ virtual})$
- Step 6 : CO mixes with Fe full virtual, $V(\text{CO};\text{Fe full virtual})$
- Step 7 : SCF energy

Figure 5.3

similarity between the FeCO UHF calculation and RHF and CASSCF calculations to continue for the Fe₂ clusters.

The initial electronic configuration for Fe₂ was taken as $d\sigma^1 d\sigma^*1 d\pi^4 d\pi^*4 d\delta^2 d\delta^*2 4s\sigma^2$ with multiplicity 7. This may not be the optimum wavefunction owing to the near degeneracy of the many other possible electronic configurations for the d electrons, but we feel such an Fe₂ wavefunction is reasonable based on the energy changes we observe in the CSOV analysis. The 3d orbitals in Fe₂ resemble the Fe orbitals in the FeCO but now the Fe₂ 4s orbitals are singlet coupled. In performing the CSOV analysis the symmetry of CO orbitals are used to define the σ and π spaces of the Fe₂. For example, for Fe₂CO(C_{2v}), with Fe₂ on the z axis and CO along the x axis, the CO σ orbitals have the same symmetry as the $4s\sigma$, $d\sigma(z^2)$, $d\pi(xz)$, and $d\delta(x^2-y^2)$ orbitals and could in principle interact with them. Similarly the CO π orbitals can interact with $4s\sigma^*$, $d\sigma^*(z^2)$, $d\pi(yz)$, $d\pi^*(xz)$ and $d\delta(x^2-y^2)$. In the tilted structure, with CO now parallel to the x axis, the division into σ and π spaces is less clear cut because both the CO σ and π_y orbitals transform as a' irreducible representations in the C_s point group. In step 2 of the CSOV analysis the Fe₂ orbitals were only allowed to interact with the CO $s\sigma$ and $p\sigma$ virtual orbitals; in step 3 the CO π virtuals were added to the orbital variation space. While in step 5 the CO orbitals were allowed to donate into the virtual a' orbitals, and in step 6 the full virtual space

included the a'' orbitals. Using the CO to specify the symmetry in the CSOV analysis suggest the dimer configuration $d\sigma^1 d\sigma^{*1} d\pi^2 d\pi^{*2} d\delta^4 d\delta^{*4} s\sigma^2$ could also be important for the tilted CO structure. The Fe_2 $d\delta$ and $d\delta^*$ orbitals have appropriate symmetry for donation into the CO π^* orbitals and the $d\delta$ -CO π^* orbital overlap should be comparable to the $d\pi$ -CO π overlap. However, the changes we find in step 1 of the CSOV analysis suggest the Fe_2 configuration with $d\pi$ orbitals completely filled is the most preferred.

The CSOV results for the on-top, bridging and tilted CO structures are given in tables 5.1, 5.2, and 5.3, respectively. In all three cases the initial interaction energy E_{step} is negative. For the on-top and bridging sites this is most likely due to repulsion between the CO σ lone pair and the Fe electrons and has been previously discussed by Bauschlicher et al.³³ The largest repulsion is found in the tilted state where the CO σ orbital is directed away from the Fe_2 electron density. The repulsion now comes from superimposing the CO electron density on the Fe_2 density resulting partly from the shorter Fe-O distance. Substantial relaxation of the Fe orbitals is found in step 1 of the CSOV analysis. In the on-top case, $4s-4p\sigma$ hybridization takes place reducing overlap between the Fe orbitals and the CO 5σ orbital.³³ In the Fe_2 clusters a different relaxation process, consisting of rehybridizing the d orbitals, takes

Table 5.1
 CSOV Analysis for FeCO(C_{4v}) ⁵Σ⁻ State
 Full Basis Set

Geometry:

Fe-C distance = 1.84 Å

C-O distance = 1.15 Å

Reference Energy:

E(Fe) + E(CO) = -1374.954578

Steps	Estep	ΔEstep	Charges			<s ² >
			Fe	C	O	
FO	-2.69		0.00	0.25	-0.25	6.00
1	-1.67	1.03	0.00	0.25	-0.25	6.04
2	-1.63	0.03	0.02	0.23	-0.25	6.04
3	-0.39	1.25	0.32	0.01	-0.32	6.33
4	-0.27	0.12	0.36	-0.11	-0.24	6.34
5	0.20	0.48	0.13	0.11	-0.24	6.34
6	0.26	0.05	0.13	0.07	-0.20	6.36
SCF	0.43	0.17	0.21	0.01	-0.21	6.69

Energy values are in eV

Charges and spin values are in atomic units

Table 5.2
 CSOV Analysis for Fe₂CO(C_{2v})
 Full Basis Set

Geometry:

Fe-C distance = 2.05 Å

C-O distance = 1.15 Å

Reference Energy:

E(Fe₂) + E(CO) = -2637.222399

Steps	Estep	ΔE_{step}	Charges			$\langle s^2 \rangle$
			Fe	C	O	
FO	-6.07		0.00	0.25	-0.25	12.04
1	-4.02	2.06	0.00	0.25	-0.25	12.16
2	-3.95	0.07	0.00	0.24	-0.25	12.16
3	-3.29	0.65	0.10	0.10	-0.29	12.21
4	-3.20	0.09	0.12	-0.02	-0.21	12.21
5	-3.00	0.20	0.06	0.07	-0.20	12.21
6	-2.90	0.11	0.05	0.05	-0.14	12.22
SCF	-2.87	0.02	0.06	0.02	-0.14	12.29

Energy values are in eV

Charges and spin values are in atomic units

Table 5.3
 CSOV Analysis for Fe₂CO(C_s)
 Full Basis Set

Geometry:

Fe - C distance = 2.05 Å

Fe - O distance = 1.80 Å

C - O distance = 1.22 Å

Reference Energy:

E(Fe₂) + E(CO) = -2637.209420

Steps	Estep	ΔE_{step}	Charges			$\langle s^2 \rangle$
			Fe	C	O	
FO	-11.68		0.00	0.32	-0.32	12.04
1	-8.88	2.80	0.00	0.32	-0.32	12.31
2	-8.78	0.10	0.00	0.30	-0.30	12.30
3	-6.52	2.26	0.21	-0.02	-0.41	12.68
4	-6.23	0.29	0.17	0.14	-0.48	12.69
5	-5.87	0.36	0.11	0.21	-0.43	12.69
6	-5.63	0.25	0.08	0.24	-0.41	12.69
SCF	-5.30	0.33	0.20	0.10	-0.51	13.58

Energy values are in eV

Charges and spin values are in atomic units

place. The symmetry of the bridging CO structure allows the $d\pi$ and $d\delta$ orbitals to mix, and the original Fe₂ minority spin $d\pi$ orbitals now contain a 25% $d\delta$ component. The tilted CO structure allows even more of the original Fe₂ irreducible representations to mix but the calculations maintain slightly larger minority spin $d\pi$ orbital populations than found for the bridged structure. The fact that the Fe₂ minority spin d orbitals maintain their $d\pi$ and $d\pi^*$ large populations supports using our initial electronic configuration chosen for Fe₂. We should expect variational collapse to $d\sigma^1 d\sigma^*1 d\pi^2 d\pi^*2 d\delta^4 d\delta^*4 s\sigma^2$ if this state is preferred.

In step 2 ΔE_{step} is small showing that the Fe donation into the CO σ virtual orbitals is slight for all clusters. As expected we find the largest ΔE_{step} and the major bonding interactions occur in the third step when the Fe d electrons are back donated into the CO π virtual space. We discuss step 3 in more detail below. When the CO orbitals are relaxed in the field of the constrained Fe orbitals, in step 4, relatively small changes in the energy and CO charges occur for all three structures. The change in the Fe populations are due to the molecular orbitals having an admixture of Fe and CO coefficients at this stage. Step 5 models the CO σ donation to the metal and as noted previously by Bauschlicher et al.³³ ΔE_{step} is found to be much smaller than for the π^* back donation. This is consistent with Bauschlicher et al. who argue the interaction between the CO 5σ and Fe σ orbitals

is repulsive. However the σ donation ΔE_{step} is still small for the tilted CO structure even though the CO 5σ is not directed towards Fe_2 . In all three structures CSOV step 6 produces a small energy change. The on-top and 2-fold bridging clusters step 6 energies are close to their final SCF energies and charges indicating we have found the major bonding interactions for these structures. For the on-top structure Bauschlicher et al.³³ attribute the final energy difference due to the relatively large covalent mixing between the CO σ orbitals and the Fe $d\sigma$ orbital which can be adequately computed by a second pass through the CSOV steps 1-6. We find a similar effect in the UHF calculation. We expect 0.33 eV between step 6 and the full SCF for the tilted CO structure to be due to an even larger CO and Fe_2 orbital mixing.

We now examine in more detail the changes taking place between step 2 and step 3 of the CSOV calculation. As expected the largest energy change ΔE_{step} is found for the tilted state, the on-top structure is next while the bridging structure gains the least energy. It might be argued that some of ΔE_{step} in step 3 is due to further Fe_2 relaxation, but the large ΔE_{step} for the tilted structure clearly shows back bonding into the CO π^* orbitals occurs much more strongly here than for the other two structures. We note also, from consideration of the bridging structure, that differences in the ionization potentials between the Fe atom

and Fe₂ are not solely responsible for the increased back bonding of the tilted state. The largest CSOV charge transfers also take place at this stage with 0.30, 0.19, and 0.43 electrons transferred from the Fe atoms to the CO at the on-top, bridging, and tilted sites, respectively. An even larger electron transfer should be anticipated when the CO dissociates.

The spin expectation values $\langle S^2 \rangle$ for the UHF wavefunctions are also interesting at this stage. The on-top and tilted state wavefunctions exhibit small yet significant contaminations by spin multiplicities higher than 5 and 7, respectively. We have no explanation for this but it may indicate that there is another low lying electronic state, or that there are very important electron correlation effects. However, the changes in the Mulliken molecular orbital populations between step 2 and 3 also show spin dependent features. In all three sites only Fe minority spin electrons are donated into the CO π^* orbitals. In FeCO(C_{4v}) the degenerate minority spin d π orbital interacts with the CO π^* forming degenerate molecular orbitals each with 0.11 C p π and 0.04 O p π character. Only the CO π^* orbitals perpendicular to the Fe₂ axis are appreciably populated in the bridging structure. The predominantly Fe₂ d π orbital becomes populated with 0.10 C p_x character and 0.04 O p_x electrons. Again, only the minority spin orbitals in the tilted structure form an admixture of d π -CO π^* molecular orbitals, these include 0.16

C p_z and 0.05 O p_z electrons parallel and 0.10 C p and 0.04 p electrons perpendicular to the Fe₂ axis. Interesting spin dependent effects also take place with the molecular orbital energies. Surprisingly those minority spin $d\pi$ which interact with the CO π^* orbitals are little changed in energy in going from step 2 to 3. Instead the majority spin Fe d orbitals are shifted to lower energy. The shift is 3.0 eV in FeCO(C_{4v}), 0.8 eV in Fe₂CO(C_{2v}), and 1.6 eV for the majority spin d and 1.4 eV for the non-CO interacting minority spin d in Fe₂CO(C_s). A reduction in the d - d repulsion due to the d to CO back donation may be a cause of this shift. Below we discuss the implications of these results for interpreting the photoemission experiments of CO on Fe(100). The CSOV analysis clearly shows the major bonding interactions between CO and Fe take place at the π back donation stage. Our cluster models are presently too simple to provide a quantitative measure of the relative stabilities of the vertical versus the tilted structures. However, the large ΔE_{step} value found at the back bonding stage for the tilted structure is in agreement with experimental expectations. The reduced vibrational frequency for the tilted state correlates with large charge donation to the CO π^* orbital. Smaller back donation effects are found for the CO on-top structure suggesting a correlation with the CO(α_2) state. The CO bridging Fe₂ shows the smallest back donation changes and the

structure should have the highest CO stretching frequency perhaps as in the $\text{CO}(\alpha_1)$ state.

The final SCF calculations for each structure are also worth examining. The total Mulliken populations and net charges for free and bound CO are given in table 5.4. The bound CO net charges are basically unchanged from their π back donation values at step 3 of the CSOV analysis. The vertical CO structures have essentially neutral C atoms while the C in the tilted CO is more positive. In a larger cluster the positive charge on the C in tilted CO might be expected to be reduced due to an end-on Fe-C interaction. The largest anisotropy in the CO π populations are found in the tilted CO structure where the C β_{p_z} orbital parallel to the Fe_2 axis has a 0.38 population and the perpendicular C β_{p_x} orbital has a 0.55 population. Interestingly, the tilted structure oxygen has $p\pi_z$ and $p\pi_x$ populations close in value. The largest spin population anisotropies are also found in the tilted CO state where the majority spin C π population are relatively small even with respect to the free CO. Figure 5.4 shows the orbital energies obtained for the FeCO and tilted Fe_2CO structures. It is tempting to use these orbital energies to interpret the photoemission experiments for CO on Fe(100), although caution needs to be exercised, since Koopmans' Theorem can not be expected to be reliable because of the different relaxations for the ionized CO and Fe d orbitals. However, if the exchange splitting is ignored, the CO energy

Table 5.4
SCF Mulliken Majority (α) and Minority (β) Populations

		Isolated CO	
		$R_{CO} = 1.15 \text{ \AA}$	$R_{CO} = 1.22 \text{ \AA}$
		$\alpha=\beta$	$\alpha=\beta$
C	s	1.92	1.92
	p σ	0.50	0.48
	p π	0.23	0.22
	Net charge	0.24	0.30
O	s	1.90	1.92
	ps	0.68	0.68
	pp	0.76	0.78
	Net charge	-0.24	-0.30

Table 5.4 (continued)

		SCF Mulliken Majority (α) and Minority (β) Populations					
		FeCO (α_1)		Fe ₂ CO (α_2)		Fe ₂ CO (α_3)	
		α	β	α	β	α	β
C	s	1.78	1.72	1.85	1.84	1.85	1.92
	p σ	0.55	0.53	0.52	0.53	0.47	0.45
	p π	0.33	0.38	0.29	0.36	0.15	0.53
	p π_z			0.31	0.29	0.16	0.37
Net charge		0.01		0.02		0.10	
O	s	1.88	1.91	1.90	1.91	1.91	1.92
	p σ	0.68	0.67	0.67	0.66	0.69	0.65
	p π	0.68	0.86	0.73	0.84	0.82	0.88
	p π_z			0.71	0.72	0.79	0.83
Net charge		-0.21		-0.14		-0.50	
Net CO charge		-0.21		-0.13		-0.40	

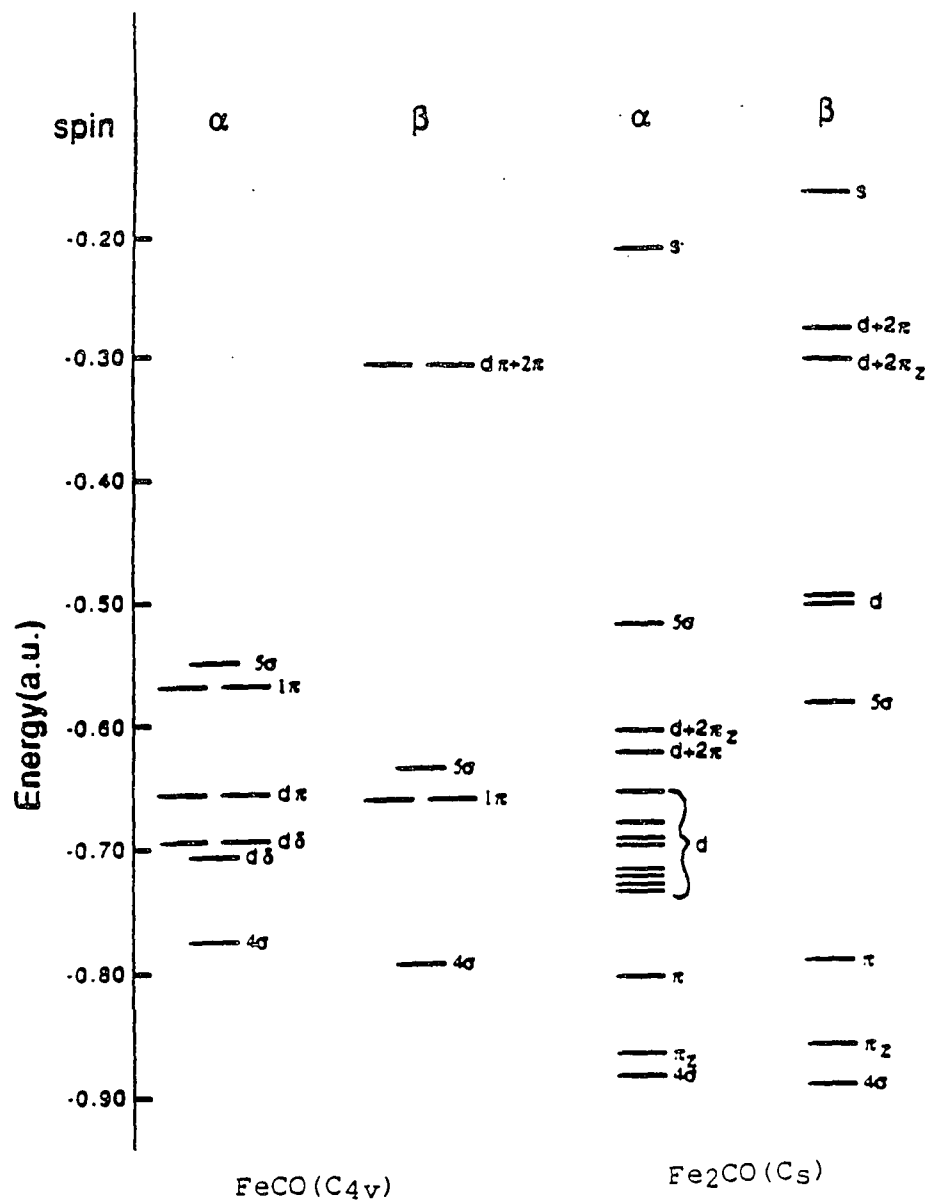
Occupied Majority (α) and Minority (β) Spin Orbital Energies

Figure 5.4

levels of FeCO, shown in figure 5.4, do simulate the 3 peak form found in the photoelectron spectra for the vertical CO.¹² Similarly, the tilted structure CO orbital energies are roughly in agreement with the photoelectron spectra in having 2 peaks and suggest the assignment of the 5σ level to the low energy peak at 8.0 eV and a mixed ($4\sigma+1\pi$) level at the high energy peak at 12.0 eV. However, Benndorf et al. suggest the peak at low binding energy is due to a mixed ($1\pi+5\sigma$) level and the high binding energy peak is due to a 4σ orbital.¹¹ Obviously, the calculated 4σ to 5σ splitting for the tilted structure is much too large and our assignment must be viewed as tentative since the calculated orbital energies will almost certainly be sensitive to the geometry of the cluster. Possible spin polarized photoemission features can also be identified from the Fe₂CO energy level diagram. The minority and majority spin features found in the spin polarized photoemission experiments at 1.7 and 2.3 eV binding energy, respectively,¹² may be associated with the Fe₂ $d\pi$ orbitals which interact with the tilted CO π^* orbitals labelled by $d+2\pi$. The energy of the minority spin d orbitals approximately remain at their original isolated Fe₂ values and are populated by 25% with C $p\pi$ electrons and small amounts of O $p\pi$ electrons. All the other d orbitals are shifted by about 4.5 eV to lower energy. The 2 majority spin d orbitals at 0.62 a.u. have a large 22% O $p\pi$ population with much smaller C p populations. Both the on-top and bridging CO

structures maintain a minority spin feature at low binding energy. However, in the bridging structure there is reduced Fe to CO back donation and the intensity of the minority spin peak should be lowered relative to that found in the other structures. When the CO coverage on the Fe(100) surface is increased, no reduction in the minority spin peak intensity is observed, suggesting that the CO on-top structure must be being formed at higher coverage.

In summary these very simple cluster models using UHF calculations along with the Constrained Space Orbital Variation analysis show that strong Fe to CO π^* back donation effects are taking place in the tilted CO adsorption state on Fe(100). The UHF calculations on the tilted CO structure also allow correlation between Fe d back donation to CO π^* orbitals and the spin dependent features recently observed in spin polarized photoemission experiments. The Fe₂CO calculations are also consistent with the two photoemission peaks at 8.0 and 12.0 eV binding energy observed at low CO surface coverage, although the calculations do suggest an alternative assignment of the CO levels. The relatively large back donation effect computed for the on-top structure FeCO(C_{4v}) along with the continuation of spin polarized effects suggest this structure correlates with the CO(α_2) state. It is worth noting that the Fe(100) surface is sufficiently open to allow the on-top CO to interact with a subsurface Fe at the 4-fold site below the top surface Fe

atoms. Finally, the bridging CO structure might correlate with the $\text{CO}(\alpha_1)$ state although the evidence from the calculations for this is weak.

Geometry Optimization Calculations

In the geometry optimizations, the CO position was varied while the Fe-Fe distance was held fixed. The calculations were done using the pseudopotential and full basis sets, but the pseudopotential basis set was used first concerning the Fe_2CO clusters. This was necessary due to problems with computational time and SCF convergence. Reducing the basis size reduced the amount of computational time greatly. Also, the pseudopotential results were used to start the full basis Fe_2CO cluster calculations.

During the geometry optimizations both the cluster point group and the symmetry of the atomic orbitals were maintained. The $\text{FeCO}(\text{C}_{4v})$ cluster was taken to lie along the z axis. The Fe_2 in the $\text{Fe}_2\text{CO}(\text{C}_{2v})$ cluster lies on the y axis, and the CO lies on the z axis, because the C_{2v} principle axis is the z axis. The Fe_2 in the $\text{Fe}_2\text{CO}(\text{C}_s)$ cluster lies on the z axis, and the CO is parallel to the x axis. The irreducible representation, for which each cluster atomic orbital belongs, is listed in table 5.5. The spin multiplicity of each cluster was kept the same as in our earlier study.

Table 5.5

Irreducible Representations Spanned by the Atomic Orbitals
used in the Fe_xCO Clusters

$\text{FeCO}(\text{C}_{4v})$

Molecule	Orbital	Irreducible Representation
Fe	$s\sigma, p\sigma_z, d\sigma_z^2$	a_1
	$d\delta(x^2-y^2)$	b_1
	$d\delta(xy)$	b_2
	$d\pi(xz), d\pi(yz)$	e
CO	$s\sigma, p\sigma_z$	a_1
	$p\pi_x, p\pi_y$	e

$\text{Fe}_2\text{CO}(\text{C}_{2v})$

Molecule	Orbital	Irreducible Representation
Fe ₂	$s\sigma, p\sigma_y, p\pi_z, d\sigma(y^2)$	a_1
	$d\pi(yz), d\delta^*(x^2-z^2)$	a_1
	$p\pi_x^*, d\delta^*(xz),$	a_2
	$d\pi^*(xy)$	a_2
	$p\pi_x, d\delta(xz), d\pi(xy)$	b_1
	$s\sigma^*, p\sigma_y^*, p\pi_z^*,$	b_2
	$d\sigma^*(y^2), d\pi^*(yz),$	b_2
	$d\delta(x^2-z^2)$	b_2

Table 5.5 (continued)
 Irreducible Representations Spanned by the Atomic Orbitals
 used in the Fe_xCO Clusters

$\text{Fe}_2\text{CO}(\text{C}_{2v})$

Molecule	Orbital	Irreducible Representation
CO	$s\sigma, p\sigma_z$	a_1
	$p\pi_x$	b_1
	$p\pi_y$	b_2

$\text{Fe}_2\text{CO}(\text{C}_s)$

Molecule	Orbital	Irreducible Representation
Fe ₂	$s\sigma, p\sigma_z, p\pi_x, p\pi_y$	a'
	$d\sigma(z^2), d\pi(xz),$	a'
	$d\pi(yz), d\delta(xy),$	a'
	$d\delta(x^2-y^2)$	a'
	$s\sigma^*, p\sigma_z^*, p\pi_x^*, p\pi_y^*$	a''
	$d\sigma^*(z^2), d\pi^*(xz),$	a''
	$d\pi^*(yz), d\delta^*(xy),$	a''
	$d\delta^*(x^2-y^2)$	a''
CO	$s\sigma, p\sigma_x, p\pi_y$	a'
	$p\pi_z$	a''

CO (C_{4v})

Free CO was optimized in C_{4v} symmetry, and the results are listed in table 5.6. The optimized C-O bond length is 1.138 Å, and the corresponding stretching frequency is 2266.6 cm⁻¹. Both of these quantities over estimate the experimental values for CO, where the C-O bond length is 1.128 Å with a stretching frequency of 2143 cm⁻¹.²⁴ However, the results are very good considering electron correlation has not been included.

Table 5.6
Optimized CO(C_{4v})
Full Basis Set

Energy = -112.685070 a.u.

C - O bond length = 1.138 Å

ν = 2266.6 cm⁻¹

Charges:

C = +0.23

O = -0.23

FeCO (C_{4v})

As found in previous studies the $^5\Sigma^-$ state with the Fe configuration $d\sigma^1d\pi^4d\delta^24s^1$ is best suited for FeCO(C_{4v}).^{33,119,127} Convergence for this system can be achieved by following these steps. First, start the calculation with a charge of +2 and a multiplicity of 7. This will remove the d electrons from the spin minority space and give all the d orbitals equal energy weight. It is not important whether this calculation converges, but rather that it provides a good starting set of vectors for the next calculation. By rearranging the vectors from the charged calculation into the $^5\Sigma^-$ configuration, one only needs to use symmetry blocking of the Fock matrix and convergence is readily achieved.

The results of the geometry optimization for the pseudopotential and full basis sets are listed in table 5.7. The pseudopotential calculation produced an optimized Fe-C distance of 2.083 Å and a C-O distance of 1.140 Å. The stretching frequency is calculated to be 2180 cm⁻¹. The full basis set produced an Fe-C distance of 1.887 Å and a C-O length of 1.162 Å. The vibrational stretching frequency is calculated to be 1992.2 cm⁻¹.

The optimized Fe-C distance from the full basis set is very close to the experimental distance of 1.84 Å in carbonyl complexes.²⁴ The results for the full basis set match other

Table 5.7
 Geometry Optimization Results for FeCO(C_{4v})

State	<u>full basis</u>		<u>pseudo.</u>
	FeCO(⁵ Σ ⁻)	FeCO(⁵ Π)	FeCO(⁵ Σ ⁻)
Energy (a.u.)	-1374.971437	-1374.921484	-134.129671
Distances (Å)			
Fe-C	1.877	2.034	2.083
C-O	1.162	1.183	1.140
Charges			
Fe	0.20	0.32	+0.04
C	0.01	-0.10	+0.16
O	-0.22	-0.22	-0.19
<S ² >	6.68	6.94	6.16
Frequency			
ν (cm ⁻¹)	1992.2	2103.9	2180.3
Binding			
Energies (eV)			
Fe(⁵ D) ^a	-1.84	-3.20	-1.77
Fe(⁵ F) ^b	+0.45	+0.15	+0.12

a) B.E. = E(Fe(⁵D)) + E(CO) - E(FeCO)

b) B.E. = E(Fe(⁵F)) + E(CO) - E(FeCO)

calculations performed on $\text{FeCO}(^5\Sigma^-)$. Using CASSCF calculations, Bauschlicher et al. determined the Fe-C equilibrium bond distance to be 1.91 Å and the C-O bond length to be 1.16 Å.³³ Dauodi et al. also determined the Fe-C distance to be 1.90 Å while keeping the C-O distance fixed at 1.15 Å using perturbation theory.¹²⁷ Even with the neglect of electron correlation the UHF calculations have produced very good optimized geometries. The C-O stretching frequency of the full basis calculation is also in good agreement with the observed frequencies. For FeCO the observed stretching frequency is 1898 cm^{-1} ,¹²⁸ and for the $\text{CO}(\alpha_1)$ and $\text{CO}(\alpha_2)$ states, 2070 and 2010 cm^{-1} , respectively. Dauodi et al. have calculated a stretching frequency of 1986 cm^{-1} , which is very close to our calculated value.¹²⁷ If we correct for the overestimation of the stretching frequency of free CO, then our calculated value becomes 1869 cm^{-1} , which is in better agreement with the observed frequency for FeCO.

Clearly, the pseudopotential does not compare as well to other calculations due to a lack of backdonation into the CO. This is seen from the smaller charge on the Fe and the shorter C-O bond length. The longer Fe-C distance may indicate that the back donation is a larger factor in the Fe-C distance versus the σ donation from the CO.

Both calculations are unbound with respect to the $\text{Fe}(^5\text{D})$ ground state by approximately 1.8 eV. However, both calculations are bound relative to the $\text{Fe}(^5\text{F})$ state. The CO

is bound by 0.12 eV to the Fe in the pseudopotential calculation, and the CO is bound to the Fe by 0.45 eV in the full basis set calculation. The binding energy for the full basis set is expected to be higher, because the Fe-C distance is shorter, and the backdonation is more significant. Bauschlicher et al.³³ calculate a binding energy of 0.98 eV for $\text{FeCO}(^5\Sigma^-)$, which reproduces the experimental value of 0.9 eV.¹²⁹ Dauodi et al. calculate a binding energy of 0.58 eV, but they also conclude $\text{FeCO}(^3\Sigma^-)$ is lower in energy than $\text{FeCO}(^5\Sigma^-)$, which contradicts other authors.^{33,126} As expected the binding energy of the UHF calculation does not compare well with the correlated calculations. Yet, The binding energy of 0.45 eV is in excellent agreement with the activation energy, 0.55 eV, for desorption of the $\text{CO}(\alpha_1)$ state.

In addition to the geometry optimization, we also wanted to do a CSOV study on the new geometry in order to determine any change in the bonding interactions. Also, the differences in the optimization results between the pseudopotential and the full basis set are enlightened by the CSOV analysis. The steps for the CSOV study are the same as listed in figure 5.3. The results for the CSOV analysis for the pseudopotential and the full basis set are given in tables 5.8 and 5.9, respectively.

Table 5.8
 CSOV Study for FeCO(C_{4v}) ⁵Σ⁻ State
 Pseudopotential Basis Set

Geometry:

Fe - C distance = 2.083 Å

C - O distance = 1.140 Å

Reference Energy:

E(Fe) + E(CO) = -134.125371 a.u.

Step	Estep	ΔEstep	Charges			<S ² >
			Fe	C	O	
0	-1.59		0.00	+0.23	-0.23	6.00
1	-1.00	0.59	0.00	+0.23	-0.23	6.02
2	-0.96	0.04	-0.01	+0.24	-0.23	6.02
3	-0.44	0.52	+0.15	+0.11	-0.26	6.11
4	-0.36	0.09	+0.13	+0.07	-0.19	6.12
5	+0.09	0.45	+0.02	+0.20	-0.22	6.11
6	+0.11	0.02	+0.01	+0.18	-0.19	6.12
SCF	+0.12	0.01	+0.04	+0.16	-0.19	6.16

Energy values are in eV

Charges and spin values are in atomic units

Table 5.9
 CSOV Study for FeCO(C_{4v}) $5\Sigma^-$ State
 Full Basis Set

Geometry:

Fe - C distance = 1.887 Å

C - O distance = 1.162 Å

Reference Energy:

E(Fe) + E(CO) = -1374.953627 a.u.

Step	Estep	ΔE_{step}	Charges			$\langle s^2 \rangle$
			Fe	C	O	
0	-2.29		0.00	0.26	-0.26	6.01
1	-1.40	0.89	0.00	0.26	-0.26	6.03
2	-1.37	0.03	0.02	0.24	-0.26	6.04
3	-0.27	1.10	0.29	0.03	-0.33	6.32
4	-0.18	0.09	0.38	-0.14	-0.24	6.33
5	+0.28	0.46	0.12	0.12	-0.24	6.33
6	+0.33	0.05	0.12	0.08	-0.21	6.34
SCF	+0.48	0.15	0.20	0.01	-0.22	6.68
2'		1.07				

Energy values are in eV

Charges and spin values are in atomic units

First, the full basis set CSOV study shows similar trends to those previously reported. There are slight variations, which result from the slight change in geometry. For the optimized geometry the frozen orbital energy has been reduced by 0.14 eV, and the amount of π backdonation has been reduced by 0.15 eV. This is due to the slightly longer Fe-C distance of 1.887 Å versus 1.84 Å in the earlier study. In fact, this was shown to be true by additional studies at longer Fe-C distances.

The pseudopotential CSOV results are significantly different. The frozen orbital step is less repulsive by 0.70 eV, and the ΔE_{step} in the first step is lower by 0.30 eV. This is due no doubt to the longer Fe-C distance causing less repulsion and perturbation of the Fe. Even more interesting results are in step 3 and step 5. The amount of π backdonation is less by 0.58 eV, but the amount of σ donation from the CO is essentially the same. This indicates that the amount of π backdonation is directly influenced by the Fe-C distance. Furthermore, because the pseudopotential has replaced the core electrons of the Fe, it suggests a large part of the π backdonation comes from the core electrons. This can be tested using the CSOV technique. If we place an additional step in the full basis set CSOV study, 2', where the valence $d\pi$ orbitals of the Fe are allowed to mix with the CO full virtual space, this will determine the amount of π backdonation from the $d\pi$ orbitals. The change in energy from

2' to 3 will measure any contribution from the core electrons. As one can see in table 5.9, ΔE_{step} at step 2' of 1.07 eV accounts for most of the π backdonation, which is 1.10 eV. Therefore, the $d\pi$ orbitals are still the major contributors to the backdonation.

Because transition metals have a number of low lying states which can contribute to chemisorption, a singles and doubles CI calculation with the full basis set was performed to determine the configurations of the low lying states of FeCO. The reference determinant was FeCO($^5\Sigma^-$) at the optimized distances of 1.887 Å for Fe-C and 1.162 Å for C-O. Only the valence space was included in the CI calculation. The results for the first 9 states of the CI calculation are listed in table 5.10.

The C.I. results suggested the following 5 Fe configurations should be examined.

1. $d\sigma^1 d\delta^2 d\delta^1 d\pi^2 d\pi^1 4s\sigma^1$
2. $d\sigma^2 d\delta^2 d\delta^1 d\pi^1 d\pi^1 4s\sigma^1$
3. $d\sigma^1 d\delta^2 d\delta^1 d\pi^1 d\pi^1 4s\sigma^2$
4. $d\sigma^2 d\delta^1 d\delta^1 d\pi^2 d\pi^1 4s\sigma^1$
5. $d\sigma^1 d\delta^1 d\delta^1 d\pi^2 d\pi^1 4s\sigma^2$

All of these states were geometry optimized in order to determine if CO is bound. All of these configurations have broken axial symmetry; therefore, Fe configurations of

Table 5.10
Singles and Doubles CI calculation for FeCO($^5\Sigma^-$)

<u>State</u>	<u>Fe configuration</u>	Major	
		<u>Coefficients</u>	<u>Energy (a.u.)</u>
1	$d\sigma^1d\delta^1d\delta^1d\pi^2d\pi^24s\sigma^1$	0.886	-1374.998046
2	$d\sigma^1d\delta^2d\delta^1d\pi^2d\pi^14s\sigma^1$	0.758	-1374.986105
3	$d\sigma^1d\delta^1d\delta^2d\pi^2d\pi^14s\sigma^1$	0.781	-1374.985714
4	$d\sigma^1d\delta^2d\delta^1d\pi^1d\pi^24s\sigma^1$	0.767	-1374.984950
5	$d\sigma^1d\delta^1d\delta^2d\pi^1d\pi^24s\sigma^1$	0.717	-1374.984442
6	$d\sigma^2d\delta^2d\delta^1d\pi^1d\pi^14s\sigma^1$	0.711	-1374.963918
	$d\sigma^1d\delta^2d\delta^1d\pi^1d\pi^14s\sigma^2$	0.699	
7	$d\sigma^2d\delta^1d\delta^2d\pi^1d\pi^14s\sigma^1$	0.711	-1374.963913
	$d\sigma^1d\delta^1d\delta^2d\pi^1d\pi^14s\sigma^2$	0.620	
8	$d\sigma^2d\delta^1d\delta^1d\pi^2d\pi^14s\sigma^1$	0.513	-1374.958085
	$d\sigma^1d\delta^1d\delta^1d\pi^2d\pi^14s\sigma^2$	0.371	
9	$d\sigma^2d\delta^1d\delta^1d\pi^1d\pi^24s\sigma^1$	0.512	-1374.957209
	$d\sigma^1d\delta^1d\delta^1d\pi^1d\pi^24s\sigma^2$	0.378	

$d\sigma^2d\delta^1d\delta^1d\pi^1d\pi^14s\sigma^2$ and $d\sigma^1d\delta^2d\delta^2d\pi^1d\pi^14s\sigma^1$ were also attempted. To prevent variational collapse during the calculation, symmetry blocking of the Fock matrix must be used to preserve the Fe configuration. All of the states were unbound, except the $d\sigma^2d\delta^1d\delta^1d\pi^2d\pi^14s\sigma^1$ configuration $\text{FeCO}(^5\Pi)$ state. However, this state changed its d orbital occupancy, where a $4p\pi$ orbital replaced the $d\pi$ orbital in the spin minority space. Now the Fe configuration is $d\sigma^2d\delta^1d\delta^1d\pi^24s\sigma^14p\pi^1$.

The results of the $\text{FeCO}(^5\Pi)$ geometry optimization are listed in table 5.7. The Fe-C distance is 2.034 Å, which is longer than the $\text{FeCO}(^5\Sigma^-)$, but the CO bond length of 1.183 Å is also longer. The longer Fe-C distance would indicate less backdonation from the Fe, while the longer C-O bond length would indicate more backdonation from the Fe. The charge on Fe is higher by 0.12 than the $\text{FeCO}(^5\Sigma^-)$ state, but the vibrational stretching frequency of 2103.9 cm^{-1} is higher indicating there is less backdonation into the $2\pi^*$ orbital. The stretching frequency is anomalous to the trends in the Fe_xCO clusters, in which a longer C-O bond length always translated into a lower frequency. The CO is bound by 0.15 eV with respect to the $\text{Fe}(^5F)$ energy, which is similar to the pseudopotential calculation with a similar Fe-C distance. If we analyze the HOMO orbital in the β space, it is comprised of Fe $4p\pi$ and CO $2\pi^*$ character. Now the $2\pi^*$ orbital has entered the occupied space. This accounts for the greater

charge transfer from the Fe and the longer bond length of the CO. The Fe-C distance is longer, because the $d\sigma(z^2)$ orbital is in the β space repelling the lone pair 5σ on the CO. The larger stretching frequency is still an enigma. A CSOV study on the $\text{FeCO}(^5\Pi)$ state should provide information regarding the properties, but there is no guarantee against variational collapse to the $\text{FeCO}(^5\Sigma^-)$ state during the execution. It is also interesting to note that the occupation of the $4p\pi$ orbital is consistent with the Avouris et al. findings for FeCO^- .⁴² They state hybridization of the $4p\pi$ orbital and the CO $2\pi^*$ orbital is important to the complete binding picture of metal carbonyls. This would seem to be the case for the bound $\text{FeCO}(C_{4v})$ geometries.

Fe_2CO (C_{2v})

Since we started with the pseudopotential, the vectors from the extended Huckel technique can be used to obtain initial guess vectors. Charge build up was also employed, and we used a charge of +2 at a multiplicity of 9. The initial vectors obtained were used to do a normal calculation with a charge of 0 at a multiplicity of 7. The charge build-up vectors produced a far lower energy than that obtained from the extended Huckel starting guess by 8.51 eV. Therefore, the extended Huckel guess was shown to be an unreliable starting point in these calculations. Using the charge build-up

vectors, corresponding to a 7B_1 electronic state, the CO bond was lengthened to 1.180 Å in the geometry optimization, and the energy dropped further by 0.19 eV. The final results of the geometry optimization are listed in table 5.11.

In order to perform a CSOV study on the 7B_1 state the CO was pulled away from the Fe₂ to derive the appropriate Fe₂ configuration of $d\delta^2d\delta^*2d\pi^2d\pi^*2d\sigma^2d\sigma^*24s\sigma^24s\sigma^*14p\pi_x^1$ with $4s\sigma^*1$ and $4p\pi_x^1$ being in the β space. However, when the CSOV analysis was executed this Fe₂ configuration produced a 7A_2 electronic state which was 0.39 eV lower in energy at the 7B_1 optimized geometry. This 7A_2 state was optimized to produce a final energy 0.77 eV lower than found for the 7B_1 state. Interestingly, the spin minority electrons for the 7B_1 and 7A_2 states maintain the same symmetry, while the spin majority electrons have differing symmetry. The electronic configurations differ by an a_1 orbital being excited to a b_2 orbital in the 7B_1 state. The results are listed in table 5.11.

The 2.445 Å Fe-C distance in the 7A_2 state is much greater than the 2.151 Å Fe-C distance in the 7B_1 state. The experimental Fe-C distance in Fe₂(CO)₉ is 2.02 Å.²⁴ This would seem to favor the 7B_1 state, but the C-O bond length of the 7A_2 state agrees better with experimental values. The C-O bond length in carbonyl complexes at the bridging site is approximately 1.15 Å,²⁴ and the carbonyl stretching frequency for Fe₂(CO)₉ is 1828 cm⁻¹.¹³⁰ The 7A_2 optimized C-O bond

Table 5.11
 Geometry Optimization Results for Fe₂CO(C_{2v})
 Pseudopotential Basis Set

State	Fe ₂ CO(⁷ B ₁)	Fe ₂ CO(⁷ A ₂)
Energy (a.u.)	-155.598693	-155.613028
Distances (Å)		
Fe-C	2.151	2.445
C-O	1.214	1.186
Charges		
Fe	+0.33	+0.28
C	-0.40	-0.32
O	-0.25	-0.24
<S ² >	14.32	14.17
Frequency		
v (cm ⁻¹)	1379.8	1797.7
Binding		
Energies (eV)		
Fe ^a	-2.89	-2.13
Fe ₂ ^b	+0.42	+1.18

a) B.E. = 2*E(Fe(⁵D)) + E(CO) - E(Fe₂CO)

b) B.E. = E(Fe₂) + E(CO) - E(Fe₂CO)

length is 1.186 Å compared to 1.214 Å for 7B_1 . The frequency for the 7A_2 state is 1797.7 cm^{-1} versus 1379.8 cm^{-1} , which is quite low. 1379.8 cm^{-1} is approaching the value of the experimental value for the tilted $\text{CO}(\alpha_3)$ structure. Both states involve interaction with the $d\delta^2d\delta^*2d\pi^2d\pi^*2d\sigma^2d\sigma^*24\sigma_s24s\sigma^*14p\pi_x^1$ Fe_2 configuration. The 7B_1 state is bound by 0.42 eV, which is close to the $\text{FeCO}(C_{4v})$ binding energy. The 7A_2 state is bound by 1.18 eV, which is substantially greater. Yet, both states are unbound with respect to the $\text{Fe}({}^5D)$ ground state by more than 2.0 eV.

Because this geometry did yield such an interesting Fe_2 configuration and a lower energy, we performed a CSOV study on this system. Since the Fe_2 configuration is very different from the Fe_2 configuration used in our earlier study, the steps in the CSOV study for this cluster have been modified to enable additional insight into the CO bonding. A summary of the steps are listed in figure 5.5. Step 0 is still the frozen orbital calculation, and Step 1 allows the Fe to relax in the field of the CO. Step 2 allows the Fe_2 to mix with the CO σ virtual orbitals. To measure the π backdonation, step 3 of the previous study has been split into steps 3 and 4, because the CO p_x and p_y orbitals belong to different symmetry types: b_1 and b_2 , respectively. Step 3 allows the Fe to mix with the CO π virtual orbitals of b_1 symmetry, and Step 4 is the full virtual space. It is important to note that the orbitals of b_1 symmetry are perpendicular to the Fe_2

Figure 5.5
CSOV Steps for Fe₂CO(C_{2v})

- Step 0 : Frozen Orbital
- Step 1 : Fe orbitals vary
- Step 2 : Fe mixes with CO a₁ virtual
- Step 3 : Fe mixes with CO a₁, b₁ virtual
- Step 4 : Fe mixes with CO full virtual
- Step 5 : CO orbitals vary
- Step 6 : CO mixes with Fe a₁, a₂ virtual
- Step 7 : CO mixes with Fe full virtual
- Step 8 : SCF energy

axis. Likewise, the orbitals of b_2 symmetry are parallel to the Fe_2 axis. Step 5 allows the CO to vary in the field of the Fe_2 . Steps 6 measures the σ donation from the CO by letting CO to mix with the Fe virtual orbitals of a_1 and a_2 symmetry. Step 7 is the full Fe virtual space, which measures any π donation from the CO. Step 8 is the final SCF energy. The results of the CSOV study are listed in table 5.12.

In the frozen orbital step the repulsive interaction is far less than for FeCO. However, this reduction matches the longer Fe-C distance for this cluster. The repulsion is also smaller, by 4.56 eV, than the repulsion calculated in the previous full basis Fe_2CO study. Even though, the previous study used a full basis set, inadequacy of the pseudopotential is not the factor. Most likely this is a result of a better starting Fe_2 configuration.

Relaxation of the Fe orbitals is observed in the first step, and it is a significant drop in energy of 0.68 eV. The change in energy is not as large as reported in the full basis study, but once again this may be due to a better starting Fe_2 configuration. Based on the Mulliken population analysis, the change in energy is a result of the Fe 4s orbital undergoing sp hybridization, and the $d\delta(x^2-z^2)$ polarized into more x^2 character. In addition, the $d\sigma(y^2)$ polarized into more z^2 character in both the spin majority and minority spaces. The $4p\pi_x$ orbital polarized slightly to the $d\pi(xy)$ orbitals in the spin minority space. In the second

Table 5.12
 CSOV Study for $\text{Fe}_2\text{CO}(\text{C}_{2v}) \ ^7\text{A}_2$
 Pseudopotential Basis Set

Geometry:

Fe - C distance = 2.445 Å

C - O distance = 1.186 Å

Reference Energy:

$E(\text{Fe}_2) + E(\text{CO}) = -155.578531 \text{ a.u.}$

Step	Estep	ΔEstep	Charges			$\langle s^2 \rangle$
			Fe	C	O	
0	-1.51		0.00	0.28	-0.28	14.11
1	-0.83	0.68	0.00	0.29	-0.29	14.12
2	-0.74	0.09	-0.02	0.31	-0.28	14.12
3	+0.33	1.07	0.26	-0.14	-0.38	14.12
4	+0.46	0.13	0.25	-0.13	-0.38	14.10
5	+0.57	0.11	0.28	-0.24	-0.32	14.11
6	+1.03	0.46	0.19	-0.08	-0.30	14.11
7	+1.26	0.23	0.27	-0.28	-0.25	14.15
SCF	+1.31	0.05	0.28	-0.32	-0.24	14.17

Energy values are in eV

Charges and spin values are in atomic units

step, no substantial change is observed. This is also true in the other CSOV studies, and it is consistent with the Fe not σ donating into the CO virtual orbitals.

The third step was found to be the major interaction. The change in energy, 1.02 eV, is the largest ΔE_{step} in the study, and the charge transfer is enormous. The charge on each Fe atom changed by +0.28, the charge on the C changed by -0.45, and the charge on the O changed by -0.10. According to the Mulliken population this is a result of the CO π_x^* entering the occupied space in the spin minority space replacing the Fe $4p\pi_x$ orbital. The HOMO of the spin minority space is comprised mostly of CO π_x^* and Fe $4p\pi_x$ character. The fourth step shows a small change in energy, and more importantly, the charge on the Fe atoms has not changed. This indicates that the Fe₂ does not back donate into the CO π_y^* orbitals. This is remarkable, since the CO π_y orbitals are in the same plane as the Fe₂. Therefore, one would predict a significant interaction between the CO π_y orbitals and the Fe orbitals. The spin minority HOMO will be designated as the ($4p\pi_x + \text{CO } \pi_x^*$) molecular orbital.

In the fifth step, the change in energy is not large, nor has the charge rearranged very much. In the sixth step, the CO σ donation is a more substantial interaction than in our previous study. The change in energy is 0.46 eV compared to 0.20 eV in the earlier calculation. The charge on each Fe atom changed by -0.09, the charge on the C changed by +0.16,

and the charge on the O changed by +0.02. As observed earlier the donation came primarily from the C atom. The Mulliken population analysis shows both the spin majority and minority electrons donate into the Fe virtual orbitals.

In the seventh step there is a significant change in energy, but the charge on each Fe changed by +0.08, thereby indicating a loss of electrons from the Fe₂. This resulted from the (4p π_x + CO π_x^*) molecular orbital polarizing to give more electrons on the C atom. Indeed the charge on the C changed by -0.20 and is now more negative by charge than the O. This has not been observed previously in other studies, and it may indicate that the σ lone pair is important in stabilizing this structure. Small changes are observed when the final SCF energy is achieved.

The $\langle S^2 \rangle$ values varied little during the CSOV process. This differs than the earlier study, where the $\langle S^2 \rangle$ values changed substantially. However, a pure spin state would yield an $\langle S^2 \rangle$ value of 12.0, which is considerably lower than 14.17. The higher spin is due to contamination from higher spins. If we analyze the starting configuration of $d\delta^2 d\delta^{*2} d\pi^2 d\pi^{*2} d\sigma^2 d\sigma^{*2} 4s^2 4s\sigma^{*1} 4p\pi_x^1$, this could easily be converted to the Fe₂ configuration of $d\delta^2 d\delta^{*2} d\pi^2 d\pi^{*2} d\sigma^2 d\sigma^{*2} 4s^2 4s\sigma^{*2}$ with a multiplicity of 9, which is the same configuration as two ground state Fe(⁵D) configurations. Therefore, calculations of multiplicity 9 should be performed.

CSOV analysis on the bridging structure obtain with the pseudopotential basis set has revealed several unexpected bonding interactions. The CO π_x^* orbital has collapsed into the occupied space of the Fe₂CO system. This accounts for the large charge of -0.56 on the CO molecule. The mixing of the CO π_x^* with the Fe₂ 4p π_x orbitals is similar to the findings of Avouris et al. in their FeCO⁻ calculations.⁴² Most interestingly is that the CO π^* orbitals perpendicular to the Fe₂ axis are the ones strongly involved in the π backdonation.

For the full basis calculation, the charge build-up technique was used to reach convergence. The Fe-C distance was put at 2.05 Å, and the CO bond length was put at 1.15 Å, which were used in the previous full basis study. A charge of +20 at a multiplicity of 1 was used first, and then the molecular orbitals were used for the normal calculation of a charge of 0 at a multiplicity of 7. Because the partial geometry optimization was not available at the time of these calculations, a number single of points were calculated in order to estimate a minimum energy for the CO position. The CO was placed at Fe-C distances of 1.80, 2.30, and 2.50 Å. These points were used to curve fit a quadratic function to determine an estimate for the optimum Fe-C distance. This resulted in a Fe-C distance of 2.26 Å, and this was the starting point for the geometry optimization. Also, symmetry blocking of the Fock matrix was employed in order to prevent

Table 5.13
 Geometry Optimization Results for Fe₂CO(C_{2v})
 Full Basis Set

State	Fe ₂ CO(⁷ B ₁)	Fe ₂ CO(⁷ A ₂)
Energy (a.u.)	-2637.315812	-2637.326921
Distances (Å)		
Fe-C	2.083	2.416
C-O	1.245	1.184
Charges		
Fe	+0.36	+0.27
C	-0.48	-0.33
O	-0.25	-0.22
<S ² >	14.65	14.27
frequency		
ν (cm ⁻¹)	1273.8	1767.0
Binding		
energies (eV)		
Fe ^a	-2.10	-1.80
Fe ₂ ^b	+1.13	+1.44

a) B.E. = 2*E(Fe(⁵D)) + E(CO) - E(Fe₂CO)

b) B.E. = E(Fe₂) + E(CO) - E(Fe₂CO)

any convergence problems during the optimization. The results are listed in Table 5.13.

The symmetry of the full basis set calculation is 7B_1 as it is for the excited pseudopotential Fe_2CO . The Fe-C distance contracted to 2.083 Å, which in turn caused more backdonation into the CO. The C-O bond length increased to 1.245 Å. This also resulted in a lower stretching frequency of 1273.8 cm^{-1} . The final charges on the Fe_2CO geometry also compare very well to the pseudopotential case, except the Fe is slightly more positive in the full basis calculation due to the additional backdonation. The binding energy for the full basis set calculation has also improved. The 7B_1 state is still unbound by -2.10 eV with respect to the $Fe({}^5D)$ ground state, but it has a higher binding energy of 0.76 eV with respect to the $d\delta^2d\delta^*2d\pi^2d\pi^*2d\sigma^2d\sigma^*24\sigma_s24s\sigma^*14p\pi_x^1 Fe_2$ configuration. These trends were also seen in the $FeCO(C_{4v})$ pseudopotential and full basis set calculations.

Since the 7A_2 state was at a lower energy when the pseudopotential basis set was used, we needed to construct the 7A_2 state in the full basis set. This was done by superimposing the $d\delta^2d\delta^*2d\pi^2d\pi^*2d\sigma^2d\sigma^*24\sigma_s24s\sigma^*14p\pi_x^1 Fe_2$ configuration with CO. The state was optimized and the results are listed in table 5.13. The same trends between the pseudopotential basis set and the full basis set continue, except the C-O bond length has contracted instead of expanding. The charge on the Fe is slightly less compared to

the pseudopotential basis indicating less backdonation and, therefore, a shorter C-O bond. The CO stretching frequency, however, is lower, but this is most likely due to errors in the curve fittings. The binding energy has increased by 0.26 eV with respect to the $d\delta^2d\delta^*2d\pi^2d\pi^*2d\sigma^2d\sigma^*24s24s\sigma^*14p\pi_x^1$ Fe₂ configuration, but it is still unbound with respect to the Fe(⁵D) ground state. The energy separation between the ⁷B₁ state and the ⁷A₂ state has lowered from 0.77 eV in the pseudopotential calculations to 0.30 eV in the full basis calculations.

A CSOV study was conducted on the ⁷A₂ state with the full basis set, and the results are listed in table 5.14. The full basis set study essentially followed the same trends as the pseudopotential study, except in step 7 and the final SCF step. ΔE_{step} in step 7 is 0.10 eV for the full basis set compared to 0.23 eV for the pseudopotential study. This results from the less charge rearrange occurring in step 7 regarding the full basis set. The small change in energy demonstrates that the CO does not π donate to the Fe₂ in the bridging structure. The larger ΔE_{step} in the final SCF step for the full basis set has been a trend observed in all the CSOV studies between the pseudopotential and full basis set. The correlation between the π backdonation and the σ donation interaction energies is represented more accurately by the full basis set.

Table 5.14
 CSOV Study for $\text{Fe}_2\text{CO}(\text{C}_{2v}) \ ^7\text{A}_2$
 Full Basis Set

Geometry:

Fe - C distance = 2.416 Å

C - O distance = 1.184 Å

Reference Energy:

$E(\text{Fe}_2) + E(\text{CO}) = -2637.273159 \text{ a.u.}$

Step	Estep	ΔEstep	Charges			$\langle s^2 \rangle$
			Fe	C	O	
0	-1.43		0.00	+0.28	-0.28	14.15
1	-0.81	0.62	0.00	+0.29	-0.29	14.23
2	-0.77	0.04	-0.01	+0.30	-0.28	14.26
3	+0.12	0.89	+0.21	-0.06	-0.36	14.27
4	+0.27	0.15	+0.21	-0.04	-0.37	14.24
5	+0.40	0.13	+0.25	-0.20	-0.29	14.25
6	+0.77	0.37	+0.16	-0.03	-0.28	14.25
7	+0.87	0.10	+0.15	-0.09	-0.21	14.27
SCF	+1.46	0.59	+0.27	-0.33	-0.22	14.27

Energy values are in eV

Charges and spin values are in atomic units

In comparison to our earlier study done on $\text{Fe}_2\text{CO}(\text{C}_{2v})$, the CSOV study is significantly improved. The frozen orbital energy is much less repulsive, and E_{step} in step 3 falls below the reference energy. In the earlier study the SCF E_{step} is above the reference energy by 2.87 eV. This could be due to the longer Fe-C distance of the ${}^7\text{A}_2$ state, but most likely this is due to a better Fe₂ starting configuration of $d\delta^2 d\delta^*2 d\pi^2 d\pi^*2 d\sigma^2 d\sigma^*2 4s^2 4s\sigma^*1 4p\pi_x^1$, which is significantly different than the Fe₂ starting configuration of $d\delta^2 d\delta^*2 d\pi^4 d\pi^*4 d\sigma^2 d\sigma^*2 4s^2$ used earlier.

$\text{Fe}_2\text{CO} (\text{C}_s)$

Because the standard SCF convergence techniques did not work for the $\text{Fe}_2\text{CO} (\text{C}_s)$ geometry, a new approach had to be developed. We started with the optimized ${}^7\text{B}_1 \text{Fe}_2\text{CO}(\text{C}_{2v})$ geometry, where the Fe-C distance is 2.151 Å, and the CO distance is 1.210 Å. When this work was started we had not started yet discovered the ${}^7\text{A}_2$ state. From the C_{2v} geometry the CO was tilted into the C_s symmetry by moving the O by 0.10 Å along the x axis. The C was kept fixed at its position, and the C-O distance was held fixed at 1.210 Å. This was attempted in the opinion that the change in geometry would produce an electronic state for the C_s symmetry. As the CO was tilted the energy rose, indicating that the CO was still in the $\text{Fe}_2\text{CO}(\text{C}_{2v})$ potential well. In fact, any attempt

at optimizing the O with the C fixed produced the C_{2v} geometry regardless of the tilt angle of the CO. Consequently, after the CO was parallel with the x axis, we moved the CO across the Fe_2 axis along the x axis. However, as the CO was moved across the Fe_2 , the energy still increased. Finally, the O was held fixed in its position with the CO parallel to the x axis, and the C position was optimized. This produced a ${}^7A'$ electronic state with an extended CO bond length of 1.255 Å. Now, when the CO was moved across the x axis, additional optimizations of the C position produced a CO bond length of 1.399 Å. From this point, the CO was allowed to vary its position. These calculations demonstrate again the utility of the partial optimization technique.¹⁰¹ The results are listed in table 5.15.

Once again when the CO was removed from the Fe_2 , an Fe_2 configuration of $d\delta^2d\delta^*2d\pi^2d\pi^*2d\sigma^2d\sigma^*24s\sigma^24s\sigma^*14p\pi_x^1$ with $4s\sigma^*1$ and $4p\pi_x^1$ in the β space resulted. This is the same starting Fe_2 configuration as found with the $Fe_2CO(C_{2v})$ geometry. Likewise, when the CSOV study was executed, this Fe_2 configuration produced a lower energy state, ${}^7A''$, which was lower by 0.84 eV than the optimized ${}^7A'$ state. The ${}^7A''$ state was optimized, and the results are listed in Table 5.15. The states differ by exciting a spin majority A' orbital to a A'' orbital in the ${}^7A'$ state. The spin minority

Table 5.15
 Geometry Optimization Results for Fe₂CO(C_s)
 Pseudopotential Basis Set

State	Fe ₂ CO(⁷ A')	Fe ₂ CO(⁷ A'')
Energy (a.u.)	-155.555777	-155.587907
Distances (Å)		
Fe-C	2.264	2.367
Fe-O	2.073	2.047
C-O	1.449	1.465
Charges		
Fe	+0.52	+0.54
C	-0.23	-0.24
O	-0.81	-0.84
<S ² >	14.81	13.96
frequency		
v (cm ⁻¹)	864.4	806.8
Binding		
energies (eV)		
Fe ^a	-4.06	-3.19
Fe ₂ ^b	-0.75	+0.12

a) B.E. = 2*E(Fe(⁵D)) + E(CO) - E(Fe₂CO)

b) B.E. = E(Fe₂) + E(CO) - E(Fe₂CO)

electronic state is the same for both $\text{Fe}_2\text{CO}(\text{C}_s)$ states as was the case for $\text{Fe}_2\text{CO}(\text{C}_{2v})$.

Even though the bond length is quite long and the CO stretching frequency is very low, approximately 800 cm^{-1} for both states, the results are encouraging for comparison to the $\text{CO}(\alpha_3)$ state, which has a CO stretching frequency of 1210 cm^{-1} .⁵ If the geometries of the ${}^7\text{A}'$ and ${}^7\text{A}''$ state are extrapolated to an $\text{Fe}_5(\text{C}_{4v})$ cluster, where the C is put directly above the well Fe atom, we can estimate how well they compare to the experimentally observed geometry for the $\text{CO}(\alpha_3)$ state. For the ${}^7\text{A}'$ state the C would be 1.0 \AA above the surface, and the tilt angle of the CO is calculated to be 70.1° from the normal. The tilt angle is much larger than what is experimentally observed, but the values are promising for representing the tilted structure. For the ${}^7\text{A}''$ structure, the C is 1.2 \AA above the surface, and the tilt angle is 80.5° from the surface normal, which is even farther than the ${}^7\text{A}'$ structure. Both states may have a role in modelling the tilted CO geometry on the Fe surface.

The CSOV study was performed on the ${}^7\text{A}''$ geometry, and the results are listed in Table 5.16. The steps are the same as listed for $\text{Fe}_2\text{CO}(\text{C}_{2v})$ in figure 5.5, except for the symmetry of the orbitals. Step 2 allows the Fe to mix with the CO σ virtual orbitals, which have a' symmetry. Step 3 allows the CO to mix with the CO virtual π_y orbitals or a' symmetry. It is important to note that these orbitals are

Figure 5.6
CSOV Steps for $\text{Fe}_2\text{CO}(\text{C}_s)$

- Step 0 : frozen orbital
- Step 1 : Fe orbitals vary
- Step 2 : Fe mixes with CO A' σ virtual
- Step 3 : Fe mixes with CO A' π virtual
- Step 4 : Fe mixes with CO full virtual
- Step 5 : CO orbitals vary
- Step 6 : CO mixes with Fe A' virtual
- Step 7 : CO mixes with Fe full virtual
- Step 8 : SCF energy

Table 5.16
 CSOV Analysis for Fe₂CO (C_s) ⁷A"
 Pseudopotential Basis Set

Geometry:

Fe - C distance = 2.367 Å

Fe - O distance = 2.047 Å

C - O distance = 1.465 Å

Reference Energy:

E(Fe₂) + E(CO) = -155.454308

Step	E _{step}	ΔE _{step}	Charges			<S ² >
			Fe	C	O	
0	-6.44		0.00	+0.50	-0.50	14.11
1	-4.37	2.07	0.00	+0.51	-0.51	13.96
2	-4.18	0.19	-0.01	+0.50	-0.50	13.97
3	+0.04	4.22	+0.43	-0.23	-0.64	14.14
4	+0.21	0.17	+0.46	-0.27	-0.65	14.10
5	+1.01	0.80	+0.46	-0.11	-0.82	14.13
6	+2.23	1.22	+0.37	+0.06	-0.80	14.17
7	+2.87	0.64	+0.29	+0.17	-0.75	14.17
SCF	+3.64	0.77	+0.54	-0.24	-0.84	13.96

Energy values are in eV

Charges and spin values are in atomic units

perpendicular to the Fe₂ axis. Step 4 allows mixing with the full CO virtual space, which includes the CO virtual orbitals of a" symmetry, the π_z orbitals. These orbitals are parallel to the Fe₂ axis. Likewise, in step 6 the CO mixes with the Fe a' virtual orbitals, and in step 7 the CO mixes with the full Fe virtual space to include the Fe a" virtual orbitals. The steps are summarized in figure 5.6.

The frozen orbital energy is less repulsive by 5.24 eV when compared to our earlier full basis study of the C_s geometry, but the interaction is still more repulsive than in the FeCO(C_{4v}) and Fe₂CO(C_{2v}) systems. This is due largely to the much shorter Fe-O bond distance, which is in fact shorter than the Fe-C distance in this system. However, the lower frozen orbital energy does demonstrate that the starting Fe₂ configuration is better than that previously used.

In step 1, there is a very large change in energy, which was also observed in the earlier study concerning the tilted Fe₂CO geometry. This is a consequence due to the symmetry of the system, because now mixing between all the d orbitals can occur. This is in contrast to the FeCO(C_{4v}) geometry, where the symmetry restricts mixing between the different d orbital symmetry types. For both the spin majority and minority electrons, the d orbitals undergo polarization and mixing. In the spin majority space, the $d\delta(x^2-y^2)$ mixes with the $d\sigma(z^2)$ and the $d\pi(yz)$. The $d\delta(xy)$ mixes with the $d\pi(xz)$ and the $d\pi(yz)$. The $d\sigma(z^2)$ polarizes into more $d\sigma(x^2)$ character, and

it mixes with the $d\pi(xz)$ and $d\pi(yz)$. The spin minority electrons underwent even larger changes. The $d\sigma(z^2)$ and $d\sigma^*(z^2)$ were replaced by orbitals that are comprised of $d\delta(xy)$ and $d\pi(xz)$. These orbitals will be designated as $d(\pi+\delta)$ and $d^*(\pi+\delta)$. The $4p\pi_x$ orbital was also replaced by an orbital of $4p\sigma_z$ and $4p\pi_y$ character. Therefore, the spin minority Fe configuration is now $d(\pi+\delta)d^*(\pi+\delta)4s\sigma 4s\sigma^*4p(\sigma+\pi)$.

In the second step, very small changes are observed, which has been typical throughout the CSOV studies on these systems. Even in the C_s symmetry, very little σ donation from the Fe into the CO σ virtual orbitals is not a significant factor in the binding.

In the third step the energy change of 4.22 eV is the largest observed in all of our studies. The change in charge on each Fe atom is 0.44 and almost amounts to donating an electron to the CO. The change in charge on the C is -0.73, and the change in charge on the O is -0.14. For the spin minority electrons the energies of the d orbitals has dropped substantially by 0.8 eV. The charge transfer primarily occurs in the spin minority electrons. The CO $2\pi_y^*$ orbital has dropped into the occupied space replacing the $4p(\sigma+\pi)$ orbital. This also occurred in the bridging Fe_2CO , where a CO π^* orbital entered the occupied space. In addition to the $4p(\sigma+\pi)$ orbital being replaced, the $d\sigma(z^2)$ and $d\sigma^*(z^2)$ have replaced the $d(\pi+\delta)$ and $d^*(\pi+\delta)$ orbitals. The spin minority occupation is now $d\sigma(z^2)d\sigma^*(z^2)(CO 2\pi_y^*)4s\sigma 4s\sigma^*$.

In the fourth step as in the bridging Fe_2CO case, the change in energy is small, and the back donation is slight. This is indicated by the small change in charge on the Fe atoms. Likewise in the bridging Fe_2CO study, the $\text{CO } \pi_z$ orbitals are in the same plane as the Fe_2 ; therefore, one would expect the Fe_2 orbitals to have a major effect on the $\text{CO } \pi_z$ virtual orbitals. In both the bridging and the tilted Fe_2CO , the $\text{CO } \pi^*$ orbital that is perpendicular to the Fe_2 axis has proven to produce a more significant interaction.

In step 5 the spin majority $\text{CO } \pi$ orbitals have dropped lower in energy than the $\text{CO } 5\sigma$ orbital, which is not the case for the CO with the extended bond length. The spin minority electrons now have a $\text{CO } 2\pi_y^*$ orbital. Thus, the HOMO orbital ordering for the spin minority electrons is now $1\pi_y 1\pi_z 5\sigma_x 2\pi_y^*$, noting that the 1π orbitals have also dropped lower in energy than the 5σ orbital.

In the sixth step the $\text{CO } \sigma$ donation is substantial for this system. This is due in large part, because the $\text{CO } \pi_y$ orbitals are of A' symmetry. Therefore, the donation measured is actually $\sigma + \pi$ donation. In fact, based on the Mulliken population analysis, the O $1\pi_y$ orbital of the spin majority and minority donates into the Fe virtual orbitals. The change in charge on each Fe is -0.09, the change in charge on the C is +0.16, and the change in charge on the O is +0.02. This clearly indicates that the CO is donating electron density to the Fe_2 .

The ΔE_{step} for the seventh step has previously been negligible. In this step the change in energy, 0.64 eV, is fairly large. The changes in the charges are more significant. The change of charge on each Fe is -0.08, the change of charge on the C is +0.11, and the change in charge on the O is +0.05. In addition to the σ donation, π donation for the CO has become an important aspect in the bonding of the tilted structure. The combined energy of the CO donation is 1.86 eV, which is much more significant than in the other geometries.

The change in energy to the final SCF energy is not too large, but the changes in charges are significant. The change in charge on each Fe is +0.25, the change in charge on the C is -0.41, and the change in charge on the O is -0.09. This is due to the fact that the CO $2\pi_x^*$ of the spin minority electrons has now entered the occupied space. The charge on the CO is not larger, for the occupation of the addition CO virtual is also offset by more π donation from the $1\pi_y$ orbital. According to the Mulliken population analysis the $1\pi_y$ orbital has even less CO character and donated the electrons to the Fe₂. As in the FeCO(C_{4v}) study, the Fe π back donation and the CO σ donation into the Fe are highly correlated. It is even more substantial for the tilted Fe₂CO, because the CO not only σ donates but also π donates.

Because the convergence techniques could not produce an SCF energy for the full basis calculations on Fe₂CO (C_s), the

$^7A''$ state from the pseudopotential calculation had to be used. The optimized $^7A''$ geometry was used, and the valence molecular orbitals from the optimized structure were expanded using the Beebe technique described earlier in chapter 2. Because the pseudopotential calculations do not produce core molecular orbitals, we used the core molecular orbitals from the full basis Fe_2 calculation. The two sets of orbitals had to be Schmidt orthogonalized. The calculation converged rapidly and smoothly in 56 cycles. This point was then used as a starting point for the geometry optimization. The results are listed in table 5.17.

Again when the full basis set is used, the Fe-C distance has contracted, and the C-O distance has expanded. However, the charge on each Fe has decreased by 0.02, which should indicate less backdonation. The stretching frequency has lowered to 771.1 cm^{-1} , which is consistent with the longer C-O bond length. The binding energy with respect to the $d\delta^2 d\delta^* 2d\pi^2 d\pi^* 2d\sigma^2 d\sigma^* 24\sigma_s 24\sigma_s^* 14p\pi_x^1$ Fe_2 configuration has increased by 0.36 eV, which is a similar trend observed with the $Fe_2CO(C_{2v})$ cluster. It is also still unbound with respect to the $Fe(^5D)$ ground state.

The CSOV study was executed using the same steps that were applied on the pseudopotential calculation listed in figure 5.6, and the results are listed in table 5.18. The results follow the same trends as the pseudopotential with slight variations. The ΔE_{step} in step 1 is larger in the full

Table 5.17
 Geometry Optimization Results for Fe₂CO(C_s)
 Full Basis Set

State	Fe ₂ CO(⁷ A ^{''})
Energy (a.u.)	-2637.291913
Distances (Å)	
Fe-C	2.350
Fe-O	1.995
C-O	1.488
Charges	
Fe	+0.52
C	-0.23
O	-0.80
<S ² >	14.04
frequency	
v (cm ⁻¹)	771.1
Binding	
energies (eV)	
Fe ^a	-2.75
Fe ₂ ^b	+0.48

a) B.E. = 2*E(Fe(⁵D)) + E(CO) - E(Fe₂CO)

b) B.E. = E(Fe₂) + E(CO) - E(Fe₂CO)

Table 5.18
 CSOV Analysis for Fe₂CO (C_s) ⁷A"
 Full Basis Set

Geometry:

Fe - C distance = 2.350 Å

Fe - O distance = 1.995 Å

C - O distance = 1.488 Å

Reference Energy:

E(Fe₂) + E(CO) = -2637.132924

Step	Estep	ΔEstep	Charges			<s ² >
			Fe	C	O	
0	-6.40		0.00	+0.51	-0.51	14.15
1	-3.71	2.69	0.00	+0.52	-0.52	14.08
2	-3.53	0.18	0.00	+0.50	-0.49	14.10
3	+0.46	3.99	+0.45	-0.25	-0.65	14.26
4	+0.62	0.16	+0.47	-0.28	-0.66	14.23
5	+1.37	0.75	+0.54	-0.16	-0.92	14.24
6	+2.55	1.18	+0.40	+0.03	-0.84	14.29
7	+3.28	0.73	+0.29	+0.15	-0.73	14.29
SCF	+4.33	1.05	+0.52	-0.23	-0.80	14.04

Energy values are in eV

Charges and spin values are in atomic units

basis study by 0.62 eV showing more relaxation of the Fe₂ configuration. On the other hand the ΔE_{step} in step 3 is less in the full basis study by 0.23 eV showing less π backdonation, which is consistent with the final charge being lower, but one would expect a greater backdonation with a longer C-O bond. The ΔE_{step} in the final SCF step is larger, but this is a trend observed in all the full basis set calculations. This means the full basis set is more sensitive to the correlation between the σ donation and π backdonation than the pseudopotential basis set.

Conclusion and Future Studies

In conclusion, these preliminary cluster calculations of FeCO(C_{4v}), Fe₂CO(C_{2v}), and Fe₂CO(C_s) provide additional insight to the adsorption of CO on the Fe(100) surface. We tentatively conclude that the FeCO(C_{4v}) structure correlates to the CO(α_1) and CO(α_2) vertical states. We infer this based on the calculated CO stretching frequencies of 1992 and 2104 cm⁻¹ for the $5\Sigma^-$ and 5Π states, respectively, which are in the range of the CO(α_1) and CO(α_2) stretching frequencies of 2070 and 2010 cm⁻¹, respectively. The binding energy and the energy level diagram of the $5\Sigma^-$ state also compare well to the desorption energy and photoemission data for the CO(α_1) state. Evidence that the CO(α_1) or the CO(α_2) is a bridged structure is lacking. The calculated frequencies for the

$\text{Fe}_2\text{CO}(\text{C}_{2v})$ ${}^7\text{A}_2$ and ${}^7\text{B}_1$ states are very low compared to the experimentally observed values. It would be highly unlikely if additional Fe atoms would alter these values to reproduce experiment. Since the Fe(100) surface is an open surface, we expect the $\text{CO}(\alpha_1)$ and $\text{CO}(\alpha_2)$ to have CO vertically on top the Fe atoms in the top surface layer and vertically on top the Fe well atoms at the 4-fold site in the subsurface layer. This was also speculated by Carbo et al.¹³¹ Assignment to which site needs to be determined via experiment.

The calculations on the $\text{Fe}_2\text{CO}(\text{C}_s)$ cluster to represent the titled structure have yielded some interesting results. First, an elongated CO bond was produced, which is observed experimentally to be 0.07 Å longer relative to the vertical structures. Our optimized C-O length of 1.488 Å for the $\text{Fe}_2\text{CO}(\text{C}_s)$ cluster is considerably longer, but this elongation is important, because it supports the tilted structure being a precursor to dissociation. Secondly, the calculated stretching frequencies show promising results regarding the $\text{CO}(\alpha_3)$ state. The calculated values of 864.4 and 806.8 cm^{-1} for the ${}^7\text{A}'$ and ${}^7\text{A}''$ states, respectively, are not much lower than 1210 cm^{-1} for the $\text{CO}(\alpha_3)$ state. Including an Fe subsurface atoms and additional surface atoms to the cluster calculations should produce better results with respect to the experimental observations. Therefore, we believe these clusters provide an excellent starting point for further calculations.

Consequently, there are many directions to proceed with the Fe_xCO clusters. Different multiplicities need to be investigated on each cluster. For example, other authors have found bound states for the $\text{FeCO } ^3\Sigma^-$ state. For the Fe_2CO clusters, our data suggests that a multiplicity of 9 should be used. This is derived from the starting Fe_2 configuration of $d\delta^2d\delta^*2d\pi^2d\pi^*2d\sigma^2d\sigma^*24s24s\sigma^*14p\pi_x^1$ in the CSOV study, which can easily be transformed to $d\delta^2d\delta^*2d\pi^2d\pi^*2d\sigma^2d\sigma^*24s24s\sigma^*2$ with a multiplicity of 9. This Fe_2 configuration is the bulk ground state for Fe.

To study larger clusters the incremental cluster technique should be used. Using the wavefunctions of the Fe_xCO clusters to construct larger clusters will further determine if the smaller clusters are reasonable models for CO adsorption. From the $\text{FeCO}(C_{4v})$ cluster, an $\text{Fe}_3\text{CO}(C_{2v})$ cluster can easily be constructed to model the vertical on top surface adsorption. Likewise, a $\text{Fe}_5\text{CO}(C_{4v})$ cluster can be constructed to model the vertical adsorption on top Fe in the well at the 4-fold site. From the $\text{Fe}_2\text{CO}(C_{2v})$ cluster, an $\text{Fe}_4\text{CO}(C_{2v})$ cluster can be constructed to include Fe well atoms as well as an $\text{Fe}_6\text{CO}(C_{2v})$ cluster to include more surface atoms. More interesting would be to construct a $\text{Fe}_4\text{CO}(C_s)$ cluster from the $\text{Fe}_2\text{CO}(C_s)$ cluster to include the well atom below the CO. Then the additional Fe_2 atom could be added to construct an $\text{Fe}_6\text{CO}(C_s)$ cluster, which would include all the near surrounding Fe atoms of the $\text{CO}(\alpha_3)$ state.

Although, the pseudopotential did not produce very good results for the $\text{FeCO}(C_{4v})$ cluster, it did show better correlation with the Fe_2CO clusters. Problems with the pseudopotential would perhaps be alleviated by using a pseudopotential with the outer core electrons treated with the valence electrons and a larger basis set. In any case the pseudopotential did provide a good starting point for the full basis set calculations, and it will have to be used for larger clusters.

The CSOV analysis has shown to provide additional information regarding the major bonding interactions, which is important in understanding chemisorption. The CSOV studies were instrumental in finding lower states for the $\text{Fe}_2\text{CO}(C_{2v})$ and $\text{Fe}_2\text{CO}(C_s)$ clusters. Also, observed for both Fe_2CO clusters, the CO π^* orbitals perpendicular to the Fe_2 axis was shown to be the major acceptor of π backdonation. Furthermore, the CSOV analysis showed the CO virtual orbitals entering the occupied space for both Fe_2CO clusters. The CSOV analysis has proven to be a very useful tool in deciphering the major bonding interactions with chemisorption.

References

1. G. Binnig, H. Rohrer, *IBM J. Res. Dev.*, **30**, 355 (1986);
G. Binnig, H. Rohrer, G. Gerber, E. Weibel, *Phys. Rev. Lett.*, **50**, 120 (1983).
2. J. Benziger, R. J. Madix, *Surf. Sci.*, **94**, 119 (1980).
3. D. W. Moon, D. J. Dwyer, S. L. Bernasek, *Surf. Sci.*, **163**, 215 (1985).
4. R. Saiki, G. S. Hermann, M. Yamada, J. Osterwalder, C. S. Fadley, *Phys. Rev. Lett.*, **63**, 283 (1989).
5. D. W. Moon, S. L. Bernasek, D. J. Dwyer, J. L. Gland, *J. Am. Chem. Soc.*, **107**, 4363 (1985).
6. C. Benndorf, B. Kruger, F. Thieme, *Surf. Sci.*, **163**, L675 (1985).
7. U. Seip, M.-C. Tsai, K. Christmann, J. Kupperts, G. Ertl, *Surf. Sci.*, **139**, 29 (1984).
8. D. W. Moon, S. Cameron, F. Zaera, W. Eberhardt, R. Carr, S. L. Bernasek, J. L. Gland, D. J. Dwyer, *Surf. Sci.*, **180**, L123 (1987).
9. D. W. Moon, S. L. Bernasek, J. P. Lu, J. L. Gland, D. J. Dwyer, *Surf. Sci.*, **184**, 90 (1987).
10. J.-P. Lu, M. R. Albert, S. L. Bernasek, *Surf. Sci.*, **217**, 55 (1989).
11. C. Benndorf, B. Niebel, B. Kruger, *Surf. Sci.*, **177**, L907 (1986).

12. N. B. Brookes, A. Clarke, P. D. Johnson, *Phys. Rev. Lett.*, **63**, 2764 (1989).
13. N. D. Shinn, T. E. Madey, *Phys. Rev. Lett.*, **53**, 2481 (1984); N. D. Shinn, T. E. Madey, *J. Chem. Phys.*, **83**, 5928 (1985); F. Zaera, E. Kollin, J. L. Gland, *Chem. Phys. Lett.*, **121**, 464 (1984); F. M. Hoffman, R. A. DePaola, *Phys. Rev. Lett.*, **52**, 1697 (1984).
14. R. Hoffmann, *Angew. Chem. Int. Ed. Eng.*, **26**, 846 (1987); R. Hoffmann, *Solids and Surfaces: A Chemist's View of Bonding in Extended Structures*, VCH Publishers, New York, 1988.
15. *Electronic Structure, Dynamics, and Quantum Structural Properties of Condensed Matter*, eds. J. T. DeVreese, P. Van Camp, Plenum, New York, 1985.
16. *Structure and Bonding in Crystals*, I and II, eds. M. O'Keefe, A. Navrotsky, Academic, New York, 1981.
17. J. Sauer, *Chem. Rev.*, **89**, 199 (1989).
18. J. Koutecky, P. Fantucci, *Chem. Rev.*, **86**, 539 (1986).
19. R. C. Baetzold, J. F. Hamilton, *Prog. Solid St. Chem.*, **15**, 1 (1982).
20. E. Rechnagel, *At. Phys.*, **9**, 153 (1984).
21. K. Hermann, *Phys Bl*, **36**, 227 (1980).

22. Reference 1 in reference 25; A. B. Anderson, *J. Chem. Phys.*, **64**, 4046 (1976); P. S. Bagus, K. Hermann, M. Seel, *J. Vac. Sci. Tech.*, **18**, 435 (1981); B. Gumhalter, K. Wandelt, P. Avouris, *Phys. Rev. B*, **37**, 8048 (1988).
23. L. E. Orgel, *Inorg. Chem.*, **1**, 25 (1962).
24. C. M. Lukehart, *Fundamental Organometallic Chemistry*, Brooks/Cole, Monterey, Ca., 1985.
25. S. B. H. Bach, C. A. Taylor, R. J. Van Zee, M. T. Valen, W. Wetten, *J. Am Chem. Soc.*, **108**, 7104 (1986).
26. I. H. Hillier, V. R. Saunders, *Mol. Phys.*, **22**, 1025 (1971).
27. K. H. Johnson, U. Wahlgren, *Int. J. Quant. Chem. Symp.*, **6**, 243 (1972).
28. K. H. Johnson, in *Wave Mechanics*, p. 332, eds. W. C. Price, S. S. Chissick, T. Ravensdale, Butterworth, London, 1976.
29. S. Larsson, M. Braga, *Int. J. Quant. Chem.*, **15**, 1 (1979).
30. S. Demuyneck, A. Veillard, *Theor. Chim. Acta*, **28**, 241 (1973).
31. B.E. Burstein, D. G. Freier, R. F. Fenske, *Inorg. Chem.*, **19**, 1810 (1980).
32. P. S. Bagus, C. J. Nelin, C. W. Bauschlicher, *J. Vac. Sci. Tech. A*, **2**, 905 (1984).

33. C. W. Bauschlicher, P. S. Bagus, C. J. Nelin, B. O. Roos, *J. Chem. Phys.*, **85**, 354 (1986).
34. C. W. Bauschlicher, P. S. Bagus, *J. Chem. Phys.*, **81**, 5889 (1984).
35. R. G. Pearson, *Inorg. Chem.*, **23**, 4675 (1984).
36. W. Hieber, K. Wollmann, *Chem. Ber.*, **95**, 1552 (1962).
37. K. L. D'Amico, F. R. Freely, E. I. Solomon, *J. Am. Chem. Soc.*, **105**, 6380; R. R. Gay, M. H. Nodine, V. E. Henrich, H. J. Zeigler, E. I. Solomon, *J. Am. Chem. Soc.*, **103** (1980).
38. W. A. Hermann, H. Biersack, M. L. Ziegler, K. Weidenhammer, R. Siegel, D. Rehder, *J. Am. Chem. Soc.*, **103**, 1692 (1981); E. O. Friesden, R. J. J. Schneider, *Angew. Chem.*, **79**, 537 (1967); E. O. Friesden, R. J. J. Schneider, *Chem. Ber.*, **103**, 3684 (1970).
39. R. Hoffmann, M. M. L. Chen, D. L. Thorn, *Inorg. Chem.*, **16**, 503 (1977).
40. G. Blyholder, *J. Phys. Chem.*, **68**, 2772 (1964).
41. M. R. A. Blomberg, C. B. Lebrilla, P. E. M. Siegbahn, *Chem. Phys. Lett.*, **150**, 522 (1988).
42. P. Avouris, P. S. Bagus, C. J. Nelin, *J. Elect. Spect. Rel. Phen.*, **38**, 269 (1986).
43. G. Broden, T. N. Rhodin, C. Brucker, R. Benbow, Z. Huryck, *Surf. Sci.*, **59**, 593 (1976); T. Engel, G. Ertl, *Adv. Catal.*, **28**, 1 (1979); I. M. Campbell, *Catalysis at Surfaces*, Chapman and Hall, London, 1988.

44. S. Sung, R. Hoffmann, *J. Am. Chem. Soc.*, **107**, 578 (1988).
45. D. R. Salahub, M. C. Zerner, in *The Challenge of d and f Electrons*, p. 1, eds. D. R. Salahub, M. C. Zerner, American Chemical Society, Washington D. C., 1989.
46. E. R. Davidson, in *The Challenge of d and f Electrons*, p. 153, eds. D. R. Salahub, M. C. Zerner, American Chemical Society, Washington D. C., 1989.
47. *Quantum Chemistry: The Challenge of Transition Metals and Coordination Chemistry*, eds. A. Veillard, D. Reidel Publishing Co., Dordrecht, 1985.
48. E. R. Davidson, D. Feller, *Chem. Rev.*, **86**, 681 (1986).
49. P. J. Hay, *J. Chem. Phys.*, **66**, 4377 (1977).
50. A. Szabo, N. S. Ostlund, *Modern Quantum Chemistry*, MacMillan Publishing CO., New York, 1982; I. N. Levine, *Quantum Chemistry*, Allyn and Bacon, Boston, 1983.
51. GAMESS, The Generalized Atomic and Molecular Electronic Structure System, B. R. Brooks, P. Saxe, W. D. Laidig, M. Dupius, D. Spangler, J. J. Wendoloski, NRCC Lawrence Livermore Laboratory.
52. H. B. Schlegel, D. W. McDouall, in *Computational Advances of Organic Chemistry: Molecular Structure and Reactivity*, p. 167, eds. C. Ogretir, G. Csizmadia, Kluwer Academic Publishers, Netherlands, 1991.
53. C. W. Bauschlicher, D. H. Liekow, C. F. Bender, H. F. Schaeffer, *J. Chem. Phys.*, **16**, 281 (1976).

54. B. V. Cox, C. W. Bauschlicher, *Surf. Sci.*, **102**, 295 (1981).
55. J. D. Head, CONAVE routine in GAMESS.
56. N. H. F. Beebe, S. Lunell, *Int. J. Quant. Chem.*, **6**, 1149 (1972).
57. P. O. Lowdin, *Advan. Phys.*, **5**, 1 (1956).
58. P. O. Lowdin, *Phys. Rev.*, **139**, A357 (1965).
59. P. O. Lowdin, *Advan. Quant. Chem.*, **5**, 185 (1970).
60. K. Hermann, P. S. Bagus, C. J. Nelin, *Phys. Rev. B*, **35**, 9467 (1987).
61. I. Panas, J. Schule, P. Siegbahn, U. Wahlgren, *Chem. Phys. Lett.*, **149**, 265 (1988).
62. C. W. Bauschlicher, *Chem. Phys. Lett.*, **129**, 586 (1986).
63. P. S. Bagus, H. F. Schaefer, C. W. Bauschlicher, *J. Chem. Phys.*, **78**, 1390 (1989).
64. K. Hermann, P. S. Bagus, *Phys. Rev. B*, **17**, 4082 (1978).
65. T. B. Grimley, E. E. Mola, *J. Phys. C*, **9**, 3437 (1976).
66. P. S. Bagus, W. Muller, *Chem. Phys. Lett.*, **115**, 540 (1985).
67. K. Hermann, P. S. Bagus, C. W. Bauschlicher, *Phys. Rev. B*, **30**, 7313 (1986).
68. P. S. Bagus, K. Hermann, *Appl. Surf. Sci.*, **22/23**, 444 (1985).
69. P. S. Bagus, K. Hermann, *Phys. Rev. B*, **33**, 2987 (1986).
70. M. R. A. Blomberg, P. E. M. Siegbahn, *J. Chem. Phys.*, **78**, 986 (1983).

71. M. R. A. Blomberg, P. E. M. Siegbahn, *J. Chem. Phys.*, **78**, 5682 (1983).
72. P. E. M. Siegbahn, M. R. A. Blomberg, C. W. Bauschlicher, *J. Chem. Phys.*, **81**, 1373 (1984).
73. M. Balooch, J. M. Cardillo, D. R. Miller, R. E. Stickney, *Surf. Sci.*, **46**, 358 (1974).
74. W. H. Press, B. P. Flannery, S. A. Teuholsky, W. T. Vetterling, *Numerical Recipes. The Art of Scientific Computing*. Cambridge University Press, Cambridge, 1986.
75. J. Cioslowski, *J. Chem. Phys.*, **89**, 2126 (1988).
76. W. B. Nielsen, *Chem. Phys. Lett.*, **18**, 225 (1973).
77. I. Roeggen, *Chem. Phys. Lett.*, **22**, 140 (1973).
78. M. J. S. Dewar, P. K. Weiner, *Comput. Chem.*, **2**, 31 (1978).
79. L. G. Ferriera, *J. Comput. Phys.*, **36**, 198 (1980).
80. Z. Chen, *Chem. Phys. Lett.*, **87**, 455 (1982).
81. D. Cremer, J. Gauss, *J. Comput. Chem.*, **7**, 274 (1986).
82. P. Pulay, *Chem. Phys. Lett.*, **73**, 393 (1980).
83. P. Pulay, *J. Comp. Chem.*, **3**, 556 (1982).
84. C. Lanczos, *J. Res. Natl. Bur. Std. US* **45**, **255** (1950).
85. H. Sellers, to appear in *Chem. Phys. Lett.*
86. D. R. Hartree, *Calculation of Atomic Structure*, Wiley, New York, 1957.
87. C. C. J. Roothaan, P. S. Bagus, *Methods in Computational Physics*, II, p. 47, eds. B. B. Adler, S. Fernbach, M. Rotenberg, Academic Press, New York (1963).

88. M. C. Zerner, M. Hehenberger, *Chem. Phys. Lett.*, **62**, 550 (1979).
89. G. Karlstrom, *Chem. Phys. Lett.*, **67**, 348 (1979).
90. P. de Montgolfier, A. Hoareau, *J. Chem. Phys.*, **65**, 2477 (1976).
91. Hsu, Davidson, Pitzer, *J. Chem. Phys.*, **65**, 609 (1976).
92. V. R. Saunders, I. H. Hillier, *Int. J. Quant. Chem.*, **7**, 699 (1973).
93. R. Carbo, J. A. Hernandez, F. Sanz, *Chem. Phys. Lett.*, **47**, 581 (1977).
94. M. F. Guest, V. R. Saunders, *Mol. Phys.*, **28**, 819 (1974).
95. A. V. Mitin, *J. Comput. Chem.*, **9**, 107 (1988).
96. A. Veillard, in *Computational Techniques in Quantum Chemistry and Molecular Physics*, p. 201, eds. G. H. Durchsen, B. T. Suttcliffe, A. Veillard, Reidel, Boston, 1975.
97. J. D. Head, G. Blyholder, F. Ruetter, *J. Comp. Phys.*, **45**, 255 (1982).
98. M. DuPuis, H. F. King, *Int. J. Quant. Chem.*, **11**, 613 (1977).
99. T. Takada, M. DuPuis, *J. Chem. Phys.*, **75**, 332 (1981).
100. T. Takada, M. DuPuis, H. F. King, *J. Comp. Chem.*, **4**, 234 (1983).
101. J. D. Head, *J. Comp. Chem.*, **11**, 67 (1990).
102. P. Lykos, R. G. Parr, *J. Chem. Phys.*, **24**, 1166 (1956).

103. R. McWeeney, *Proc. R. Soc. London Ser. A*, **253**, 242 (1959).
104. R. McWeeney, K. Ohno, *Proc. R. Soc. London Ser. A*, **255**, 367 (1960).
105. W. H. Fink, A. M. Butkus, J. P. Lopez, *Int. J. Quant. Chem. Symp.*, **13**, 331 (1979).
106. P.S. Bagus, K. Hermann, C. W. Bauschlicher, *J. Chem. Phys.*, **80**, 4378 (1984).
107. P. S. Bagus, K. Hermann, C. W. Bauschlicher, *J. Chem. Phys.*, **81**, 1966 (1984).
108. R. S. Mulliken, *J. Chem. Phys.*, **23**, 1833 (1955).
109. C. W. Bauschlicher, *Chem. Phys.*, **106**, 391 (1984).
110. J. D. Head, T. E. Meehan, S. Silva, *Phys. Scripta*, **41**, 874 (1990).
111. E. Ganz, K. Sattler, J. Clarke, *J. Vac. Sci. and Tech*, **A6**, 419 (1988).
112. H. Mizes, J. S. Foster, *Science*, **224**, 559 (1989).
113. F. Illas, F. Sanz, J. Virgili, *J. Mol. Struct. THEOCHEM*, **94**, 79 (1983); R. Caballol, J. Igual, F. Illas, J. Rubio, *Surf. Sci.*, **149**, 621 (1985); G. Abbate, V. Barone, F. Lelj, E. Iaconis, N. Russo, *Surf. Sci.*, **152/153**, 690 (1985)(1987); V. Barone, F. Lelj, E. Iaconis, F. Illas, N. Russo, A. Jounou, *J Mol. Struct. THEOCHEM*, **136**, 313 (1986); V. Barone, F. Lelj, E. Iaconis, F. Illas, N. Russo, *J Mol. Struct. THEOCHEM*, **139**, 277 (1986).

114. J. Almlof, H. P. Luthi, *Supercomputer Research in Chemistry and Chemical Engineering*, p. 35, eds. C. Jensen, D. Truhlar, American Chemical Society, Washington D. C., 1987.
115. W. J. Hehre, R. F. Stewart, J. A. Pople, *J. Chem Phys.*, **51**, 2657 (1969); W. J. Hehre, R. Ditchfield, R. F. Stewart, J. A. Pople, *J. Chem. Phys.*, **52**, 2769 (1970); W. J. Pietro, B. Levi, W. J. Hehre, R. F. Stewart, *Inorg. Chem.*, **19** 2225 (1980); W. J. Pietro, E. S. Blurock, R. S. Hout, W. J. Hehre, D. J. DeFrees, R. F. Stewart, *Inorg. Chem.*, **20**, 3650 (1981);
116. W. J. Hehre, L. Radom, v. R. Schleyer, P. Schleyer, J. A. Pople, *Ab Initio Molecular Orbital Theory*, Wiley, New York, 1986.
117. A. Haaland, *J. Organometal. Chem.*, **92**, 157 (1975).
118. F. L. Pilar, *Elementary Quantum Chemistry*, McGraw Hill, New York, 1968.
119. T.E. Meehan, J. D. Head, *Surf. Sci. Lett.*, **243**, L55 (1991).
120. P. J. Hay, W. R. Wadt, *J. Chem. Phys.*, **82**, 270 (1985).
121. A. J. H. Wachters, *J. Chem. Phys.*, **52**, 1033 (1970).
122. P. J. Hay, *J. Chem. Phys.*, **66**, 4377 (1984).
123. C. W. Bauschlicher, L. G. M. Petterson, P. E. M. Siegbahn, *J. Chem. Phys.*, **87**, 2129 (1987).

124. T. H. Dunning, P. J. Hay, in *Methods of Electronic Structure*, p. 1, ed. H. F. Schaefer, Plenum, New York, 1977.
125. D. C. Harris, M. D. Bertolucci, *Symmetry and Spectroscopy: An Introduction to Vibrational and Electronic Spectroscopy*, Dover Publishers, New York, 1978.
126. V. R. Marathe, A. Sawaryn, A. X. Trautwein, *Hyper. Int.*, **36**, 39 (1987); A. C. Pavao, M. Braga, C. A. Taft, B. L. Hammond, W. A. Lester, *Phys. Rev. B*, **43**, 6962 (1991).
127. G. Berthier, A. Dauodi, M. Suard, *J. Mol. Struct. (Theochem)*, **179**, 407 (1988).; A. Dauodi, M. Suard, C. Barbier, *J. Chim. Phys.*, **84**, 795 (1987).
128. C. H. Peden, S. F. Parker, P. H. Barrett, R. G. Pearson, *J. Phys. Chem.*, **87**, 2329 (1983).
129. P. C. Engelking, W. C. Lineberger, *J. Amer. Chem. Soc.*, **101**, 5569 (1979).
130. R. K. Sheline, K. S. Pitzer, *J. Am. Chem. Soc.*, **72**, 1107 (1950).
131. A. C. Pavao, M. Braga, C. A. Taft, B. L. Hammond, W. A. Lester, to appear in *Phys. Rev. B*.